

MICROMACHINED MILLIMETER WAVE CIRCUITS

by

NOOR ASNIZA MURAD

A thesis submitted to the University of Birmingham for the degree of
DOCTOR OF PHILOSOPHY

School of Electronic, Electrical and Computer Engineering

College of Engineering and Physical Sciences

The University of Birmingham

May 2011

UNIVERSITY OF
BIRMINGHAM

University of Birmingham Research Archive

e-theses repository

This unpublished thesis/dissertation is copyright of the author and/or third parties. The intellectual property rights of the author or third parties in respect of this work are as defined by The Copyright Designs and Patents Act 1988 or as modified by any successor legislation.

Any use made of information contained in this thesis/dissertation must be in accordance with that legislation and must be properly acknowledged. Further distribution or reproduction in any format is prohibited without the permission of the copyright holder.

Abstract

This thesis presents the design and characterisation of millimetre-wave Butler matrix beamforming circuits at 63 GHz. A micromachining technique is used to fabricate the tiny structures. The ability to manufacture the circuits at this frequency may benefit to the development of intelligent transport system (ITS) communication and sensing systems. All components that build the Butler matrix beamformer are designed to fit the thick SU-8 photoresist micromachining technology, where structures are built by bonding together five layers of metal coated SU-8. The matrix is constructed using air filled rectangular coaxial lines. The dielectric losses are avoided by having air filled structure, however the suspended lines need supporting system. Therefore, stubs are placed in the circuits to hold the suspended lines. In order to transfer signal from the Butler matrix to the antenna, a transition is necessary. A rectangular coaxial line to ridge waveguide transition is designed to feed the H-plane horn antenna and the ridge waveguide slot antenna. **The novelty of this work is in both the design of new microwave structure and also in the demonstration of millimetre wave structures in micromachined form using SU8 resist. Four new microwave structures are (1) a back to back rectangular coaxial line to ridge waveguide transition, (2) an H-plane horn antenna, (3) a ridge waveguide slot antenna, and (4) a Butler matrix with a patch antenna array.** These and other structures have been built and tested and finally the selection put together to form a new type of Butler matrix. The compatibility of the designs to the fabrication method has been demonstrated. The transition return loss is better than -12 dB from 60 GHz to 90 GHz and has been proven to work with integration to the horn and the waveguide slot antenna. The

Butler matrix with a patch antenna array exhibits the forming of the beams at $\pm 17^\circ$ as expected from the theoretical calculation.

Acknowledgements

I am grateful for guidance and continuous support from my supervisor, Prof. M. J. Lancaster. His inspiring advices and commitment during the period of this work are invaluable. My particular thanks go to my second supervisor, Dr. P. Gardner, for fruitful advices in numerous discussions especially on the antenna parts. My appreciations go to Dr. Yi Wang and Dr Mao Long Ke, who helped me in the technical parts including advices, fabrications and measurements. I am also wish to thank Dr. Gemma Louise Nicholson for her friendship and revising the English language of this thesis. Not forgetting, Xiaobang Shang, Talal Skaik and all my office mates for their encouragements. It has been a priceless experience working with such a dynamic team.

I would like to acknowledge the Ministry of Higher Education, Malaysia and the University of Technology Malaysia (UTM) for the financial support throughout my study.

Finally, I would like to express my special appreciation to my wonderful and understanding husband (Ahmad Shahir) and son (Ahmad Arif Farhan), for their love and patience that make this happen. Thanks also to all my family for their support and encouragement.

Table of Contents

Abstract	
Acknowledgements	
Table Of Contents	
List Of Tables	
List Of Figures And Illustrations	
Chapter 1	1
Introduction	1
1.1 Introduction	1
1.2 Motivation And Objective	8
1.3 Scope Of Research	12
1.4 Thesis Layout	14
Chapter 2	17
Micromachining	17
2.1 Introduction	17
2.2 Micromachining Fabrication Techniques	19
2.2.1 Bulk Micromachining	20
2.2.1.1 Liga	23
2.2.1.2 Membrane Technology	24
2.2.2 Surface Micromachining	27
2.3 Thick Su-8 Photoresist Technique	30
2.4 Summary	39
Chapter 3	42
Micromachined Transmission Lines And Transitions	42
3.1 Introduction	42
3.1.1 Transmission Lines	43
3.1.2 Micromachined Transmission Lines	47
3.1.3 Transmission Lines Losses	55

3.2	Micromachined Rectangular Coaxial Lines	56
3.3	Co-Planar Waveguide (Cpw)	61
3.4	Cpw To Rectangular Coaxial Line Transition	63
3.5	Rectangular Waveguide	65
3.5.1	Rectangular Ridge Waveguide	68
3.6	Micromachined Coaxial Line To Ridged Waveguide Transition	70
3.7	Summary	80
	Chapter 4	83
	Micromachined Antennas	83
4.1	Introduction	83
4.2	Micromachined Patch Antenna	84
4.2.1	Patch Antenna Design	88
4.3	Micromachined Horn Antenna	99
4.3.1	H-Plane Horn Antenna Design	103
4.4	Ridge Waveguide Slot Antenna	110
4.4.1	Ridge Waveguide Slot Antenna Design	114
4.5	Summary	122
	Chapter 5	127
	Micromachined Coupler And Butler Matrix Beamforming	127
5.1	Introduction	127
5.2	Types Of Coupler	128
5.3	Hybrid Branch Line Coupler	131
5.3.1	Odd And Even Mode Analysis	132
5.3.2	Design And Characteristics	136
5.4	Butler Matrix Beamforming	142
5.4.1	Array Factor	144
5.4.2	Butler Matrix With A Patch Antenna Array	147

5.4.3 Butler Matrix With A Horn Antenna Array	156
5.4.4 Butler Matrix With A Ridge Waveguide Slot Antenna Array	160
5.5 Summary	164
Chapter 6	166
Conclusions And Future Work	166
6.1 Conclusions	166
6.2 Future Work	168
6.2.1 Studies On Fabrication Errors	168
6.2.2 Broadband Butler Matrix And Wideband Antenna Array	169
6.2.3 Antenna Measurement At Millimetre-Wave Frequencies Using On-Wafer Probe Station	169
6.2.4 Front End Design And Real Application Implementation.	169
Appendix A	171
Appendix B	179
Appendix C	180

List of Tables

Table 1.1 : General applications of V2V and R2V ITS	4
Table 1.2: ITS characteristics	5
Table 2.1: The thick SU-8 micromachining recipe for 200 μm layer thickness as used in this thesis.	31
Table 3.1 Micromachined Transmission Lines.	48
Table 3.2 Rectangular Coaxial Line Dimensions.	60
Table 3.3 Ridge Waveguide Dimensions.	70
Table 4.1 The early micromachined patch antennas.....	86
Table 4.2 Micromachined horn antennas.	102
Table 4.3 Ridge waveguide slot antenna dimensions.	117
Table 4.4 Comparisons of the antenna performances at 63 GHz.	123
Table 5.1 Different types of coupler [1-3].	129
Table 5.2 The impedances (in ohms) and dimensions (in μm) of semi-coaxial lines.	139
Table 5.3 Theoretical 4x4 Butler matrix phase difference between input and output.....	143

List of Figures and Illustrations

Figure 1.1: 24 GHz vehicle radar sensor network block diagram taken from [9].....	2
Figure 1.2: 24 GHz vehicle radar sensor network block diagram taken from [10].....	3
Figure 1.3: A dual channel, bi-static configuration.	6
Figure 1.4: System illustration taken from [19].	8
Figure 1.5: 63 GHz and 77 GHz radar system concept taken from [19].	9
Figure 1.6: Butler Matrix Beamformer.	10
Figure 1.7: Five layers rectangular coaxial line structure; (a) five layers exploded view; and (b) top view of Layer 3, showing the centre conductor of rectangular coaxial line.	11
Figure 1.8: Research scope diagram.	13
Figure 2.1: Isotropic and anisotropic etched cantilever structure [8].	21
Figure 2.2 : DRIE manufacturing technique [10].	22
Figure 2.3: UV LIGA fabrication steps [11].	24
Figure 2.4: Membrane supported transmission line taken from [13].	25
Figure 2.5: Microwave filters taken from [14].	26
Figure 2.6: Membrane supported transmission line taken from [14].	27
Figure 2.7: An example of surface micromachining process steps [16].	28
Figure 2.8: Capacitive switch fabrication process taken from [17].	30
Figure 2.9: The process of fabrication and assembly.	32
Figure 2.10: Wall imperfection.	35
Figure 2.11: Second evaporation on the imperfect wall before assembling the top layer. .	36
Figure 2.12: The cavity filter structure without the top layer taken from [22].	37
Figure 2.13: (a) The structure and (b) the dimensions of middle layer taken from [23]. ...	37
Figure 2.14: (a) The structure and (b) the detail dimensions of middle layer taken from [24].	38
Figure 3.1: Guiding structures	44
Figure 3.2: Attenuation constant versus area, taken from [9]	55

Figure 3.3: Cross section of the rectangular coaxial line.....	57
Figure 3.4: Calculated and simulated characteristic impedance.	59
Figure 3.5: Co-planar waveguide (CPW) configuration.....	61
Figure 3.6: (a) CPW to rectangular coaxial line transition and (b) the cross section.....	64
Figure 3.7: Dominant mode field lines of rectangular waveguide [4].....	65
Figure 3.8: TE ₁₀ field variations across a rectangular waveguide aperture.	66
Figure 3.9: Coaxial feed waveguide	67
Figure 3.10: Ridge waveguide feeding a horn antenna.....	68
Figure 3.11: Cross sections diagram; (a) single ridge waveguide and; (b) double ridge waveguide.....	69
Figure 3.12: Coaxial line to double ridge waveguide transition presented in [31].	71
Figure 3.13: Rectangular coaxial line to ridge waveguide transition and the cross sections	73
Figure 3.14: Simulated response of the rectangular coaxial line to ridge waveguide transition.	74
Figure 3.15: Back to back coaxial line to ridge waveguide transition circuit.....	75
Figure 3.16: Five layers exploded view with all dimensions in μm	76
Figure 3.17: Metal coated pieces of layer 3 and 4.....	77
Figure 3.18: Simulated and measured response of the transition.	78
Figure 3.19: Simulated responses for different stub length with $S = 1840 \mu\text{m}$	79
Figure 3.20: Simulated responses for different stub spacing with $L = 1840 \mu\text{m}$	79
Figure 4.1: Microstrip patch antenna	85
Figure 4.2: Microstrip line and its electric field lines.....	88
Figure 4.3: The patch antenna and most common feeding types.	91
Figure 4.4: The single patch antenna fed by a rectangular coaxial line.....	93
Figure 4.5: The simulated return loss of the single patch antenna.	94
Figure 4.6: The simulated radiation pattern of the single patch antenna at 63 GHz.	96
Figure 4.7: A patch antenna with two supporting lines.	97

Figure 4.8: Simulated return loss.....	97
Figure 4.9: Simulated radiation patterns at 63 GHz.	98
Figure 4.10: Horn antennas.	100
Figure 4.11: Phase error due to the wave curvature in the horn aperture.	103
Figure 4.12: H-plane sectoral horn antenna.	105
Figure 4.13: The H-plane horn structure.....	106
Figure 4.14: The layer layouts (all dimensions are in μm).	106
Figure 4.15: Simulated return loss of the integrated H-plane horn antenna.	107
Figure 4.16: Simulated radiation pattern of the integrated H-plane horn antenna.	108
Figure 4.17: Simulated and measured return loss.....	109
Figure 4.18: Simulated and measured radiation pattern at 63 GHz.....	110
Figure 4.19: Rectangular waveguide dominant mode surface current.	111
Figure 4.20: Slots on waveguide.	112
Figure 4.21: Waveguide longitudinal slot antenna and its equivalent circuit.	114
Figure 4.22: Ridge waveguide slot antenna and the layer layouts.	118
Figure 4.23: Simulated return loss of the waveguide slot antenna.	119
Figure 4.24 Simulated radiation pattern of the waveguide slot antenna at 63 GHz.	120
Figure 4.25 Simulated and measured return loss.....	121
Figure 4.26 Simulated and measured radiation pattern.	122
Figure 5.1: Four port network.	128
Figure 5.2: Hybrid 3-dB branch line coupler.	132
Figure 5.3: Circuit diagram of normalized branch line coupler.	132
Figure 5.4: Decomposition of Branch Line Coupler into (a) even and (b) odd mode excitation [3].	133
Figure 5.5: The branch line coupler with shorted stubs.....	138
Figure 5.6: Branch line coupler (a) without and (b) with stubs.....	139
Figure 5.7: Simulated S-parameters of the coupler without stubs.....	140

Figure 5.8: Simulated S-parameters of the coupler with stubs.....	141
Figure 5.9: 4x4 Butler matrix topology diagram.....	142
Figure 5.10: Array factor for different distances between 2 antenna elements.....	145
Figure 5.11: Calculated radiation patterns for single patch antenna.	146
Figure 5.12: Calculated radiation patterns for 2 element patch antenna array.....	147
Figure 5.13: Butler matrix with a patch antenna array.	148
Figure 5.14: Return loss of the patch antenna array.	149
Figure 5.15: 3D radiation pattern of the patch antenna array.....	150
Figure 5.16: A simulated H-plane field pattern at 63 GHz with an input at port 1.	151
Figure 5.17: A simulated H-plane field pattern at 63 GHz with an input at port 4.	151
Figure 5.18: Five layer exploded view.....	152
Figure 5.19: Dimensions (in μm) of (a) layers 2 and 4; and (b) layer 3 of the structure..	153
Figure 5.20: Simulated and measured return loss with input from port 1 (S_{11}) and port 4 (S_{44}).	154
Figure 5.21: Simulated and measured inter-port isolation (S_{41}) of the patch antenna array.....	154
Figure 5.22: Simulated and measured H-plane radiation pattern of the patch antenna array.....	155
Figure 5.23: H-plane horn antenna array with Butler matrix structure without top layer.	156
Figure 5.24: Simulated return loss of a BM with an H-plane horn antenna array.....	157
Figure 5.25: Simulated 3D radiation pattern of H-plane horn antenna array.....	158
Figure 5.26: Simulated H-plane radiation pattern of H-plane horn antenna array.....	159
Figure 5.27: Butler matrix with a ridge waveguide slot antenna array.....	160
Figure 5.28: Simulated return loss of the Butler matrix with the ridge waveguide slot antenna array.....	161
Figure 5.29: Simulated 3D radiation pattern of the ridge waveguide slot antenna array.	162
Figure 5.30: Simulated E-plane radiation pattern of the ridge waveguide slot antenna array.....	163

List of Symbols and Abbreviations

λ	Wavelength
ω	Angular frequency
δ	Skin depth
δ_e	Phase error
3D	Three Dimensional
AF	Array factor of the array antenna
Au	Gold
BW	Bandwidth
c	Speed of light in free space
CPW	Coplanar waveguide
Cr	Chromium
D	Largest dimension of the antenna
DRIE	Deep reactive ion etching
E	Electric field intensity (V/m)
EM	Electromagnetic
f	Resonance frequency (Hz)
f_c	Cutoff frequency (Hz)
H	Magnetic field intensity (V/m)
HPBW	Half Power Beamwidth
L	Antenna length
LIGA	German acronym for lithography, electroforming and moulding
PEB	Post Expose Bake
r	Distance far from the antenna
Si	Silicon
TE	Transverse electric field
UV	Ultraviolet
W	Antenna width
Z_o	Characteristic impedance (Ω)
Z_{in}	Input impedance (Ω)
β	Phase constant
ΔL	Extension in antenna length due to fringing field
ϵ_{eff}	Effective dielectric constant
ϵ_o	Dielectric constant of free space
ϵ_r	Dielectric constant of substrate material

Chapter 1

Introduction

1.1 Introduction

Microwaves can be referred to the electromagnetic (EM) waves with frequencies ranging between 300 MHz and 300 GHz[1]. This range corresponds to the free space wavelengths varying from 1 m to 1 mm. The EM waves that travel in the millimetre wavelength range at frequencies between 30 GHz and 300 GHz are also known as millimetre waves [2]. Millimetre wave communication have been studied since 1970's [3]. In the last few years, many applications for millimetre wave frequencies have emerged. Operating in the millimetre wavelength frequency range provides many benefits including i) the availability of a high bandwidth, ii) small physical size of antenna for high gain requirements, iii) multi-channel and / or multi-time-slot operation, and iv) very high data rate communications [4].

Frequencies ranging from 30 GHz up to 60 GHz are allocated for commercial applications in radar, satellite and mobile communications [5]. 60 GHz with a 3-7 GHz bandwidth is open for wireless communication depending upon the country. This frequency band becomes of interest in the development of wireless access and wireless local area network (LAN) as part of the fourth generation (4G) systems due to its large spectral space allocation [6, 7].

Smart transportation system is another application operating at millimetre wavelength. Intelligent Transportation Systems (ITS) based on vehicle to vehicle and vehicle to roadside communications have been studied for many years in Europe, North America and Japan [8]. Short range radar (SRR) and long range radar (LRR) systems have been identified as significant technologies to improve road safety. Those radar sensors are now operating at 24 GHz, but will move to the 71 to 81 GHz range by mid 2013 [9]. This is to avoid interference with other applications of the licensed-free 24 GHz industry, scientific and medical (ISM) band. Short range radar in automotive systems can enable different applications as shown in Figure 1.1. These applications, together with long range radar automatic cruise control, could assist the driver in safety driving.

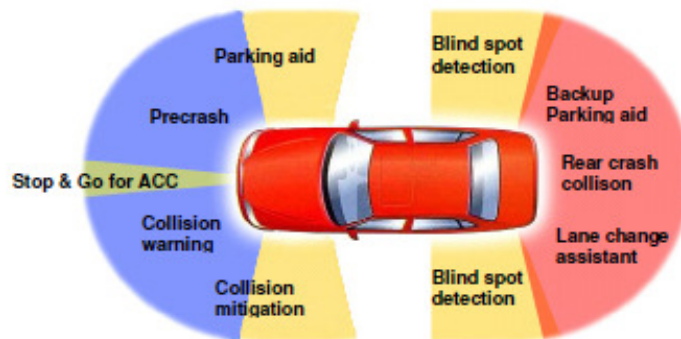


Figure 1.1: 24 GHz vehicle radar sensor network block diagram taken from [9].

Figure 1.2 shows an example of 24 GHz radar sensor network block diagram implemented in [10]. An external signal was sent into the system for processing and to identify tracking targets and objects.

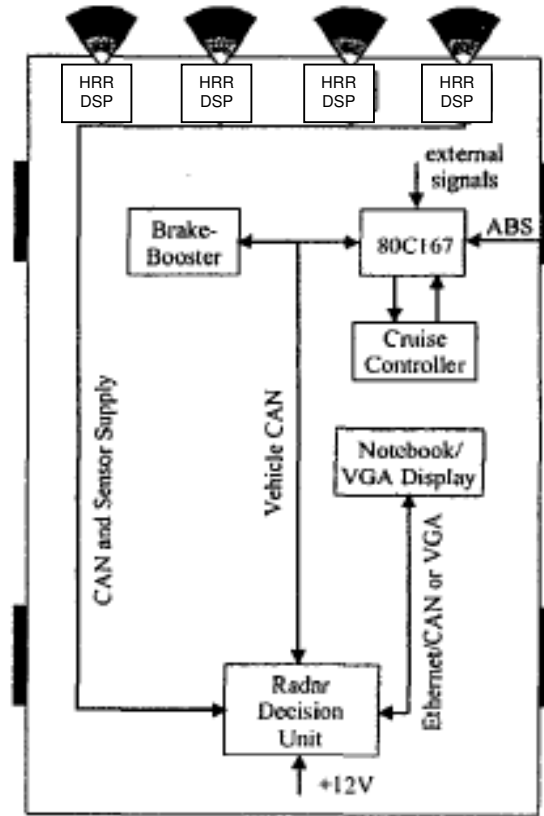


Figure 1.2: 24 GHz vehicle radar sensor network block diagram taken from [10].

The transition time from 24 GHz to higher millimetre wavelength frequencies allows more research and enhancements towards mature SRR sensor systems. Anti collision SRR and automatic cruise control LRR can be designed at 77 GHz.

On the other hand, 63 GHz is allocated for vehicle to vehicle (V2V) and roadside to vehicle (R2V) communication systems. The system will allow the exchange of safety information between cars. In addition, information such as safety and hazard warnings can be transferred from the roadside units. Thus, the driver can take precautions to facilitate safe driving. Table

1.1 describes general applications for V2V and R2V while Table 1.2 gives a summary of ITS characteristics in the frequency range of 63-64 GHz [11].

Table 1.1 : General applications of V2V and R2V ITS

	Application	Description
1	Automatic Fee Collection (AFC) Access	Charges for use of road at point of use / allows access to controlled area.
2	Traffic information	Sends data to car advising of traffic congestion, poor visibility ahead
3	Route guidance	Advices driver on traffic flow problems ahead and alternative route.
4	Traffic monitoring	Gathers information for traffic management.
5	Parking management	Enables driver to check ahead on availability of parking and to prebook.
6	Freight and fleet management	Efficient management of freight and fleet. For example locates vehicles and transmit nature of cargo to save time at border controls.
7	In car internet / PC mobile office	Provides an internet style access of telematic data.
8	Co-operative driving	Alerts driver to another vehicle braking, changing lane, etc.
9	Platoons / road trains	Organizes a number of vehicles into convoys.
10	Emergency warning	Alerts driver to sudden manoeuvres or failures of nearby vehicles.
11	Intelligent intersection control	Alerts driver to other vehicles at intersections.
12	Feed from radio station	Local, national or international radio stations stream live (only with node backhaul) or pre-recorded (content on node) via nodes.
13	Stolen vehicle alarm, tracking and recovery	Unauthorised movement of vehicle is detected and authorities alerted. Vehicle is then tracked for recovery.

Table 1.2: ITS characteristics

Parameter	Values / characterisation
Frequency	63-64 GHz
EIRP	40dBm
Antenna gain (roadside unit)	23 dBi
Antenna gain (vehicle)	21 dBi (V2V) and 14 dBi (V2R)
Sidelobe Attenuation	20 dB
Range	up to 300 m
Channel spacing	192 MHz to 1 GHz
Bandwidth	120 MHz

There are numerous reports of ITS research in the United Kingdom, such as the Short and Long Range Integrated Multifunction Radar and Communication Sensors (SLIMSENS) [12]. This project, led by e2v Technologies, tried to extend the function of 77 GHz radar transceiver devices in their operation as radar sensors with the integration of a short range high rate data communication function. The Future Antenna Technologies for Cars and Trucks (FATCAT) and Millimetric Transceivers for Transport Applications (MILTRANS) [13, 14] are another two projects conducted in the United Kingdom. The projects are being led by BAE Systems in collaboration with the University of Birmingham, QinetiQ and Panorama Antennas Limited.

The objective of FATCAT was to design antennas for communication between vehicles and the roadside infrastructure at 63 GHz. The aim of MILTRANS was broader; to design and demonstrate the operation of a high capacity inter-vehicle and vehicle to roadside data link operating in the 63 and 64 GHz frequency range. Low cost design and fabrication techniques of the data links were also investigated.

MILTRANS decided to use a dual channel, bi-static configuration to build the transceiver circuit. The circuit layout of the configuration is shown in Figure 1.3.

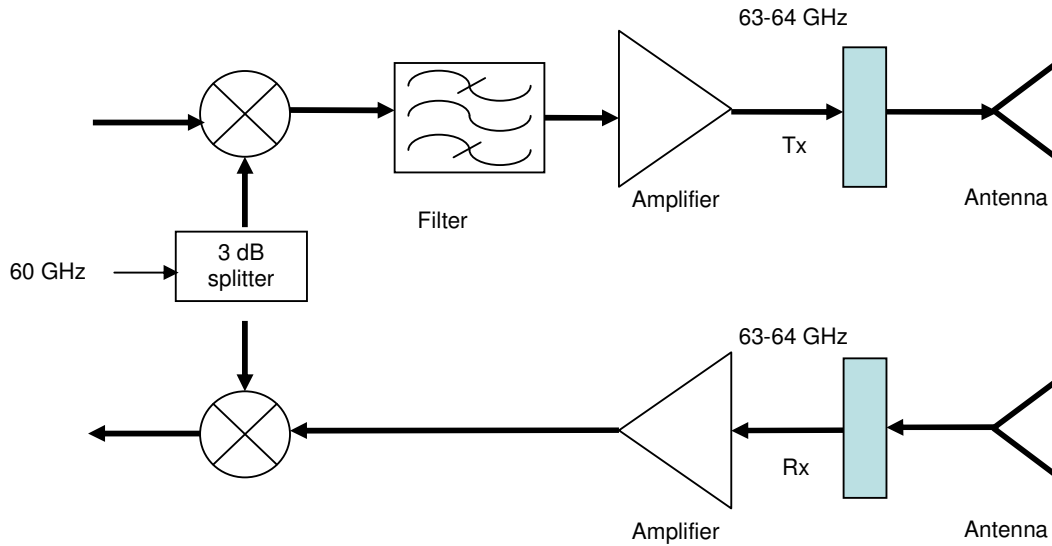


Figure 1.3: A dual channel, bi-static configuration.

This configuration offers the least risky option as transmitting and receiving are in totally separate sections. The isolation between the transmitter and the receiver sections is high because switch is not needed. The incorporation of switch will add more losses to the circuit. The multiplier output is split to supply local oscillation (LO) signals at millimetre wavelength frequency to both the up and down converter circuits. The signal is filtered and amplified before being transmitted. The received signal is amplified before being down converted to an intermediate frequency (IF). The transceiver was demonstrated in microwave monolithic integrated circuit (MMIC) chipset under MILTRANS program [15]. The chipset has three main sections which are i) core chip, ii) frequency multiplier, and iii) transmit amplifier. Transmit and receive output ports are connected to test equipment and antennas by having microstrip to waveguide transitions.

The needs of state of the art systems at higher frequencies will not only bring complexity to the device design, but also complicate the process of fabrication. Most traditional techniques of manufacturing microwave waveguide components use milling and drilling to produce a 3-dimensional (3D) structure. The structure dimensions are limited by the smallest available milling cutter, normally between 150 μm and 200 μm [16].

MMIC technology with gallium arsenide (GaAs) substrate has gained great interest since the 1980's in the manufacture of microwave and millimetre wave circuits. However, at millimetre wavelength frequencies, components in the circuits are physically close together and the energy can couple from one section of the circuits to another by the substrate modes. Interest is growing in new fabrication techniques for three dimensional (3D)-structuring such as surface micromachining, bulk micromachining, thick SU-8 photoresist and wafer bonding [16]. The 3D structuring, with the ability to confine signal within the conductor walls, offers the advantage of avoiding the effects from contiguous lines within a circuit. Micromachining is a machining process capable of fabricating tiny structures, which has sparked the interest of millimetre and sub-millimetre wave researchers. It is a very useful technique in the manufacture of miniature devices. The technique has grown from integrated circuit fabrication technologies [17]. Sub unit substrates used to be implemented in manufacturing integrated circuits, which later on incorporated multiple interfaces [18].

1.2 Motivation and Objective

The objective of this project is to demonstrate the performance of micromachined millimetre wave circuits that would benefit antenna beamforming at 63 GHz , and have potential to be used in V2V and R2V communication systems in the future. **However, this work is not about building the whole system, or even part of it. It is about the development of new micromachined components for a variety of uses. Automobile radar, for example, is only one of the potential applications for the components.** The option of designing and manufacturing the components using micromachining is demonstrated here. Figures 1.4 and 1.5 illustrate the operation of the system together with the long and short range radar systems. The moving vehicle receives general data from the roadside transponder (63 GHz). The sensor uses a radar system (77 GHz) to detect any obstacles or other vehicles, and the car can initiate any necessary actions that need to be taken [19].

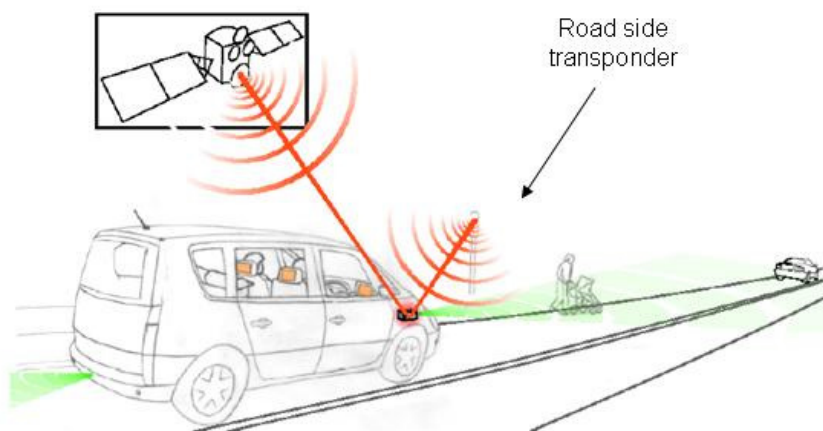


Figure 1.4: System illustration taken from [19].

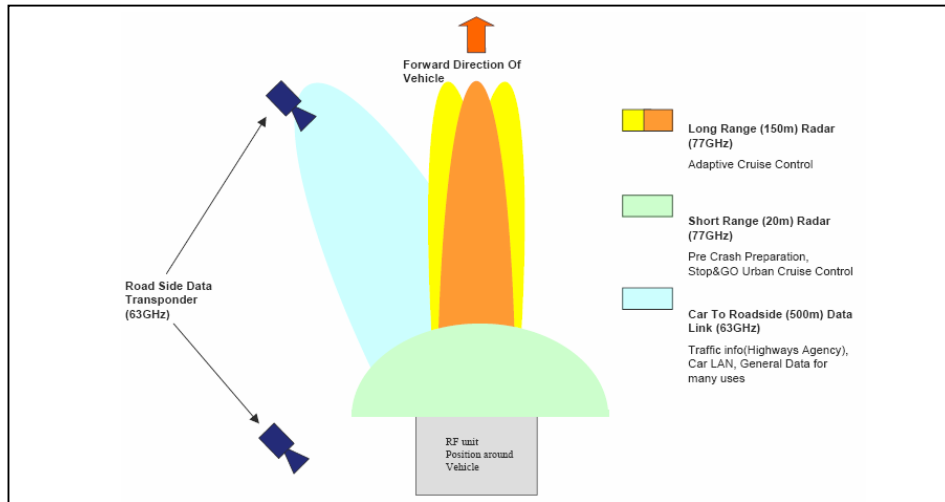


Figure 1.5: 63 GHz and 77 GHz radar system concept taken from [19].

Referring to Figure 1.4 and 1.5, as the vehicle is moving, the transceiver needs an adaptive antenna system that can direct its beam to transmit and receive signals in the desired direction. For example, when the car moves forward, it should be able to detect obstacles at different locations. Therefore, the beam must be switched on to an appropriate bearing. This can be done by rotating the antenna; however, this study proposes that the antenna beam will be formed electronically. The beams for the systems can be formed by implementing a beamforming system such as by using the Butler matrix configuration as shown in Figure 1.6. The matrix has N input ports and the same number of output ports or radiating elements. Signals introduced at particular input ports possess a constant phase difference and the same amount of excitation signal at all output ports. The radiation beam generated at the output port would be at a certain angle due to phase progression through all ports. For instance, if a signal is introduced to port i_1 , phase progression through the circuit will result in the O_{i1} output beam.

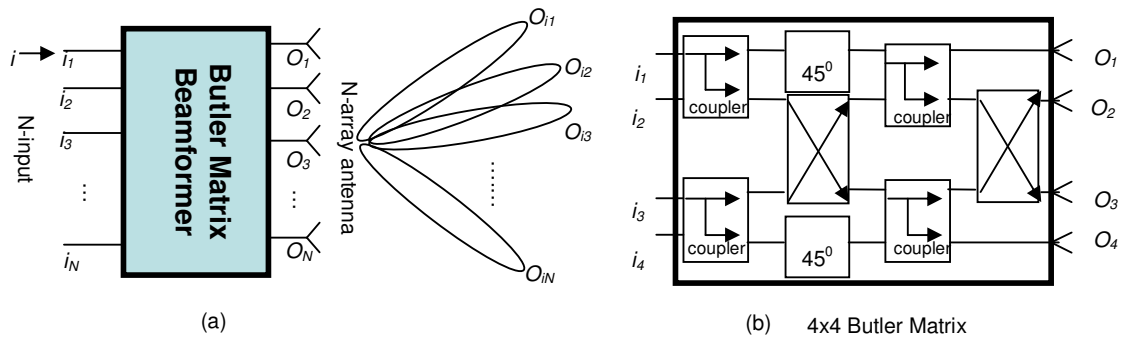


Figure 1.6: Butler Matrix Beamformer.

The above mentioned applications at higher frequencies have raised new interest in systems integration and challenges in transmit/receive antenna circuitry for millimetre wave front ends. As the frequencies increase, the components shrink in size. One of today's challenges at millimetre wavelengths is to integrate components with their interconnections on a single dielectric [6]. Thus, losses at interconnection discontinuities can be minimised, especially on systems that are mobile, such as for inter car communications; where the circuits are attached to a moving vehicle.

Vehicle beamforming systems may have the antenna attached to the Butler matrix configuration before the antenna is mounted directly to the small and lightweight transceiver. The transceiver is an integration of components such as filters, multipliers, switches, amplifiers, mixers, and power splitters. The Butler matrix is build by couplers, phase shifters and crossovers. These components can be made using conventional planar transmission lines such as microstrip and co-planar waveguide. However, the planar conductors provide unwanted effects such as fringing fields, dispersion and coupling

between adjacent lines. These effects are frequency dependent and became significant at millimetre wavelength frequencies.

This study is mainly involved with designing micromachined millimetre wave components and circuits for Butler matrix antennas beamforming at 63 GHz. The structures are designed using five layers of SU-8 photoresist substrate, each having a thickness of 200 μm ; coated in 1.5 μm metal. Figure 1.7 shows an example of a five layer rectangular coaxial line structure. A 3D structure is formed when all layers are bonded together.

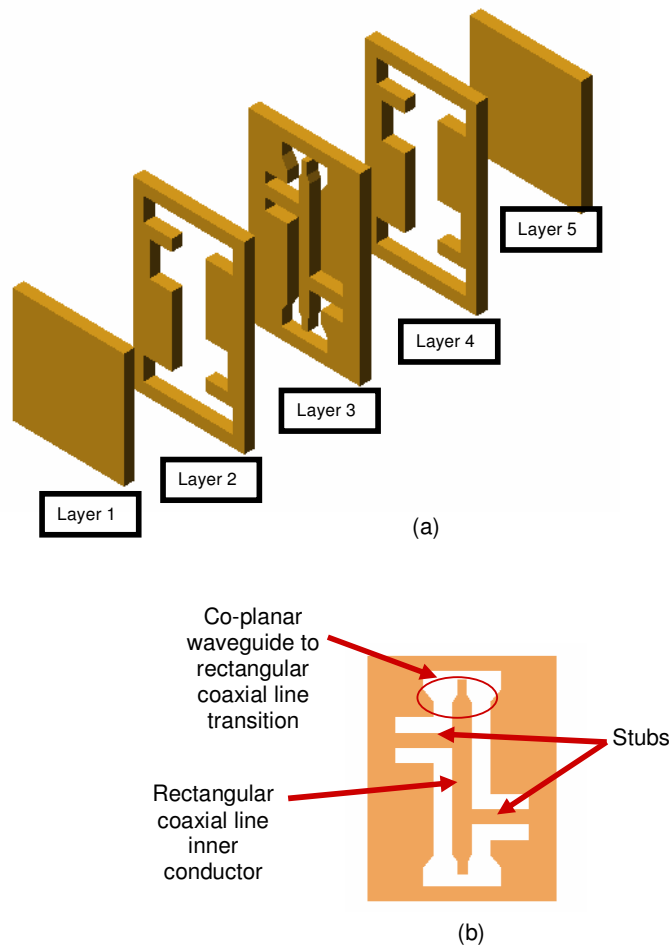


Figure 1.7: Five layers rectangular coaxial line structure; (a) five layers exploded view; and (b) top view of Layer 3, showing the centre conductor of rectangular coaxial line.

The Butler matrix circuit is developed using an air filled rectangular coaxial line. A ridge waveguide is placed to feed the horn and the waveguide slot antennas at the end. Therefore, a transition from the rectangular coaxial line to a ridge waveguide is designed. Low loss transmission lines are used to produce the best possible system performance. Low dispersion coaxial lines are compact in size, making them a suitable guiding structure for millimetre waves. Coaxial lines have the advantage of the signal line being shielded by the outer conductor. Thus, a coupling signal from any contiguous line can be avoided. Furthermore, the dielectric loss can be neglected as it is air filled. The challenge is to design all the suspended lines in the air filled structure.

1.3 Scope of Research

Figure 1.8 shows the research scope. The colours of the boxes differentiate the chapters where the structures are discussed. The components in the blue boxes are presented in Chapter 3, pink in Chapter 4 and yellow in Chapter 5. The arrows represent the flow of the work. All structures are designed in five layers; each layer is a 200 μm metal coated thick SU-8 photoresist, for the micromachining process.

The transmission lines involved in this study are co-planar waveguides, rectangular coaxial lines, ridge waveguides and the transitions. The co-planar waveguide to rectangular coaxial line transition is studied for on-wafer probe measurement purposes. A novel rectangular coaxial line to ridge waveguide transition is designed and manufactured to transfer signal

from the Butler matrix into the feeding waveguide that feeds the horn and the slot waveguide antennas. More details on these transmission lines are discussed in Chapter 3.

There are three antennas studied in this work. They are i) patch antenna, ii) horn antenna and iii) waveguide slot antenna. The horn antenna and the slot waveguide antenna have been fabricated and measured. The antennas performance and physical structures are compared and discussed in Chapter 4.

The antennas are made in array of two elements and attached to the output of the Butler matrix, which will be discussed in Chapter 5. The branch line coupler that built the Butler matrix has been chosen for use in this study due to its simplicity of design. It is made by using rectangular coaxial lines.

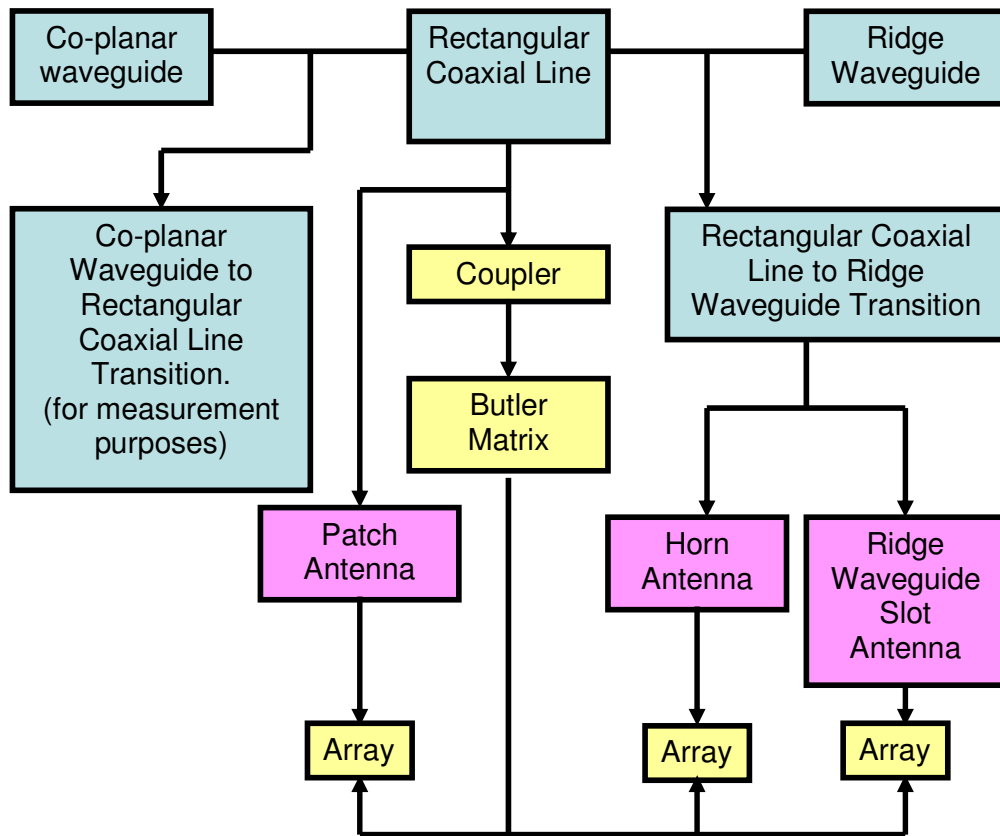


Figure 1.8: Research scope diagram.

1.4 Thesis Layout

The overall idea of the research work is introduced in Chapter 1 along with the motivation and objectives of the research. A brief introduction to each chapter is also given here.

Chapter 2 explains the micromachining process and is focused on the thick SU-8 photoresist technique used to develop structures designed in this work. Although the process is not covered in the project scope, it is important to give an overview of the micromachining and some factors involved that must be taken into account during the design process.

Chapter 3 describes the transmission lines and transitions used in this work. It starts with the introduction of different types of transmission lines before focusing on rectangular coaxial lines, ridge waveguides and also the transition between them. The designs and modelling are presented together with the experimental testing involved.

Antennas are discussed in Chapter 4. Three types of antennas, as mentioned in the scope above, are compared. Except for the patch, the other two antennas are modelled and fabricated with the rectangular coaxial line to ridge waveguide transition designed in Chapter 3. The measurements of fabricated antennas are also presented.

Chapter 5 focuses on Butler matrix beamforming. The concept of beamforming is introduced with the components that build a Butler matrix, which are couplers, phase shifters and crossovers. Different types of couplers are briefly described before focusing on the hybrid quadrature branch line coupler. The integration of the circuits which form a Butler matrix beamformer with an array antenna is presented at the end of the chapter.

Finally, Chapter 6 concludes all research work done together with a presentation of the proposed future work.

References

- [1] D. M. Pozar, *Microwave Engineering*, Third ed.: John Wiley & Sons, 2005.
- [2] J.-S. Hong and M. J. Lancaster, *Microstrip Filters For RF/Microwave Applications*: John Wiley & Sons, 2001.
- [3] H. H. Mainel, "Commercial Applications of Millimeterwaves : History, Present Status, and Future Trends," *IEEE Transactions on Microwave Theory and Techniques*, vol. 43, pp. 1639-1653, 1995.
- [4] D. Gunton, P. Gardner, D. Pansegrouw, and J. Powell, "MILTRANS - A Millimetric Data Link for Transport Applications," in *13th World Congress on Intelligent Transport Systems and Services*, 2006, pp. 1-8.
- [5] "FCC Online Table of Frequency Allocations," 2010.
- [6] D. Liu, *Advanced Millimeter Wave Technologies : Antennas, Packaging and Circuits.*: John Wiley & Sons Ltd, 2009.
- [7] P. Smulders, "Exploiting the 60 GHz Band for Local Wireless Multimedia Access : Prospects and Future Directions," in *IEEE Communications Magazine*. vol. 40, 2002, pp. 140-147.
- [8] O. Andrisano, R. Verdone, and M. Nakagawa, "Intelligent transportation systems: the role of third generation mobile radio networks," *IEEE Communications Magazine*, vol. 38, pp. 144-151, 2000.
- [9] K. M. Strohm, H.-L. Bloecher, R. Schneider, and J. Wenger, "Development of Future Short Range Radar Technology," in *European Radar Conference*, Paris, 2005, pp. 165-168.
- [10] M. Klotz and H. Rohling, "A 24 GHz short range radar network for automotive applications," in *Radar, 2001 CIE International Conference on, Proceedings*, 2001, pp. 115-119.
- [11] "Compatibility Studies Around 63 GHz Between Intelligent Transport Systems (ITS) and Other Systems," CEPT, Harv ECC Report 113, May 2009.
- [12] R. I. Henderson, W. M. A. Qureshi, and B. Kumar, "A Compact Multifunction Automotive Antenna," in *European Conference on Antennas and Propagation*, Edinburgh, UK, 2007, pp. 1-5.
- [13] D. Gunton, B. Pirollo, B. Kumar, J. Powell, D. Bannister, A. Barnes, D. Pansegrouw, P. Gardner, C. Constantinou, E. Lee, A. Lee, T. Lee, R. Hunt, A. Stacey, and C. Moss, "MILTRANS - Millimetric Transceivers for Transport Applications," in *The 5th International Conference on ITS Telecommunications*, 2005.
- [14] T. Y. Lee and F. G. McKinney, "Data Interchangeability between 63 GHz and 77 GHz Vehicular Technologies," in *IET Conference on Automotive Electronics*, London, 2007, pp. 1-3.
- [15] J. R. Powell, P. D. Munday, W. H. A. Tang, R. C. Hunt, and D. J. Gunton, "MMIC and Module Design and Performance for Millimetric Transceiver Front-ends for Transport Applications," in *Microwave Symposium Digest, 2006. IEEE MTT-S International*, 2006, pp. 1497-1500.
- [16] S. Biber, J. Schur, A. Hofmann, and L. P. Schmidt, "Design of new passive THz devices based on micromachining techniques," in *The Fifth International Kharkov Symposium on Physics and Engineering of Microwaves, Millimeter, and Submillimeter Waves*, 2004, pp. 26-31.

- [17] K. J. Vinoy, "Micromachined Components for Millimeter and Sub-Millimeter Wave Systems," in *International Conference on Smart Material Structure and Systems*, Bangalore, India, 2005, pp. 101-108.
- [18] J. Grzyb and G. Troster, "MM-wave microstrip patch and slot antennas on low cost large area panel MCM-D substrates-a feasibility and performance study," *IEEE Transactions on Advanced Packaging*, vol. 25, pp. 397-408, 2002.
- [19] "SLIMSEN - Short and Long Range Integrated Multifunction Radar and Communication Sensors."

Chapter 2

Micromachining

2.1 Introduction

Interest in millimetre wave frequency research has increased due to demands on bandwidth and high data rate communications. The challenge is the fabrication tolerance with the short wavelength in order to prevent cross talk between signal paths and difficulties in routing multiple lines [1]. Conventional metal milling may still be used, but at very high accuracy, which increases the equipment cost. Microfabrication is a parallel process suitable for large scale production at lower cost than conventional milling.

In order to realise low loss structures, different approaches to overcome high attenuation on passive components at millimetre wave were investigated. One of the approaches involved the use of highly resistive silicon in order to reduce the substrate losses. However, fabrication in standard metal oxide semiconductor (CMOS) use low resistivity silicon [2]. Another approach is micromachining.

Micromachining and microelectromechanical systems (MEMS) evolved from integrated circuit and microsystem technology. MEMS components can be considered micromachined components. However, manufactured micromachined components without reconfigurable actuators involved in converting a control voltage or current into mechanical movement cannot be considered MEMS components [3]. In the late 1980's researchers referred to micromachining as a field that focused on the use of silicon [4]. Nowadays, micromachining has evolved with various techniques.

This chapter presents details micromachining, a machining process designed to manufacture tiny structures with great accuracy. Different micromachining techniques and technologies are briefly reviewed first, followed by a discussion of the thick SU-8 photoresist micromachining technique implemented in this work. All structures in this thesis were designed to consist of five metal-coated SU-8 layers with equal thickness. All the layers are arranged to fit into the 4-inch SU-8, thus only one mask is needed for each device. The five layer scheme is chosen as a minimum number of layers upon which to build the rectangular coaxial line used in this study. This will minimise possible losses that may occur between layers.

2.2 Micromachining Fabrication Techniques

Micromachining has grown in popularity due to its potential to achieve small structures with great accuracy at a reduced cost. Micromachined transmission lines, high-Q resonators, filters and antennas are categorised in one of four distinct areas in radio-frequency (RF) microelectromechanical systems (MEMS) research [5]. The other three are: 1) RF MEMS switches, varactors and inductors; 2) thin film bulk acoustic resonators and filters; and 3) RF micromechanical resonators and filters. Micromachining techniques can be categorised into bulk micromachining or surface micromachining. Bulk micromachining consists of wet and dry etching, and photoresist technologies. Photoresist technologies involve photolithography using either X-ray or ultraviolet (UV) light sources. Bulk micromachining, as well as surface micromachining, is also used in membrane technology. The surface micromachining process involves thin film growth on the surface of a substrate. The differences between bulk and surface micromachining are presented in [6]. The thickness of the wafer used determines the vertical dimension of the bulk micromachined structures, which is between 100 to 500 μm . However, in surface micromachined structures, the vertical dimension is determined from the practical thickness of thin film that can be deposited, which is between 0.5 and 2 μm [6]. Further discussion on micromachining fabrication techniques are presented in the next sections.

2.2.1 Bulk Micromachining

The main process in bulk micromachining is the etching. There are two etching techniques; wet etching and dry etching [7]. The advantage of wet etching is that more than one wafer can be processed at a time. However, dry etching is preferred in achieving vertical walls. The extent of the etching can be controlled by using layers of different materials. The changes of material that determine the depth of etching is called the etch stop [8]. There are three ways of implementing etch stop [8]: 1) silicon-on-insulator (SOI) wafer where different materials are grown layer by layer on one side of a wafer; 2) doping on material; and 3) electrochemically by applying a voltage across a p-n junction that prevents some etchants from affecting the n-type material.

Wet etching can be either isotropic or anisotropic. Isotropic requires etching to progress at the same rate in all directions. For silicon etching, a hydrofluoric, nitric and acetic acid (HNA) etch system is commonly used. A mixture of nitric acid (HNO_3) and hydrofluoric acid (HF) is diluted with water or acetic acid. Isotropic etching can be done at room temperature at a faster rate compared to anisotropic etching [7]. However, isotropic etching is used less frequently than anisotropic [8]. This is because the isotropic etchant attacks a wide area around the structure and consequently may weaken the performance of the device. An example of cantilever design with isotropic and anisotropic etching is shown in Figure 2.1 (a) and (b), respectively [8]. The figures show that the isotropic etching etched a massive area around the structure.

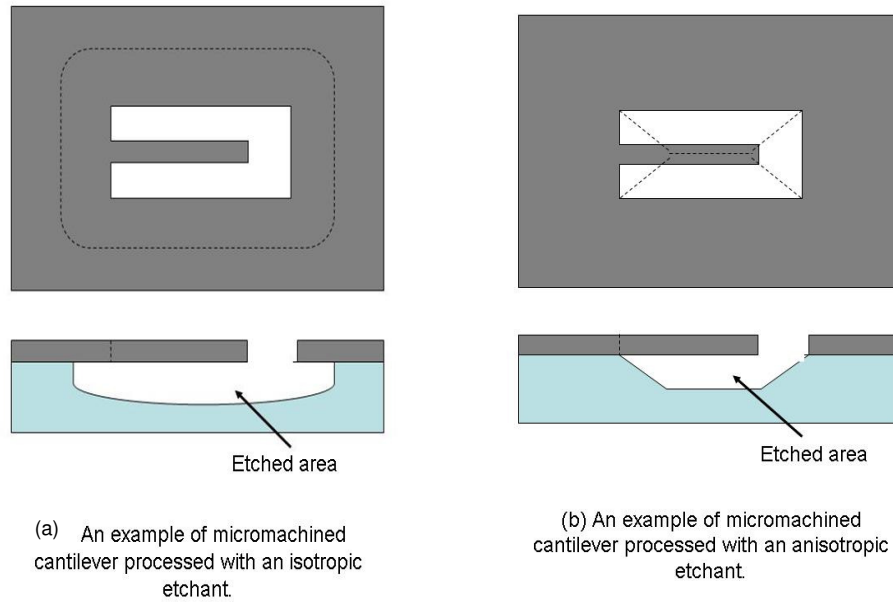


Figure 2.1: Isotropic and anisotropic etched cantilever structure [8].

Anisotropic etching is restricted by the crystalline structure of the material used and usually has different etching rates in different directions. A solution of potassium hydroxide (KOH) mixed with water, and sometimes with the addition of alcohol, is the most commonly used etchant. The silicon etch rate is influenced by the process temperature [7].

In contrast to wet etching, dry etching needs sophisticated equipment. It is normally done in an evacuated chamber where plasma is generated and used to etch the silicon substrate. Deep Reactive Ion Etching (DRIE) is the most common dry etching process. The wafer is exposed alternately to an etchant and passivant to control the side wall of the structure. The etchant is the plasma of sulphur hexafluoride (SFC), while the passivant is octafluorocyclobutane (C_4F_8). This technique requires expensive equipment and is not efficient for etching layers approximately 0.5 mm and above [9].

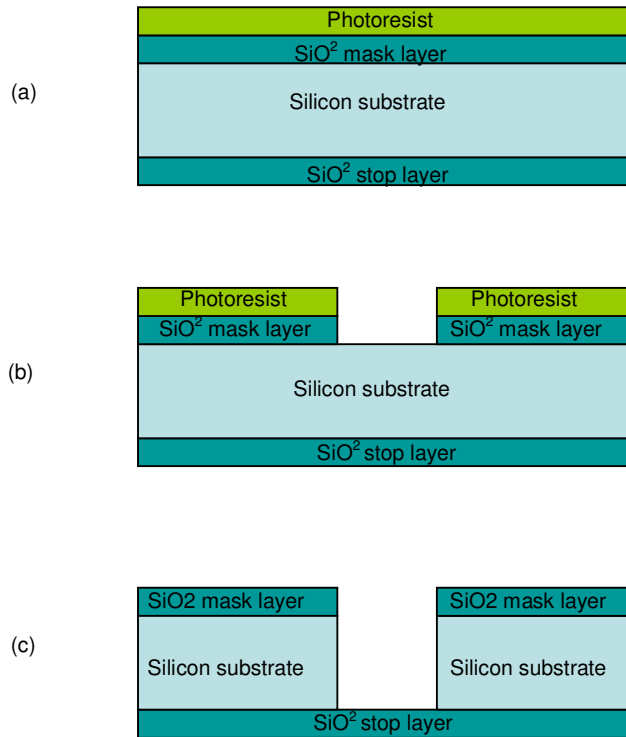


Figure 2.2 : DRIE manufacturing technique [10].

As an example, the DRIE process was implemented in fabricating W-band waveguide in [10]. The process is shown in Figure 2.2. The silicon substrate was cleaned before both sides were deposited by SiO_2 . The top SiO_2 layer, which was $3.5 \mu\text{m}$ thick, was used as a mask for deep silicon etching while the bottom layer, at $0.6 \mu\text{m}$, was used as the etch stop. A photoresist layer was deposited on top of the SiO_2 mask layer (Figure 2.2 (a)). The photoresist was developed and the SiO_2 was patterned (Figure 2.2 (b)). The silicon substrate layer was etched using the DRIE BOSCH process. The etch stop layer determined the depth

of the etching (Figure 2.2 (c)). The SiO₂ layers were then removed before the silicon substrate was metallised by sputtering Ti and Cu.

2.2.1.1 LIGA

LIGA is a German acronym for lithography, electroforming and moulding [8]. It can be categorised into two fabrication technologies. One is X-ray LIGA which uses X-rays produced by a synchrotron and the second is UV LIGA which uses ultraviolet light. X-ray light has a higher resolution and a shorter wavelength and is able to create high aspect ratio structures with parallel and smooth side walls. However, it is more expensive compared to ultraviolet (UV) light sources. Figure 2.3 shows the principal fabrication steps of UV LIGA [11]. A thick photoresist layer is exposed before being developed (Figure 2.3 (a)). For X-rays, a special sophisticated mask is required for this process step. For UV LIGA a chromium mask can be used. The photoresist is developed (Figure 2.3 (b)) to be used as a mould for galvanofarming (Figure 2.3 (c)) or electroforming where material is deposited by means of an electric current or by means of reactive chemical mixtures. Components are created by electro-deposition when the photoresist mould gap is filled with filling material. Finally, the photoresist is stripped away, leaving the metal structure (Figure 2.3 (d)). The released components can be used for injection moulding.

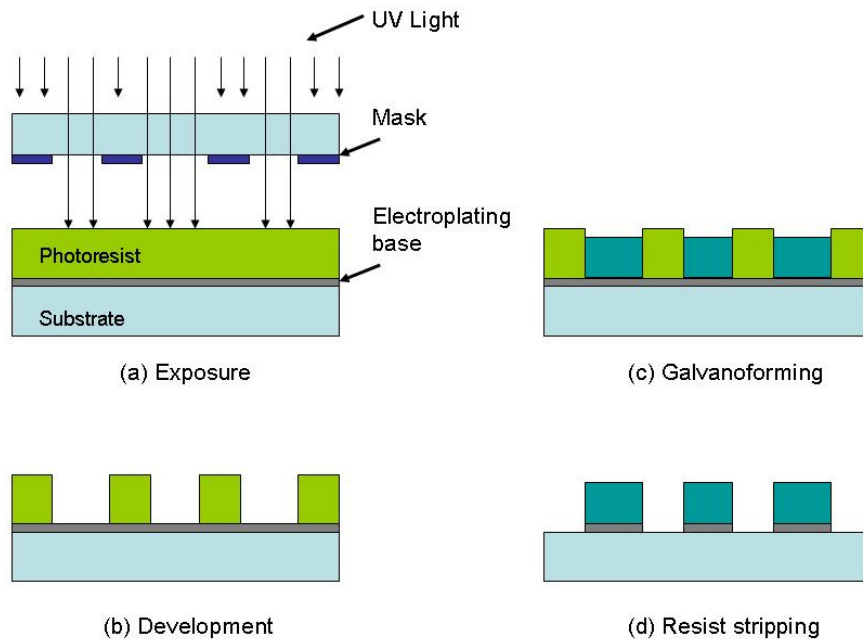


Figure 2.3: UV LIGA fabrication steps [11].

2.2.1.2 Membrane Technology

Membrane technology in micromachining first gained attention due to its ability to produce thick pieces at high aspect ratios [12]. A thin layer of high quality dielectric material is applied to support a suspended structure. The etch stop discussed earlier is very useful in fabricating membranes. Membrane technology is commonly used in integrating micromachined transmission lines and antennas. In antenna design, the idea is to have a

cavity underneath the radiator, thus reducing the effective permittivity of the substrate and consequently minimising losses due to surface waves.

For instance, a membrane supported patch antenna was presented in [13]. The manufacturing process is depicted in Figure 2.4.

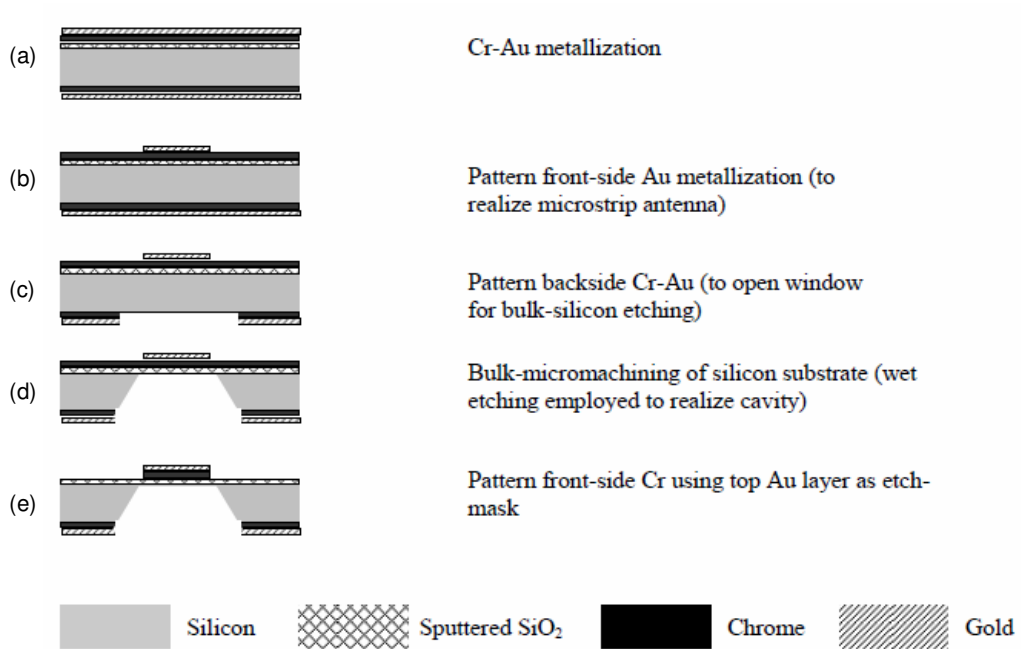


Figure 2.4: Membrane supported transmission line taken from [13].

The process in Figure 2.4 starts with a 2 μm layer of SiO₂ deposited on the silicon substrate before it was metallised by 3 μm thick Cr and Au on both sides (Figure 2.4 (a)). Then, the Au layer on the front side was patterned to realise the patch antenna (Figure 2.4 (b)). The back side was patterned as an open window for the bulk micromachining etching process (Figure 2.4 (c)). An anisotropic wet etch was applied to remove the silicon substrate

underneath the circuit area to obtain a thin layer membrane (Figure 2.4 (d)). Finally, the Cr layer was patterned (Figure 2.4 (e)).

Other examples of the implementation of membrane technology are the membrane supported transmission lines and Ka-band microwave filter presented in [14]. The top view of the filter structure and the 3D view of the CPW line on the membrane are shown in Figure 2.5 and 2.6, respectively. A 1 μm silicon nitride membrane layer was deposited on a 525 μm thick silicon substrate before part of the substrate underneath the circuit was etched away. The circuit was patterned on the membrane surface. A metallised substrate was bonded to form a ground layer and to support the structure.

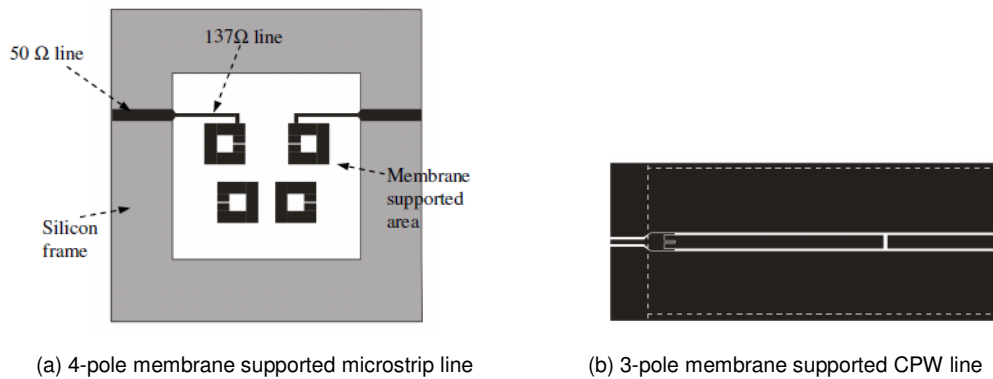


Figure 2.5: Microwave filters taken from [14].

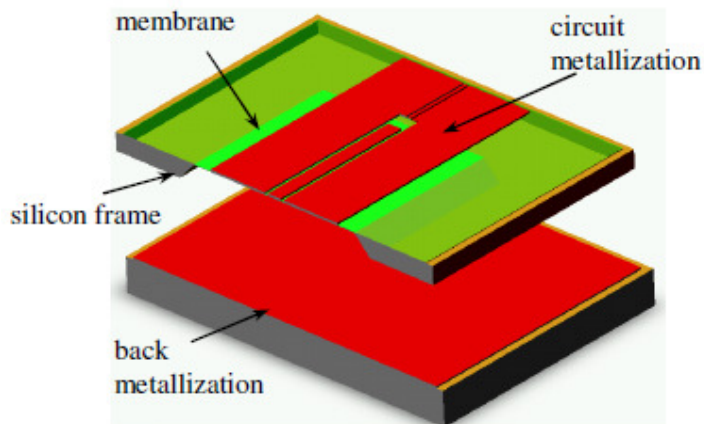


Figure 2.6: Membrane supported transmission line taken from [14].

Membrane technology is also implemented in the manufacture of MEMS switches. The movable bridge membrane allows the switch to turn on and off. The fabrication usually involves the surface micromachining process, which will be presented in the next section.

2.2.2 Surface Micromachining

The surface technique selectively adds and removes a deposit film on the wafer [15]. The process involves wet and dry etching together with thin film deposition. The thin film (normally about 1 μm) can be polysilicon, silicon oxide or nitrite. A soluble layer, normally

silicon dioxide, is deposited beneath other patterned materials for later removal. The layer is referred to as a sacrificial layer.

A chemical wet etching of the sacrificial layer is the main process in surface micromachining. A soluble or removable sacrificial layer is used to temporarily support the structural layers during subsequent fabrication steps. It must be stable during deposition and throughout the fabrication process and etched away quickly during the release step. The sacrificial layer can be metal (such as Au, Ni or Al), dielectric (SiO_2 or Si_3N_4), polymer (photoresist or polymethyl) or polyimide [7].

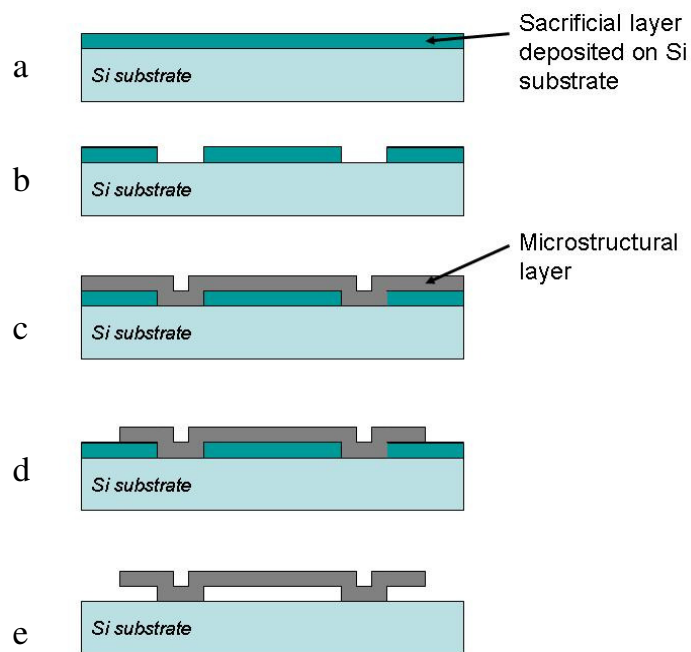


Figure 2.7: An example of surface micromachining process steps [16].

An example of the surface micromachining steps is illustrated in Figure 2.7 [16]. A silicon substrate was deposited with a sacrificial layer and coated with a dielectric layer as an

isolation layer (Figure 2.7 a). Then, the layer was patterned with the first mask (Figure 2.7 b) before a microstructural thin film layer was deposited (Figure 2.7 b). The microstructural layer, the layer that forms the structure, should be designed with good mechanical and electrical properties. The layer was patterned with a second mask (Figure 2.7 d) before being released with an etching step to remove the sacrificial layer (Figure 2.7 e).

Surface micromachining was used in the manufacture of an RF MEMS capacitive switch in [17]. The process is depicted in Figure 2.9. A 1 μm thick SiO_2 layer was grown on the substrate before the switch electrode was patterned from 0.4 μm thick deposited metal and insulated by a layer of patterned PECVD (Plasma Enhanced Chemical Vapour Deposition) silicon nitride (Figure 2.8 (a)). The insulation was for DC isolation. A 4 μm thick layer of aluminium alloy was evaporated and patterned to define the metal transmission line and the mechanical support before a sacrificial layer was applied and planarized to get a planar and smooth layer (Figure 2.8 (b)). Then, an aluminium membrane layer less than 0.5 μm was deposited and patterned to form the switch membrane (Figure 2.8 (c)). The membrane bridge was released by using the plasma etching process (Figure 2.8 (d)). Without any potential applied, the bridge will remain suspended. The bridge will be pulled down to the dielectric covered metal electrode when the application of an electrostatic field between the bridge and the electrode is strong enough. This creates a capacitive connection between the CPW centre conductor and the ground planes.

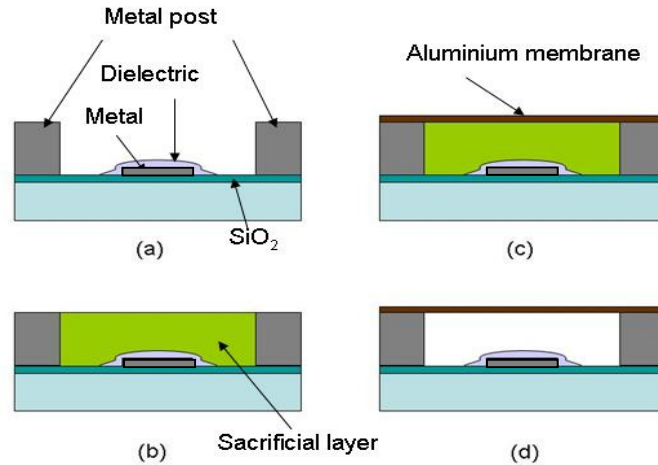


Figure 2.8: Capacitive switch fabrication process taken from [17].

2.3 Thick SU-8 Photoresist Technique

The thick photoresist technique presented here lets the photoresist remain as part of the structure. The patterned photoresist pieces are coated with metal and assembled to form a structure. It is different from other processes such as LIGA where the photoresist acts as a mould and is removed at the end of the process.

SU-8 is a negative epoxy based photoresist, initially developed by IBM for MEMS applications [18]. It has become of interest for high-aspect ratio (HAR) and three-dimensional (3D) lithography patterning due to its outstanding coating processing properties. Furthermore, it is mechanically and chemically stable, making it suitable for permanent use applications [19].

A normal process in thick SU-8 photoresist micromachining typically involves the following steps: spin coat, soft bake, expose, post expose bake (PEB) and develop. Once developed, the pieces are coated with metal before being aligned and bonded together to form a structure. The recipe used in this thesis is shown in Table 2.1 and described below with a diagram of the process in Figure 2.9. All the processes detailed here were done at the University of Birmingham.

Table 2.1: The thick SU-8 micromachining recipe for 200 μm layer thickness as used in this thesis.

PROCEDURE STEPS	PROCESS PARAMETERS
Substrate pre-treatment	200°C for 5 min
SU-8 Dispense	4 ml
Spread	300 rpm for 5 s
Spin Coat	1000 rpm for 30s
Soft Bake	65°C for 10 min. and 95°C for 75 min
Expose	500 mJ
Post Expose Bake	65°C for 2 min. and 95°C for 20 min
Develop	20 minutes in EC solvent
Hard Bake	150°C for 30 min.
Metalise	1.5 μm of Au (Gold)
Alignment and Bonding	Adhesive

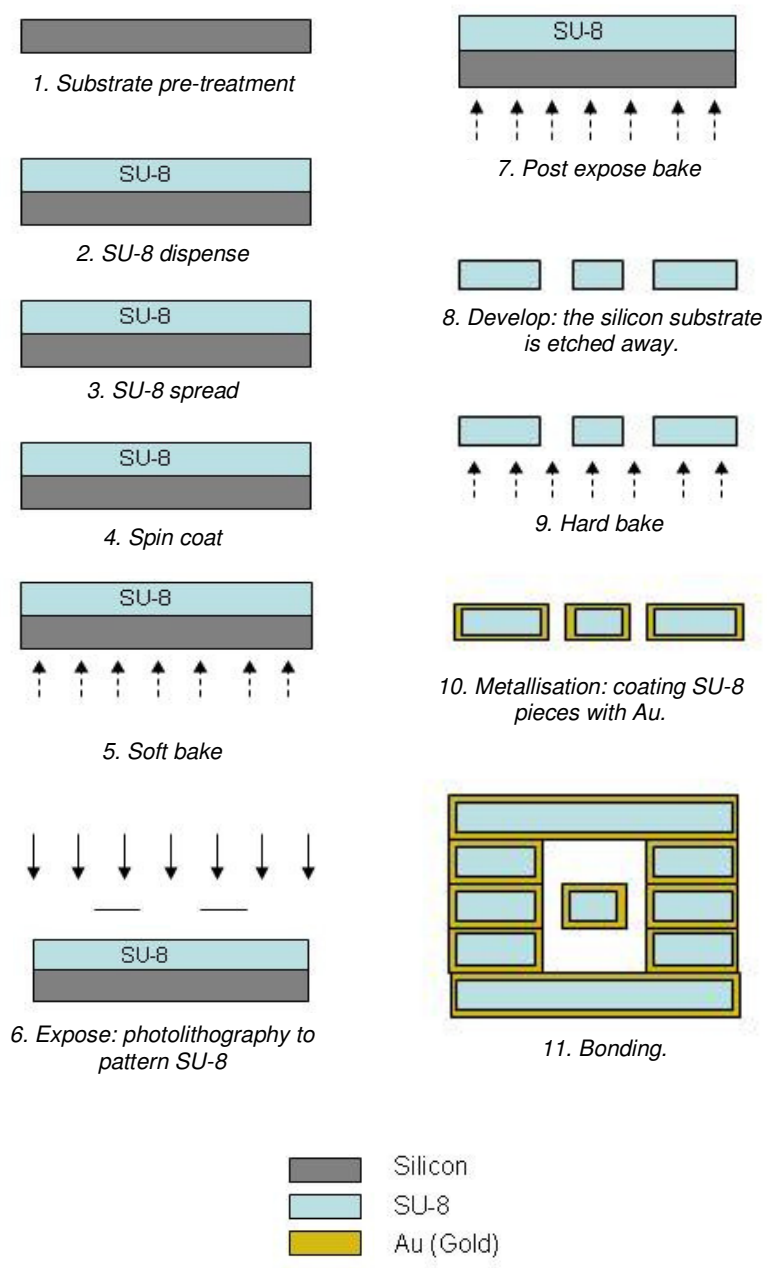


Figure 2.9: The process of fabrication and assembly.

The process can be described as follows.

1. *Pre-treatment* - In order to obtain maximum process reliability, the silicon substrate is pre-treated. It is rinsed with dilute acid followed by water. To dehydrate the surface, it is put on a hotplate at 200°C for 5 minutes.
2. *SU-8 Dispense* - The process starts with a static dispensation of around 4 ml SU-8 on a 4 inch silicon substrate. The amount for different viscosities can be approximated from the data sheet. However, some optimization has been made to obtain a more accurate level.
3. *Spread* - The SU-8 is spread with a 300 rpm spin.
4. *Spin coat* - The SU-8 is spin coated with a 1000 rpm for 30 seconds.
5. *Soft bake* - A soft pre-bake is stepped from 65°C for 10 minutes to 95°C for 75 minutes on a levelled hotplate. This is done to evaporate the solvent inside the film. The stepping temperature is used to allow the evaporation process to be more controllable at a lower initial bake temperature. This could result in better coating fidelity, reduced bead and better resistance to substrate adhesion [19].
6. *Expose* – The exposure dose is 500 mJ for a 200 µm thick SU-8 layer. The SU-8 coated silicon and the mask are placed in the mask aligner and exposed to UV light from a mercury lamp.
7. *Post Exposure Bake (PEB)* – The PEB is done to selectively cross link the exposed portions of the film. Again, a two step hot plate contact process is done to minimize stress, wafer bowing and to resist cracking. The post bake is stepped from 65°C for 2 minutes to 95°C for 20 minutes.

8. *Develop* – Ethyl lactate (EC) solvent is used to develop the SU-8 pieces. The wafer is agitated in the solvent for about 20 minutes before being rinsed with isopropyl alcohol and dried with a gentle stream of air.
9. *Hard Bake* –The processed wafer is hard baked at 150°C. After 30 minutes, the hotplate is switched off and the wafer is left on the hotplate, allowing it to cool down gradually. This will help to reduce the stress. The hard bake is done to keep the pieces stable during subsequent processing.
10. *Metallization* – The pieces would be susceptible to bending during this coating process without the hard bake. The SU-8 pieces are first sputter-coated with a 5nm Cr adhesion layer, followed by a 1.5 μm thick thermally evaporated gold layer. The thickness of the gold is about five skin depth at 63 GHz, which is thick enough to prevent the signal from penetrating into the SU-8. Skin depth is the distance where the amplitude of the fields in the conductor decays by an amount of 1/e or 36.8 %. It can be calculated by [20]

$$\delta_s = \sqrt{\frac{2}{\omega\mu\sigma}} = \sqrt{\frac{2}{\pi f\mu_0\sigma}} \quad (2.1)$$

It can be seen from (2.1) that the skin depth is inversely proportional to the frequency (f) and the conductance of the material (σ).

11. *Bonding* – The pieces are aligned and bonded together using a conducting adhesive material.

During the process, some imperfections between the joined layers can be apparent. This can contribute to loss and degradation in the performance of the structure. Losses between each layer may be contributed to by i) excessive or insufficient adhesion material during the

bonding process, resulting in imperfect walls as shown in Figure 2.10, ii) planarization problems, or iii) misalignment between layers during the bonding process. The absence of adhesive material at the edge results in a small cavity on the wall. A second evaporation on the inside wall as shown in Figure 2.11 can be implemented to improve the imperfect wall should one develop during the bonding process.

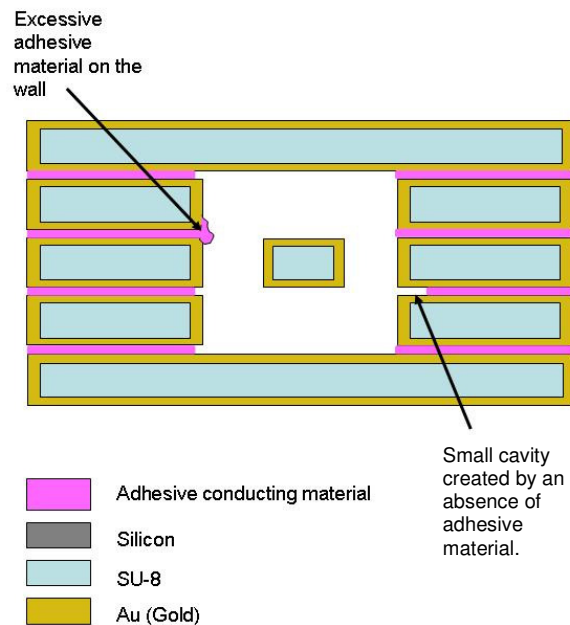


Figure 2.10: Wall imperfection.

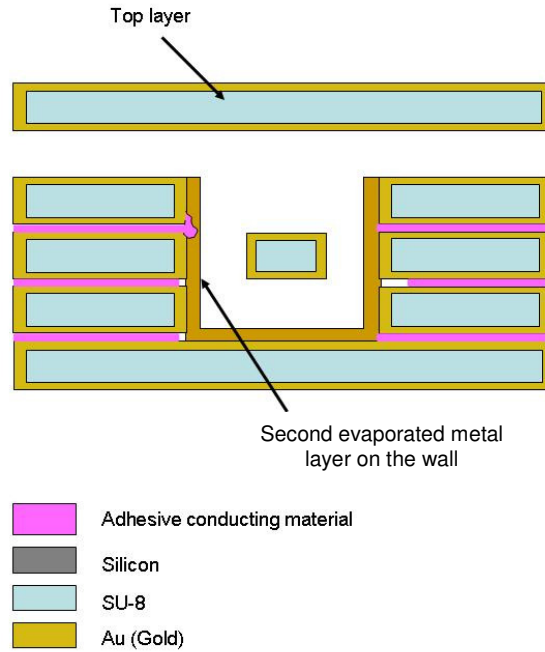


Figure 2.11: Second evaporation on the imperfect wall before assembling the top layer.

The Emerging Device Technology (EDT) group at the University of Birmingham improved the performance of a cavity filter (Figure 2.12) using the second evaporation technique [21]. 2 μm gold was applied inside the cavity before the top layer was placed to enclose the structure. The insertion loss of the filter has been improved from 1.72 dB to 1.01 dB.

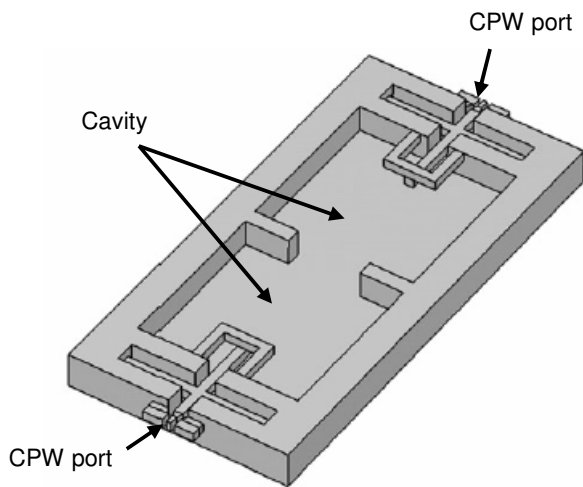
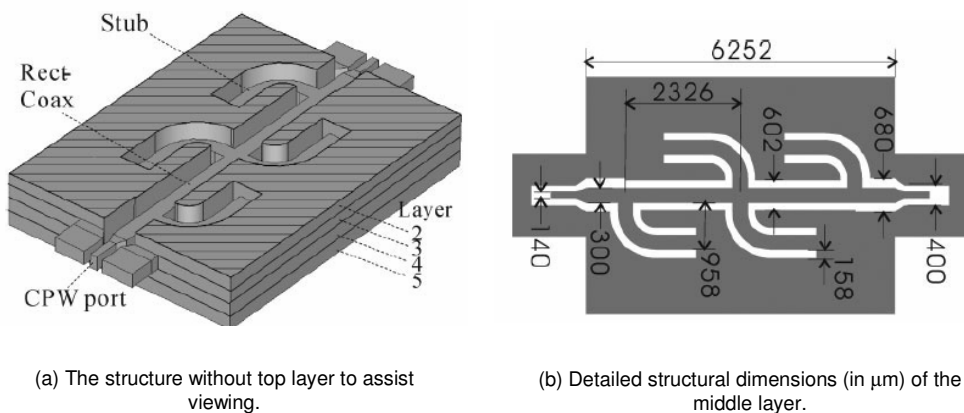


Figure 2.12: The cavity filter structure without the top layer taken from [22].



(a) The structure without top layer to assist viewing.

(b) Detailed structural dimensions (in μm) of the middle layer.

Figure 2.13: (a) The structure and (b) the dimensions of middle layer taken from [23].

The Emerging Device Technology (EDT) group at the University of Birmingham has produced numerous publications on thick SU-8 photoresist micromachined structures. For

example, a low loss rectangular coaxial cable operating in the 28 to 48 GHz range was presented in [23]. It was built by bonding five layers of metal coated SU-8 photoresist pieces. The suspended line of the coaxial line inner conductor was supported by shorted quarter wavelength bent stubs. The structure is shown in Figure 2.13. An average loss 0.057 dB/mm has been achieved.

Another example are the interdigital filters designed at 60 GHz centre frequency presented in [24]. The interdigital filter structure is shown in Figure 2.14. The structure was built by using the five layer thick SU-8 photoresist technique discussed above with each layer 200 μm thick. An insertion loss of 1.1 dB was achieved from the measurement.

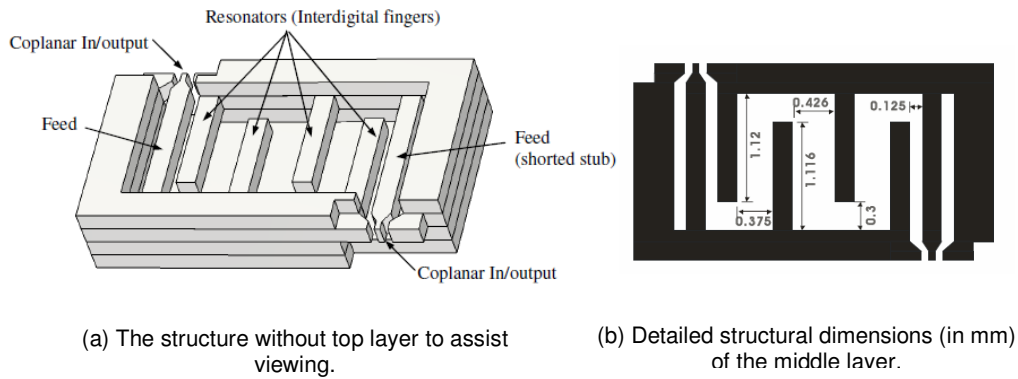


Figure 2.14: (a) The structure and (b) the detail dimensions of middle layer taken from [24].

2.4 Summary

Different micromachining techniques have been briefly discussed in this chapter. Bulk and surface micromachining are mature techniques with the emphasis on the etching process to control the side walls. The bulk micromachining process removes selective parts of the material to form a structure, while surface micromachining forms a structure by growing or adding thin films (0.5 to 2.0 μm) on top of a silicon wafer or other substrate layer. The use of a sacrificial layer in the latter technique lends flexibility to the structure. However, low aspect ratios require a search for different photoresists to obtain precise structures at high aspect ratios [25].

The suitability of fabricating microwave components using three different micromachining technologies were investigated in [18]. The technologies were i) SU-8 photoresist, ii) Si deep reactive ion etching (DRIE), and iii) electroforming. It was claimed that these three technologies were able to produce accurate defined thick pieces [18]. The technologies were used to construct various coaxial lines operating in the 20 GHz to 50 GHz range. Excellent microwave performance was obtained for SU-8 and etched silicon devices, but not for electroplated Ni ones. In addition, SU-8 was found to produce the most accurate pieces with a deviation angle of 0.15° on the lateral sidewall, which is the lowest compared to 0.6° obtained from Ni electroplating and 1° from DRIE. Therefore, the thick SU-8 photoresist technique has been chosen here in this work. SU-8 is not only more accurate, but also chemically and thermally stable, with a lower cost.

A very thick SU-8 layer can achieve an excellent aspect ratio of 1:50 [9] In this work, devices are built in layers; therefore a proper design at each layer is necessary to achieve a whole structure with minimum loss. For the millimetre wave devices designed in this study,

all five layers can be processed simultaneously on the 4 inch silicon wafer. The devices will be discussed further in Chapters 3, 4 and 5.

References

- [1] J. R. Reid, V. Vasilyev, and R. T. Webster, "Three dimensional micromachining for millimeter-wave circuits," in *Wireless and Microwave Technology Conference*, 2009, pp. 1-4.
- [2] L. L. W. Leung, H. Wai-Cheong, and K. J. Chen, "Low-loss coplanar waveguides interconnects on low-resistivity silicon substrate," *IEEE Transactions on Components and Packaging Technologies*, vol. 27, pp. 507-512, 2004.
- [3] S. Lucyszyn, "Review of radio frequency microelectromechanical systems technology," *IEE Proceedings - Science, Measurement and Technology*, vol. 151, pp. 93-103, 2004.
- [4] C. Liu, *Foundations of MEMS*: Pearson Education Inc., 2006.
- [5] G. B. Rebeiz, *RF MEMS : Theory, Design, and Technology*: John Wiley & Sons, 2003.
- [6] P. J. French and P. M. Sarro, "Surface Versus Bulk Micromachining: a Contest for Suitable Applications " *Journal of Micromechanics and Microengineering*, vol. 8, pp. 45-53, 1998.
- [7] B. G. Duixian Liu, Ullrich Pfeiffer, Janusz Grzyb, "Advanced Millimeter-wave Technologies," 2009.
- [8] R. W. Johnstone and M. Parameswaran, *An Introduction to Surface Micromachining*: Kluwer Academic Publisher, 2004.
- [9] Y. Wang, M. Ke, M. J. Lancaster, and F. Huang, "Micromachined Millimeter-wave Rectangular Coaxial Branch-Line Coupler with Enhanced Bandwidth.," *IEEE Transaction on Microwave Theory and Techniques*, vol. 57, pp. 1655-1660, 2009.
- [10] L. Yuan, P. L. Kirby, and J. Papapolymerou, "Silicon Micromachined W-Band Folded and Straight Waveguides Using DRIE Technique," in *Microwave Symposium Digest, 2006. IEEE MTT-S International*, 2006, pp. 1915-1918.
- [11] Q. Wenmin, C. Wenzel, A. Jahn, and D. Zeidler, "UV-LIGA: a promising and low-cost variant for microsystem technology," in *Conference on Optoelectronic and Microelectronic Materials Devices*, 1998, pp. 380-383.
- [12] M. Ke, Yi Wang, Kyle Jiang, M. J. Lancaster, "Micromachined Rectangular Coaxial Line and Cavity Resonator for 77 GHz Applications Using SU8 Photoresist," in *Asia Pacific Microwave Conference, 2008*, Hong Kong, 2008, pp. 1-4.
- [13] S. Preeti, K. K. Shiban, and C. Sudhir, "Design and development of microstrip patch antenna at Ka-band using MEMS technology," 2006, p. 61721F.

- [14] Y. Wang, M. J. Prest, and M. J. Lancaster, "Membrane Supported Transmission Lines and Filters," in *European Microwave Conference 2008*, pp. 1133-1136.
- [15] J. M. Bustillo, R. T. Howe, and R. S. Muller, "Surface Micromachining for Microelectromechanical Systems," in *Proceedings of The IEEE*. vol. 86, 1998, pp. 1552-1574.
- [16] M. J. Madou, *Fundamentals of Microfabrication : The Science of Miniturization*: CRC Press, 2002.
- [17] C. L. Goldsmith, Z. Yao, S. Eshelman, and D. Denniston, "Performance of Low Loss RF MEMS Capacitive Switch," *IEEE Microwave Guided Wave Letter*, vol. 8, pp. 269-271, 1998.
- [18] M. L. Ke, Y. Wang, X. Wei, K. Jiang, and M. J. Lancaster, "Precision Microfabrication of Millimetre Wave Components," in *Laser Metrology and Machine Performance IX*, 2009.
- [19] "NanoTM SU-8 Negative Tone Photoresist".
- [20] D. M. Pozar, *Microwave Engineering*, Third ed.: John Wiley & Sons, 2005.
- [21] Y. Wang, M. L. Ke, and M. J. Lancaster, "Micromachined 38 Ghz Cavity Resonator and Filter with Rectangular Coaxial Feed Lines," *IET Microwave Antennas Propagation*, vol. 3, pp. 125-129, 2009.
- [22] Y. Wang, M. Ke, and M. J. Lancaster, "Micromachined 38 GHz cavity resonator and filter with rectangular-coaxial feed-lines," *Microwaves, Antennas & Propagation, IET*, vol. 3, pp. 125-129, 2009.
- [23] M. Ke, Y. Wang, and M. J. Lancaster, "Design and realisation of low loss air-filled rectangular coaxial cable with bent quarter-wavelength supporting stubs," *Microwave and Optical Technology Letters*, vol. 50, pp. 1443-1446, 2008.
- [24] Y. Wang, M. Ke, and M. J. Lancaster, "Micromachined 60 GHz Air Filled Interdigital Bandpass Filter," in *International Workshop on Microwave Filters* Toulouse, France, 2009.
- [25] E. Koukharenko, M. Kraft, G. J. Ensell, and N. Hollinshead, "A Comparative Study of Different Thick Photoresist for MEMS applications," *Journal of Material Science : Materials in Electronics*, vol. 16, pp. 741-747, 2005.

Chapter 3

Micromachined Transmission Lines and Transitions

3.1 Introduction

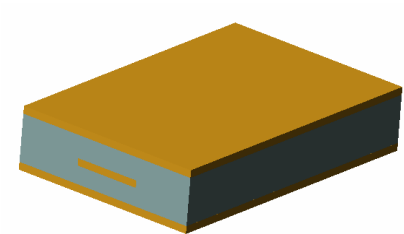
Planar transmission lines, namely microstrip, stripline and coplanar waveguide, have provided flexibility in microwave and millimetre wave integrated circuit designs for decades. However, they are some drawbacks that degrade the performance of the designed circuits, such as parasitic coupling and radiation, increased ohmic coupling, dielectric losses and dispersion [1]. Other than dielectric and radiation losses, microwave circuits also suffer from conductor losses. It is well known that surface resistance is proportional to the square root of the frequency. Therefore, conductor losses are very significant at millimetre wavelength frequencies. Furthermore, at millimetre wavelength frequencies, the circuit blocks, including the antenna, are close to each other and tend to couple signals. Non-planar

structures such as waveguide are able to confine signals along the direction mitigating circuit losses. There have been numerous efforts to obtain a low loss and low dispersion transmission lines at millimetre wave. Recent advances in manufacturing techniques, such as micromachining, have led a revolution in geometries and integration of three dimensional configurations. The integration needs a smooth transition between different transmission lines to ensure efficient signal transfer.

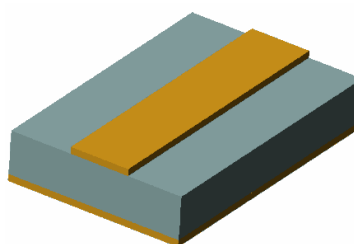
This chapter discusses the micromachined transmission lines and transitions involved in this work. A brief description of a general transmission line is given at the beginning of the chapter to introduce the parameters used in this thesis. This is followed by a discussion of the micromachined lines and transitions considered in this research. They are the rectangular coaxial line, co-planar waveguide (CPW), ridge waveguide and their transitions. The co-planar waveguide and its transition to the rectangular coaxial line are studied here for measurement purposes. It also acts as a transition between a three dimensional structure and planar circuitry.

3.1.1 Transmission Lines

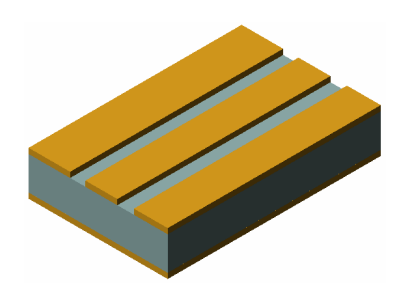
A microwave transmission line is a structure that guides a microwave signal from one point to another. Microwave transmission lines such as striplines, microstrip lines and coaxial cables have been studied for decades.



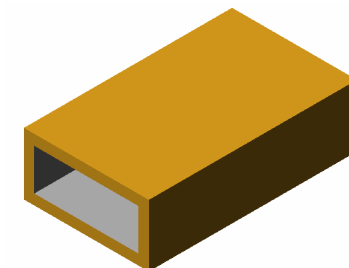
(a) Stripline



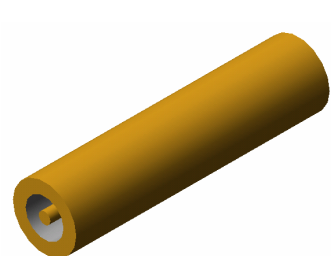
(b) Microstrip



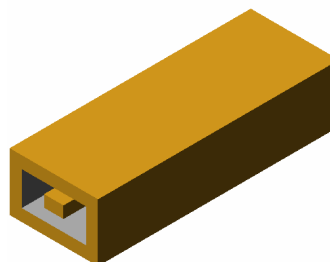
(c) Conductor – backed co-planar waveguide



(d) Rectangular waveguide



(e) Coaxial line



(f) Rectangular coaxial line

Figure 3.1: Guiding structures

Physically, a stripline is a flat strip of metal in between two parallel ground plates, separated by dielectric as shown in Figure 3.1 (a). The wave propagates in the TEM mode. The interior strip can be incorporated into useful functional circuits. The ground plates can be extended wide enough to shield the interior circuitry from outside interference.

Microstrip can be envisioned as one half of the stripline with a conductor plate parallel to and above the flat conducting ground plane with an insulator in between, as shown in Figure 3.1 (b). The characteristic impedance of the line is determined by the width of the line, the thickness, and the dielectric constant of the insulating layer. The wave propagates in a quasi-TEM mode.

Coplanar waveguides are advantageous when assembling passive and active circuits, together since all conductors, are on a common plane as shown in Figure 3.1 (c). Another type of transmission line is the waveguide as shown in Figure 3.1 (d). The waves in waveguides propagate in TE or TM mode. Waveguides have the advantage of having only one hollow conductor that confines the travelling waves. Thus, besides having low loss propagation, it can be easier to construct at higher frequencies compared to coaxial lines Figure 3.1(e). The wave propagates down the coaxial line in the TEM mode.

The behaviour of a transmission line is largely described by the characteristics of impedance, Z_0 velocity, v , attenuation constant, α , and peak power handling capability, P_{\max} , in terms of the physical parameters and the dielectric and conducting materials used. [2].

The characteristic impedance can be described as the ratio of the voltage across the line to the current along the line at any cross section when a wave is propagating in one direction only [3]. In a lossless line, the impedance can be simplified as [3, 4],

$$Z_0 = \sqrt{\frac{L}{C}}, \quad (3.1)$$

where L is the total self inductance of two conductors and C is the shunt capacitance due to the close proximity of the two conductors. Note from equation (3.1) that the characteristic impedance is independent of the position along the line.

The waves propagate along the lines at a certain velocity, known as the phase velocity. It is given by [4],

$$v_p = \frac{\omega}{\beta}, \quad (3.2)$$

where ω is the angular frequency and β is the phase constant.

If we consider a signal launched along a waveguide in arbitrary time dependence and with the phase velocity of each wave component the same, the signal will retain the same wave shape as it travels. However, if the phase velocity of the component waves varies, they will gradually change in phase. The components may then combine and produce a different wave shape compared to the original launched signal. This occurrence is known as dispersion [3].

In transmission lines, the phase velocity is given as:

$$v_p = \frac{1}{\sqrt{\epsilon\mu}}, \quad (3.3)$$

where ϵ is the medium permittivity and μ is the medium permeability.

If these two parameters are varied as a function of frequency, then the line will exhibit material dispersion.

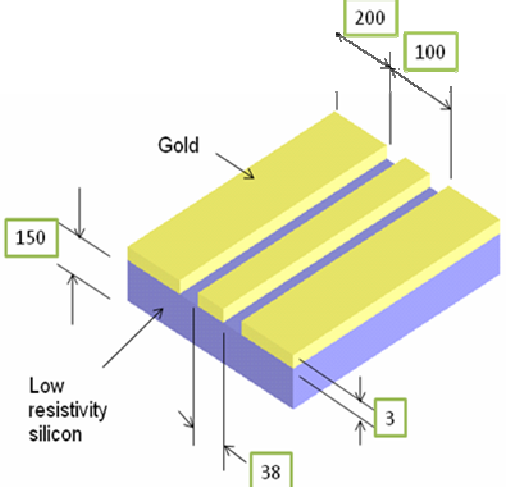
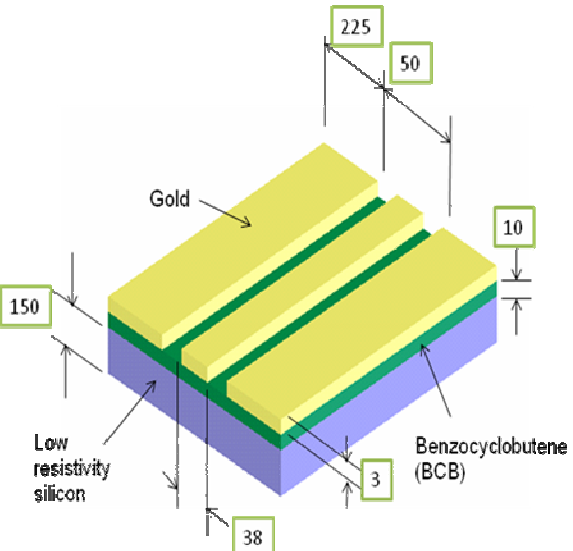
In this study, the coaxial line and the waveguide involved are air filled. Therefore, it is assumed no material dispersion takes place.

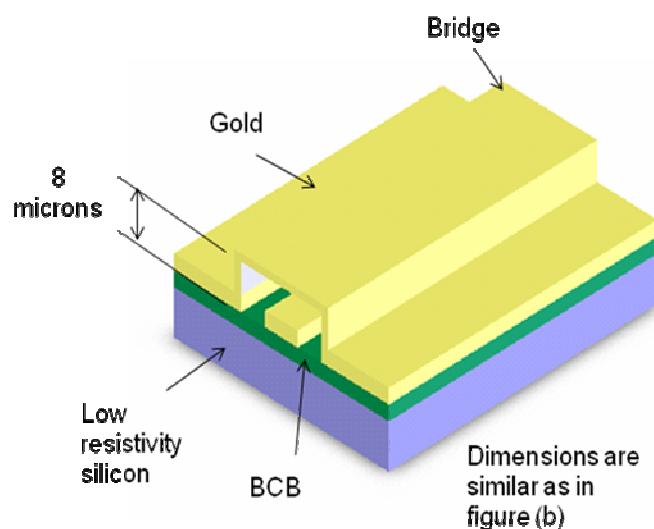
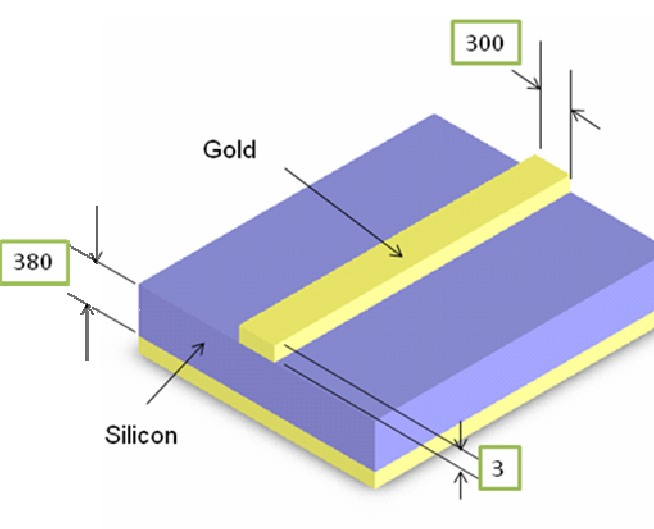
3.1.2 Micromachined Transmission Lines

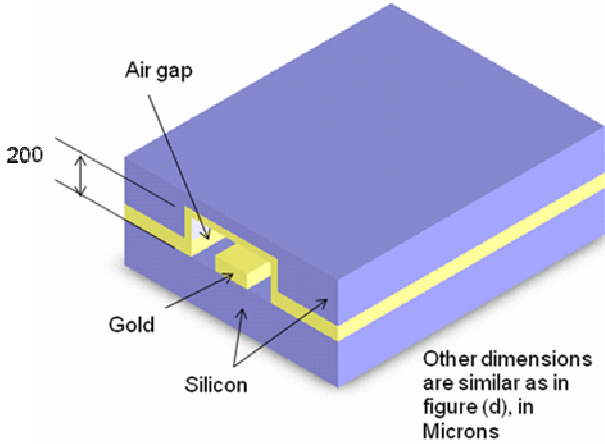
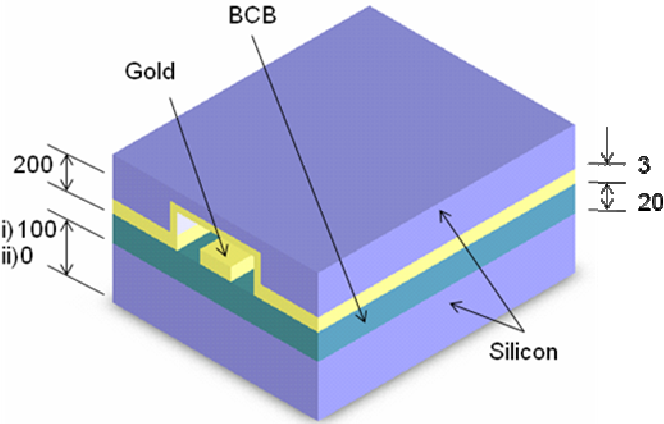
Different types of transmission lines were investigated in the past few years in order to achieve low loss transmission at millimetre wavelength frequencies. Table 3.1 shows losses observed for different transmission lines.

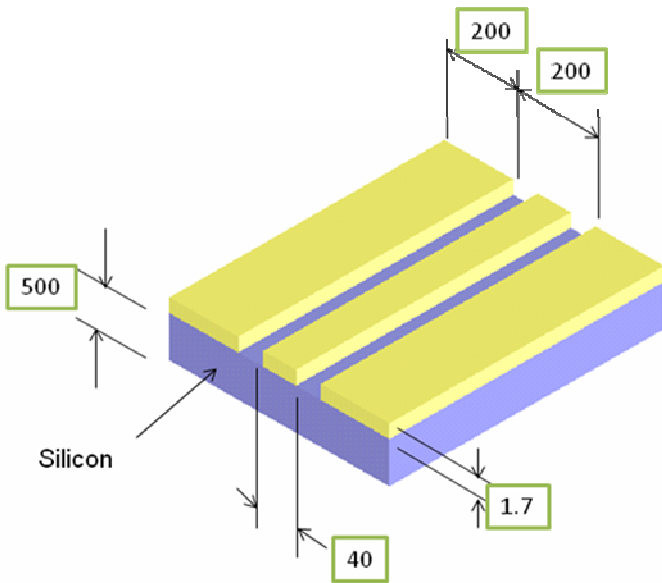
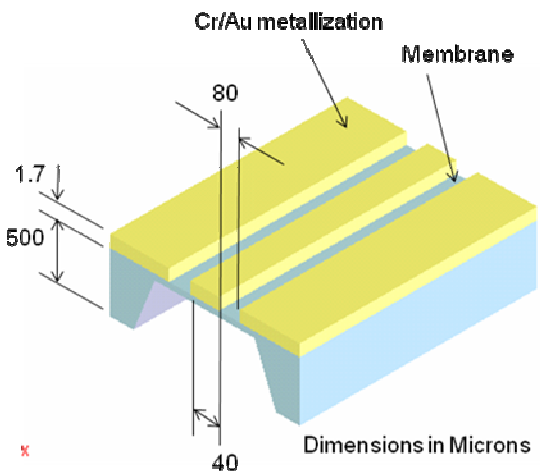
One of the main issues in manufacturing devices at millimetre wavelength is the significant transmission line losses on low resistivity substrates [5]. A co-planar waveguide (CPW) structure in Table 3.1 (a) was manufactured on a low resistivity silicon substrate ($\rho = 10 \Omega \text{ cm}$). A 3.4 dB/mm loss was observed at 50 GHz. The loss reduced to a 0.6 dB/mm by introducing a benzocyclobutene (BCB) layer between the silicon substrate and the line, as shown in Table 3.1 (b). A ground-ground bridge structure shown in Table 3.1 (c) covered the CPW line, thus reducing the loss further to a 0.55 dB/mm.

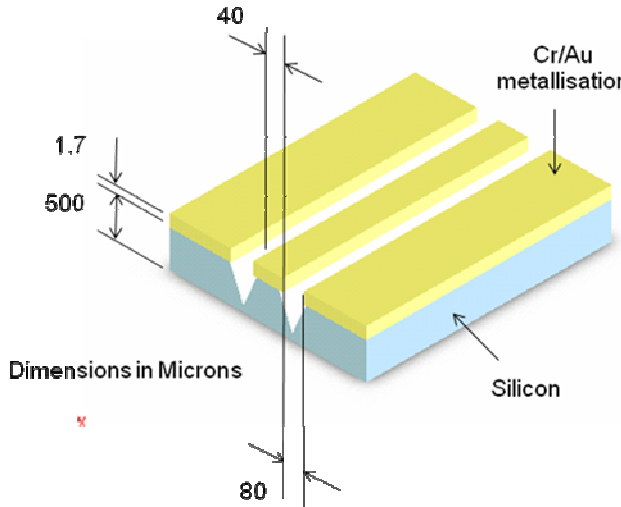
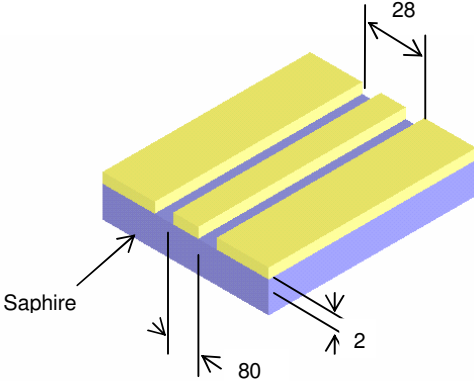
Table 3.1 Micromachined Transmission Lines.

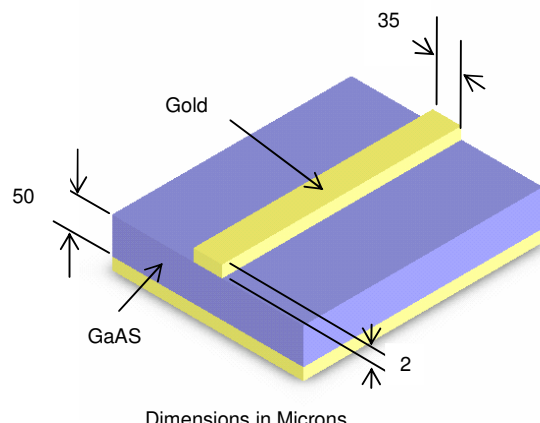
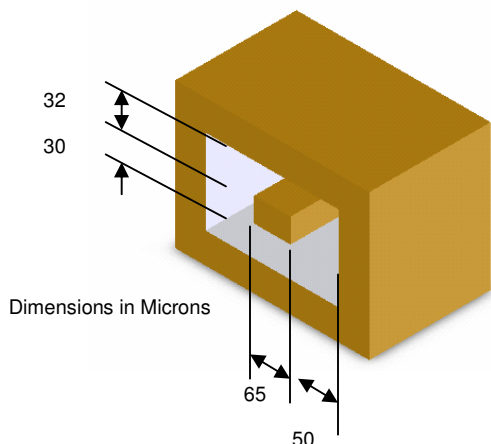
Structure	Loss	Reference
 <p style="text-align: center;">(a)</p>	<p>3.4 dB/mm at 50 GHz</p>	<p>[5]</p>
 <p style="text-align: center;">(b)</p>	<p>0.6 dB/mm at 50 GHz</p>	<p>[5]</p>

 <p style="text-align: center;">(c)</p>	<p>0.55 dB/mm at 50 GHz</p>	<p>[5]</p>
 <p style="text-align: center;">(d)</p>	<p>0.15 dB/mm at 40 GHz</p>	<p>[6]</p>

 <p>(e)</p>	<p>0.12 dB/mm at 40 GHz</p>	<p>[6]</p>
 <p>(f)</p>	<p>i) 0.06 dB/mm at 40 GHz</p> <p>ii) 0.033 dB/mm at 40 GHz</p>	<p>[6]</p>

 <p style="text-align: center;">(h)</p>	<p>0.162 dB/mm at 60 GHz</p>	<p>[7]</p>
 <p style="text-align: center;">(i)</p>	<p>0.069 dB/mm at 60 GHz</p>	<p>[7]</p>

 <p style="text-align: center;">(j)</p>	<p>0.115 dB/mm at 60 GHz</p>	<p>[7]</p>
 <p style="text-align: center;">(k)</p>	<p>0.17 dB/mm at 60 GHz</p>	<p>[8]</p>

 <p>(l)</p>	<p>0.12 dB/mm at 60 GHz</p>	<p>[8]</p>
 <p>(m)</p>	<p>0.06 dB/mm at 60 GHz</p> <p>0.05 dB at 40 GHz</p>	<p>[8]</p>

The loss in microstrip line is compared to the inverted microstrip line (IMSL) in [6]. The microstrip line in Table 3.1 (d) has a loss 0.15 dB/mm, which is 0.03 dB higher than IMSL structure shown in Table 3.1 (e). The IMSL is modified by introducing a BCB membrane layer shown in Table 3.1 (f). The IMSL with BCB membrane on 100 μm silicon has

improved the loss by half compared to IMSL without BCB membrane. The structure with suspended BCB without the silicon shows a loss 0.03 dB/mm.

The field in co-planar lines is tightly concentrated in the apertures between the conductors. The idea of using silicon micromachining to remove the dielectric material in the area between the conductors was implemented in [7]. The removal of the material reduces the line inductance and leads to less current flowing in the conductors [7]. Two types of micromachined co-planar lines were compared to a conventional co-planar line shown in Table 3.1 (h). The conventional line shows a 0.162 dB/mm loss at 60 GHz. A suspended co-planar line using membrane technology shown in Table 3.1 (i) was 0.046 dB lower than 0.115 dB/mm loss given by the second micromachined co-planar structure shown in Table 3.1 (j).

Micromachining allows construction of three dimensional (3D) structures such as a coaxial line. A rectangular coaxial line (Table 3.1 (m)) has been compared to a co-planar line (Table 3.1 (k)) and microstrip line (Table 3.1 (l)) in [8]. The rectangular coaxial line loss, 0.06 dB/mm at 60 GHz is the lowest, compared to 0.12 dB/mm given by the microstrip line and 0.17 dB/mm given by the co-planar line. Thus, a rectangular coaxial line is a good candidate for millimetre wave circuits as it offers low loss transmission. A transition from the rectangular coaxial line to planar and non-planar lines is worth investigating in order to facilitate possible demand in circuit integration.

3.1.3 Transmission Lines Losses

All transmission lines have losses due to finite conductivity and/or lossy dielectrics. This section will discuss the attenuation due to conductor loss. The dielectric loss is neglected, as all transmission lines used in this study are air filled. A loss comparison between round coaxial, square coaxial, microstrip and strip line at the frequency of 50 GHz has been presented in [9]. In [9], *Mathcad 8* software has been used to compute the attenuation, considering all the transmission lines to be air filled with ideal copper metallization and having a 50 Ω characteristic impedance. The round coaxial line exhibits the lowest attenuation with respect to the cross sectional area, as shown in Figure 3.2. The square coaxial followed closely behind the round coaxial line.

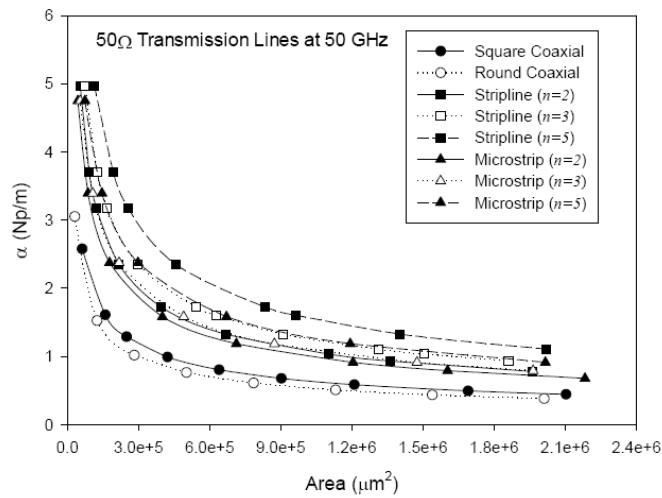


Figure 3.2: Attenuation constant versus area, taken from [9]

Therefore, a coaxial line is chosen in this study as a low loss transmission line that would produce good system performance. However, due to the nature of constructing a layering micromachined structure with the same thickness for each layer, it is not easy to build either a round or square coaxial line. It is only possible to change the dimensions in one plane to obtain the desired characteristic impedance, which form a rectangular coaxial line.

3.2 Micromachined Rectangular Coaxial Lines

A coaxial cable is made of an outer conductor covering an inner conductor with an insulator in between. The wave propagates down the line in TEM mode. The coaxial line has the advantage over a stripline or microstrip in that the inner conductor is totally covered by the outer conductor. Therefore, the fields are completely enclosed between the two conductors. This profile makes it possible to construct two lines very close to each other without coupling between contiguous lines. The signals coupling from adjacent lines are significant in high frequency microwave system design, where the physical structure size and spaces could be very small. The rectangular coaxial line gives the advantages of ease of signal routing and high isolation in passive millimetre wave circuit structures [8].

In this project, a rectangular coaxial line is chosen to be made in five layers using a micromachining technique. The dielectric insulator is eliminated, leaving an air filled space between the inner conductor and the outer conductor. The elimination allows lower loss and the removal of any substrate modes that can be a problem at high frequencies. The centre conductor is held up by short circuit stubs.

A cross section of a rectangular coaxial line built using five layer metallisation is depicted in Figure 3.3. The rectangular inner conductor can be located symmetrically or asymmetrically inside a rectangular hollow outer conductor [10]. For simplicity in design and manufacturing, a symmetrical structure is chosen in this study.

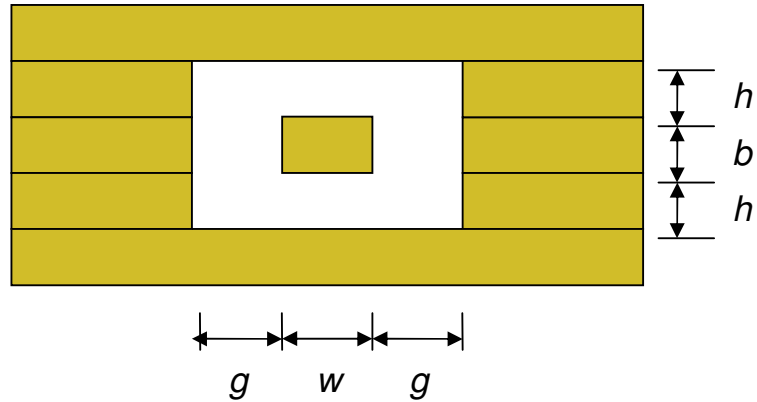


Figure 3.3: Cross section of the rectangular coaxial line.

The characteristic impedance of a rectangular coaxial line can be approximately calculated using equations given by Chen [11];

$$Z_0 = \frac{376.62}{2\left(\frac{b}{g} + \frac{w}{h}\right) + 4\left(\frac{C_1}{\epsilon} + \frac{C_2}{\epsilon}\right)}, \quad (3.4)$$

where b , g , w and h are from the structure in Figure 8 (a) and C_1 and C_2 are given by

$$C_1 = \frac{\varepsilon}{\pi} \left[\ln \left(\frac{g^2 + h^2}{4h^2} \right) + 2 \left(\frac{h}{g} \right) a \tan \left(\frac{g}{h} \right) \right] \quad , \quad (3.5)$$

$$C_2 = \frac{\varepsilon}{\pi} \left[\ln \left(\frac{g^2 + h^2}{4g^2} \right) + 2 \left(\frac{g}{h} \right) a \tan \left(\frac{h}{g} \right) \right] \quad . \quad (3.6)$$

Chen's equations have been reviewed by Weil and it is noted that Chen's work is based on the coupled stripline equation developed by Cohn [8, 12, 13]. The equations are approximated by the conditions of $w > g$ and $b > h$ [8]. Reid did the comparison between the calculations using Chen's equation and finite element simulations performed using Ansoft's HFSS. It was found that the calculated value was within 4% of the simulation in all cases, which gives confidence in using the equations. Since it was not a rigorous analysis, another comparison has been done here between the calculations using (3.4) to (3.6) and numerical simulations. Simulations were performed using CST microwave software to confirm the validity and approximate accuracy of the equations to be used in this study. The rectangular coaxial line has been designed using equations (3.4) to (3.6) and simulated using CST simulator software. The width of the inner conductor, w , is varied with a constant g . The other side's dimensions, b and h are maintained at 300 μm layer thickness. A graph has been plotted as shown in Figure 3.4. The difference between the theoretical calculation and numerical simulation curves is 3% at $w = 1000 \mu\text{m}$ and 4% at $w = 200 \mu\text{m}$. This is due to stripline approximations in Chen's equations [8] which are only valid for approximate conditions of $w > g$ and $b > h$, as mentioned earlier. However, from the comparisons made, the percentages of differences are tolerated. Therefore, Chen's equations are used in this study.

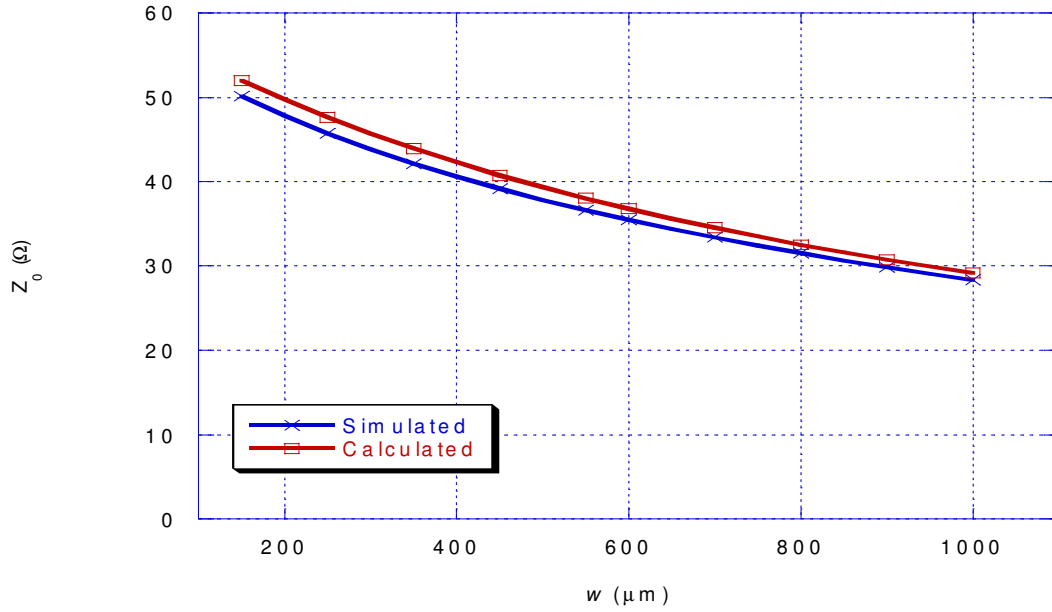


Figure 3.4: Calculated and simulated characteristic impedance.

As mentioned in Chapter 1, the dielectric loss of this rectangular coaxial line is avoided by having air filled between the two conductors. The conductor loss of a rectangular coaxial line can be calculated by [8]

$$\alpha_c = \frac{\Delta Z_0}{\sigma \mu_c v_p \delta^2 Z_0}, \quad (3.7)$$

where Z_0 is the characteristic impedance calculated from (3.4), δ is the skin depth from (2.1), v_p is the phase velocity of the line given by (3.3), μ_c is the permeability, σ is the

conductivity of the metal, and ΔZ_0 is the change in the impedance when the conductor walls are receded by half of the skin depth of the conductor.

The rectangular coaxial line is mainly studied here in order to build a Butler matrix, which will be discussed in Chapter 5. Referring to Figure 3.3, Table 3.2 shows the dimensions of the rectangular coaxial line obtained using (3.4) to (3.6). The two impedances shown are the most useful values used in designing the Butler matrix. The dimensions of h and b are fixed at 200 μm layer thickness.

Table 3.2 Rectangular Coaxial Line Dimensions.

Z_0	h (μm)	b (μm)	g (μm)	w (μm)
50 Ω	200	200	135	222
35 Ω	200	200	135	530

The Butler matrix designed with this rectangular coaxial line will be integrated with an antenna array at the end. A waveguide is needed to feed the horn and the waveguide slot antennas, while a rectangular coaxial line to a co-planar waveguide transition is needed for on-wafer measurement purposes. The waveguide, the co-planar waveguide and the transitions to the coaxial line will be discussed in the next sections.

3.3 Co-planar Waveguide (CPW)

The co-planar waveguide (CPW) nature of a single-sided configuration makes it ideal for surface mounted component integration. It is studied in this work for measurement purposes as mentioned earlier. The measurement is detailed in Appendix A. The configuration of the CPW is shown in Figure 3.5. The ground planes on each side of the centre conductor should extend greater than $5B$. Otherwise, a coplanar strip analysis should be applied [14]. The distance between the two grounds, B , should be less than half wavelength to prevent propagation of higher modes [14].

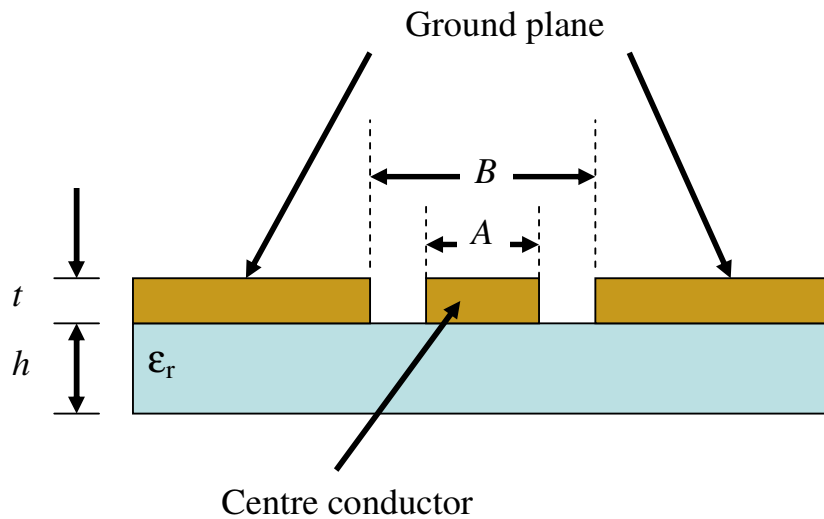


Figure 3.5: Co-planar waveguide (CPW) configuration.

The impedance of the CPW is given by [14]

$$Z_0 = \frac{30\pi K(k_t')}{\sqrt{\epsilon_{eff,t}} K(k_t')} , \quad (3.8)$$

where

$$\epsilon_{eff,t} = \epsilon_{eff} - \frac{\epsilon_{eff} - 1}{\frac{(B-A)}{2} \left(\frac{K(k)}{K(k')} \right) + 1} , \quad (3.9)$$

$$\epsilon_{eff} = 1 + \frac{\epsilon_r - 1}{2} \left(\frac{K(k')K(k_1)}{K(k)K(k_1')} \right) , \quad (3.10)$$

$$k_t = \frac{A_t}{B_t} , \quad (3.11)$$

$$k_t' = \sqrt{1 - k_t^2} , \quad (3.12)$$

$$k = \frac{A}{B} , \quad (3.13)$$

$$k' = \sqrt{1 - k^2} , \quad (3.14)$$

$$k_1 = \frac{\sinh\left(\frac{\pi A_t}{4h}\right)}{\sinh\left(\frac{\pi B_t}{4h}\right)} , \quad (3.15)$$

$$k_1' = \sqrt{1 - k_1^2} , \quad (3.16)$$

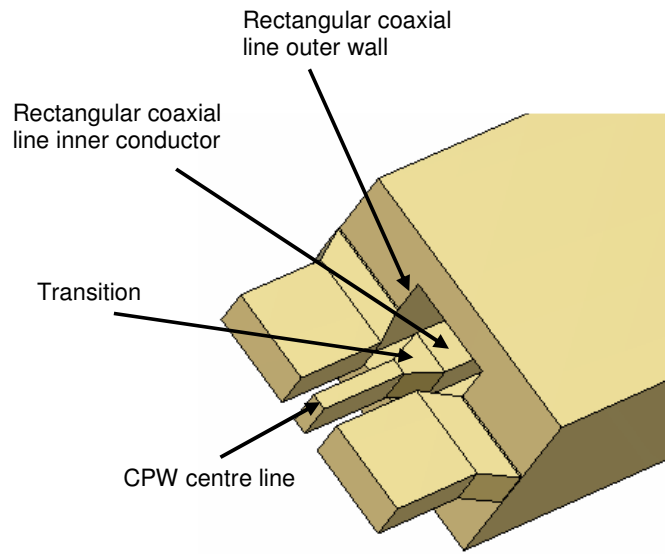
$$A_t = A + \frac{1.25t}{\pi} \left[1 + \ln \left(\frac{4\pi A}{t} \right) \right], \quad (3.17)$$

$$B_t = B - \frac{1.25t}{\pi} \left[1 + \ln \left(\frac{4\pi A}{t} \right) \right]. \quad (3.18)$$

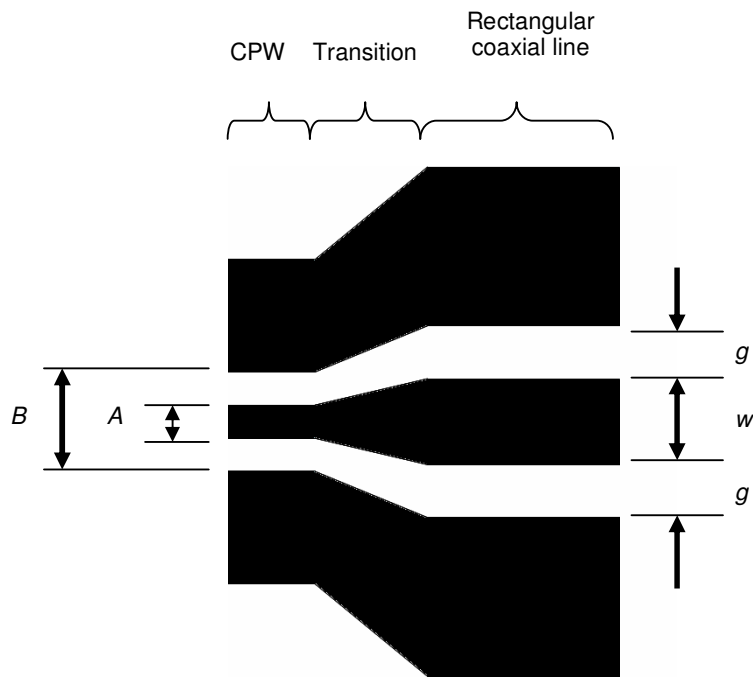
$K(k)$ is a complete elliptical integral of the first kind.

3.4 CPW to Rectangular Coaxial line Transition

In this work, a 50Ω air-suspended CPW is made as the transition from the rectangular coaxial line described in the previous section. The structure and its cross section are depicted in Figure 3.6. The line is smoothly tapered and optimized using CST software [15]. The CPW dimensions are $A = 80 \mu\text{m}$ and $B = 270 \mu\text{m}$. These dimensions fit the pitch size of the 76 GHz ground-signal-ground-ground-signal-ground (GSG GSG) Picoprobe® used for measurement. The coaxial line cross section dimensions are $g = 135 \mu\text{m}$, and $w = 220 \mu\text{m}$.



(a)



(b)

Figure 3.6: (a) CPW to rectangular coaxial line transition and (b) the cross section.

3.5 Rectangular Waveguide

A waveguide is known as a low loss transmission line with all the electric and magnetic fields confined within the guide wall. Thus, no radiation loss is expected. In this study, dielectric losses are also negligible as the waveguide is air filled. However, a small power loss is expected from the wall conductor. Figure 3.7 shows the dominant mode E-field and H-field of a conventional rectangular waveguide with the width, a , and height, b , cross section.

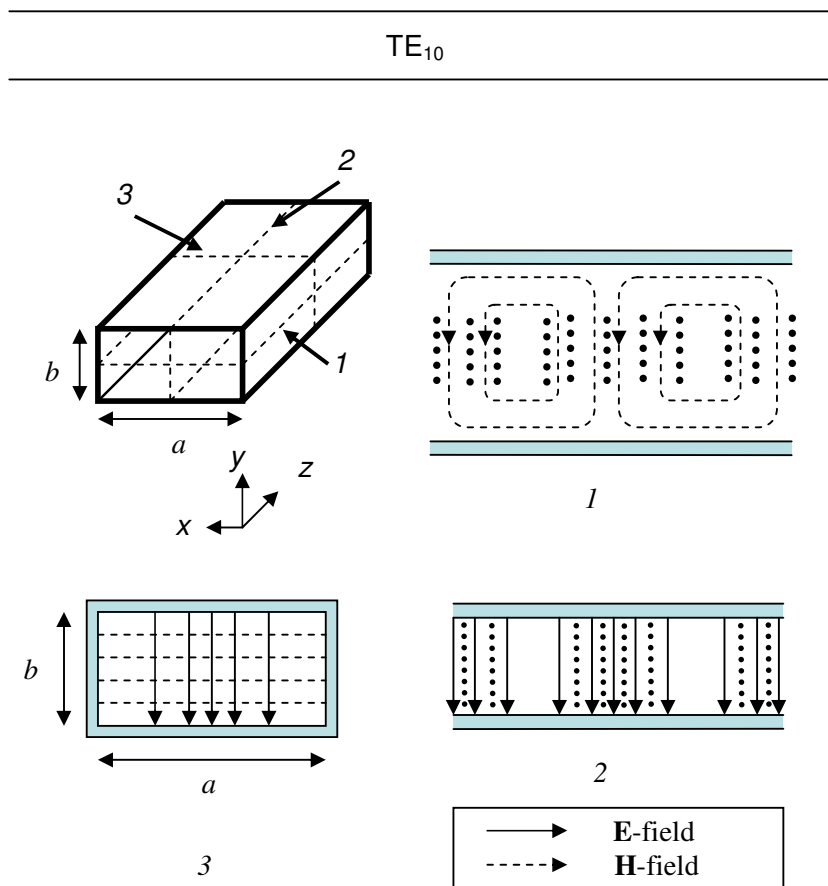


Figure 3.7: Dominant mode field lines of rectangular waveguide [4].

Waveguides possess a high pass filter characteristic. Propagation is considered above the cut-off frequency, f_c . The cut-off frequency of a rectangular waveguide can be calculated by

$$f_{c_{mn}} = \frac{1}{2\pi\sqrt{\mu\epsilon}} \sqrt{\left(\frac{m\pi}{a}\right)^2 + \left(\frac{n\pi}{b}\right)^2} \quad , \quad (3.19)$$

where a and b are the waveguide cross section dimensions, and m and n are the integers that label the modes. The integer m refers to the number of half wavelength variations of field across the width, a , while integer n refers to the number of half wavelength variations of field across the height, b . For instance, the dominant mode TE_{10} gives $m=1$ and $n=0$. This indicates one half wavelength variations of the field across a of the waveguide; as shown in Figure 3.8; and no field variations across b .

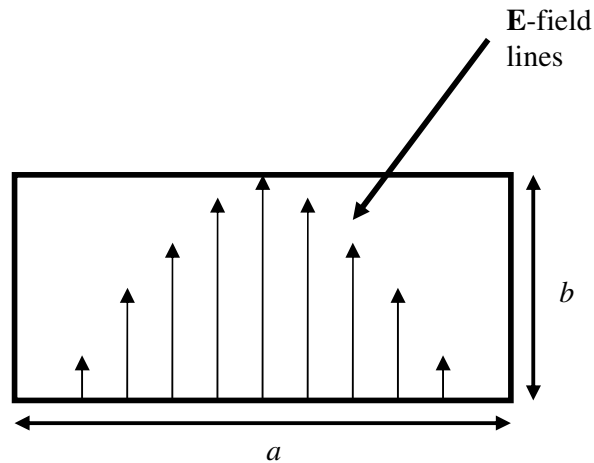


Figure 3.8: TE_{10} field variations across a rectangular waveguide aperture.

Any modes with cut-off frequency, f_c , higher than the operating frequency, f_0 , will decay exponentially away from the source of excitation [4]. This study takes the single TE dominant mode of propagation into consideration. The choice of using the dominant mode is made to ensure only one mode propagates through the waveguide, thus simplifying the analysis.

The common way to excite a signal into a waveguide is using a coaxial line as shown in Figure 3.9. However, the protrusion of a coaxial line into the waveguide from the wall is not easy to implement in the five layer micromachining manufacturing technique as proposed in this research. Therefore, a ridge waveguide is proposed to accommodate the transition from a coaxial line in the Butler matrix before the signal radiates, for instance through the flared horn. This is illustrated in Figure 3.10 and presented in the next sections.

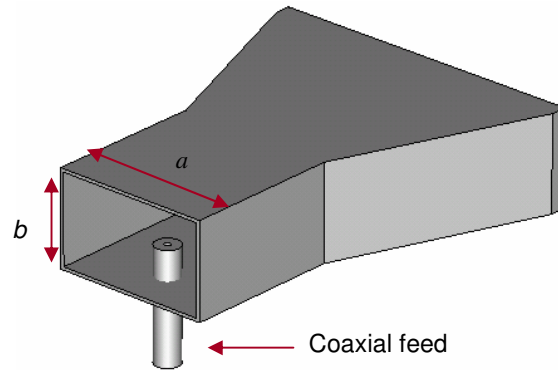


Figure 3.9: Coaxial feed waveguide

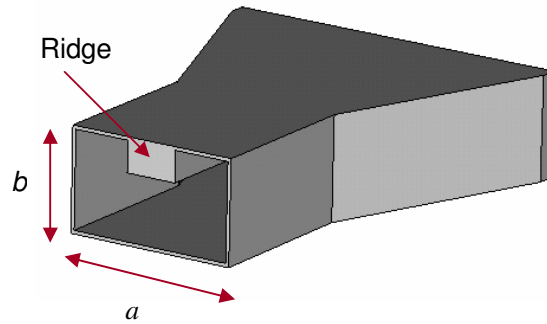


Figure 3.10: Ridge waveguide feeding a horn antenna.

3.5.1 Rectangular Ridge Waveguide

Attention to ridge waveguides increased after Cohn published his work in obtaining eigenvalues by using the transverse resonance in 1947 [16]. The idea of lowering the dominant mode cut-off frequency expands the single-mode range before the higher order modes occur. This is the main advantage of ridge waveguides over the conventional ones. Hopfer improved Cohn's design curves with proper consideration of step discontinuity susceptance in all calculations, particularly at an aspect ratio of 0.45 [17]. Aspect ratio is the ratio of the two waveguide aperture side walls. A decade later, Pyle repeated Hopfer's work and improved the analysis with more accurate data for any aspect ratio [18]. An approximate dominant mode field determination was first published by Getsinger [19]. Work and analysis on ridge waveguides was continued by other researchers in exploring and utilising the advantages of lowering the cutoff frequency and expanding the bandwidth [20-

24]. Hence, the ridge is applied in this research to accommodate the transition from the coaxial line in the Butler matrix to feed the horn and the waveguide slot antennas, which will be discussed further in Chapter 4 and Chapter 5. At the same time the ridge applied reduces the size of the waveguide as it lowers the dominant cut-off frequency.

The single and double ridge waveguide cross section diagrams are shown in Figure 3.11. The ridge at the centre of the waveguide cross section can be envisioned as a reduced height of the waveguide. It can be seen as a heavy capacitive load placed across the maximum electric field of the dominant TE_{10} mode, shown in Figure 3.8. Thus, the cut-off frequency is considerably lowered.

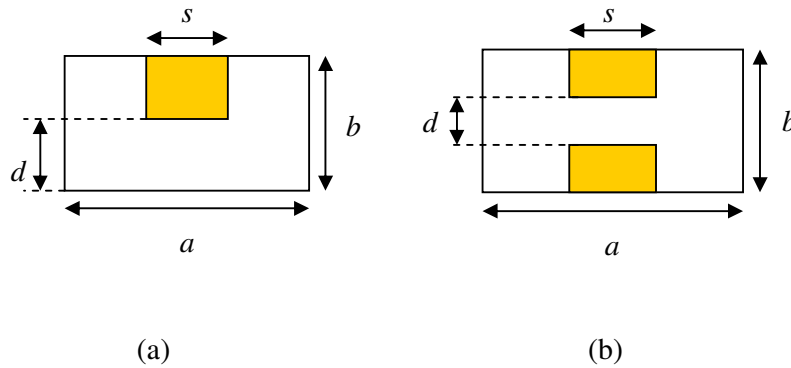


Figure 3.11: Cross sections diagram; (a) single ridge waveguide and; (b) double ridge waveguide.

The dominant mode cut-off wavelength of a single ridge waveguide can be calculated by using a closed form approximation [25];

$$\frac{a}{\lambda_{c10}} = \frac{a}{2(a-s)} \left[1 + \frac{4}{\pi} \left(1 + 0.2 \sqrt{\frac{2b}{b-s}} \right) \left(\frac{2b}{a-s} \right) \ln \left[\operatorname{cosec} \left(\frac{\pi d}{2b} \right) + \left(2.45 + 0.2 \frac{s}{a} \right) \left(\frac{2bs}{2d(a-s)} \right) \right] \right]^{\frac{1}{2}} \quad (3.20)$$

The dimensions, a , b , and s are shown in Figure 3.11. Equation (3.26) has been adopted to estimate an appropriate ridge waveguide structure size. The calculated single ridge waveguide dimensions are as follows.

Table 3.3 Ridge Waveguide Dimensions.

	Dimension in μm
A	2000
B	600
D	200
S	1060

3.6 Micromachined Coaxial Line to Ridged Waveguide

Transition

A coaxial line to ridged waveguide transition is designed to ensure that signals from the coaxial line Butler matrix can be transferred to the horn and the waveguide slot antennas. In most literature, a coaxial cable is protruded into the ridge as a launcher that sends the signal into the waveguide [26-29]. A fashionable compact transition has been reported in [30] with the coaxial line on the axis of the wave propagation and steps in the ridges. It has been successfully tested from 6 GHz to 18 GHz with low return loss. However, these conventional ways of exciting the waveguide are not fit for the proposed five layer micromachined structure. Furthermore, the inner conductor of the coaxial line at 63 GHz will be very small and fragile to protrude or connect directly onto the ridge. Therefore, it is wise to have the interconnections properly attached to each other.

Boyd [31] has patented a parallel plate line transition section between a coaxial line and a double ridge waveguide as shown in Figure 3.12. He utilised a modified strip line as a transition. One end of the strip line is connected to the inner conductor of the coaxial line while the other end is connected to the upper ridge. The upper side of the transition section is approximately quarter wavelength and terminated by a conductive block which is the upper ridge. Therefore, the other end of the transition section appears as an open circuit. Only the lower part of transition line conducts energy into the waveguide. The transition allows a transformation of the TEM mode in coaxial line into the TE mode in the ridge waveguide. This concept has been adopted in designing the transition section in this project, but using a single ridge rather than double ridge.

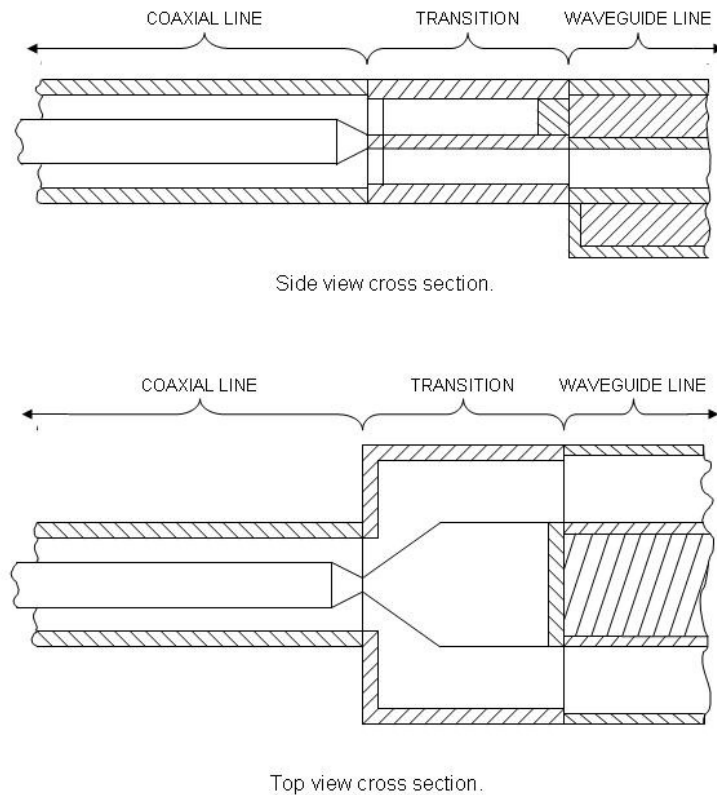


Figure 3.12: Coaxial line to double ridge waveguide transition presented in [31].

The designed structure in this work is divided into three sections, which are the coaxial line, the transition and the ridge waveguide. Figure 3.13 shows the transition structure drawn in five layers with the top layer lifted. The cross-sections at A, B and C show the rectangular coaxial line, the transition with tapered inner conductor, and the ridge waveguide, respectively. The inner conductor of the coaxial line is extended into the transition section and combined as a ridge in the waveguide. The inner transition line is made tapered to avoid the possibility of electrical breakdown with the outer conductor of the coaxial line. The transition section is designed quarter wavelength at 63 GHz and shorted to the outer wall as it is combined with the ridge. Thus, the other end is virtually an open circuit with very high impedance.

The transition has been designed and simulated using CST simulation software. The coaxial line is designed with a characteristic impedance of $50\ \Omega$ using Chen's equations, while the ridge waveguide is designed as presented in Table 3.3, section 3.5.1. The length of the tapered coaxial line inner conductor has been optimised in CST [15]. The S-parameter plot in Figure 3.14 shows a good match with the return loss, S_{11} , better than -20dB from 60 GHz to 90 GHz.

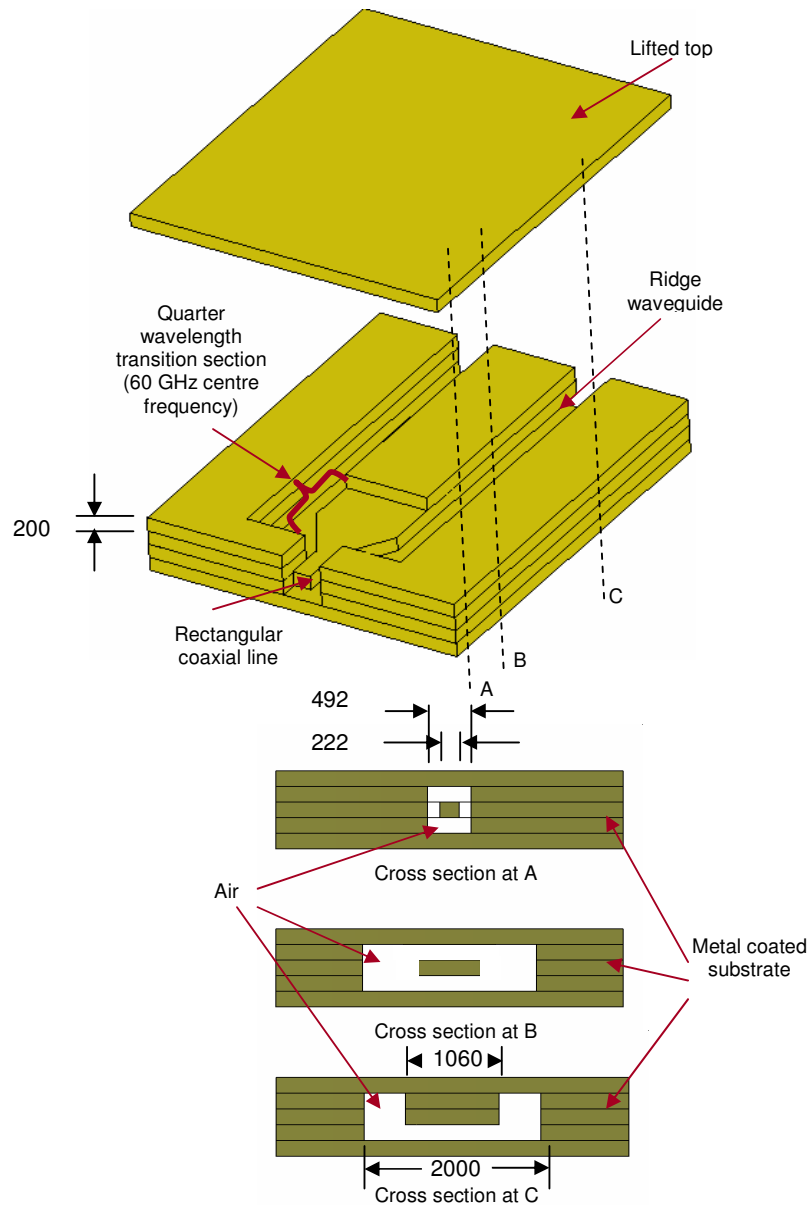


Figure 3.13: Rectangular coaxial line to ridge waveguide transition and the cross sections.

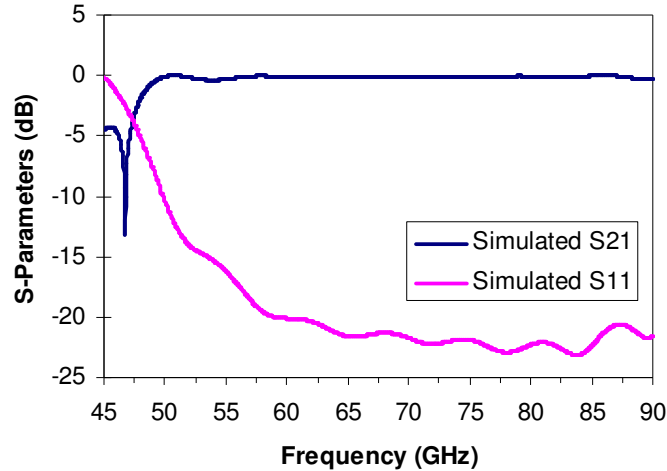


Figure 3.14: Simulated response of the rectangular coaxial line to ridge waveguide transition.

As shown in Figure 3.13, the inner conductor of the coaxial line and the ridges in the middle of the waveguide are suspended in the air. Thus, a proper design with a support system has to be made. There are a few ways of supporting suspended micromachined lines, such as using membrane technology and quarter wavelength stubs [8, 10, 32, 33].

Membrane technology presented in Chapter 2 is widely used in supporting microstrip lines. However, the thin dielectric membrane used can influence the phase velocity and cause some degradation in device performance [34]. Furthermore, it is an expensive technology. The membrane is used with a hole beneath a planar line in order to achieve an effective relative dielectric constant near to unity. Thus, the performance of the device can be improved. Nevertheless, the dielectric free transmission line used in this study absolutely gives a unity relative dielectric constant.

The ridge waveguide stub supporting structure is chosen as the transmission media in this research is air filled. The shorted stubs can be designed by using a wideband band-pass filter design as detailed in [35-37]. The impedance of stubs has to match the main line. However, in this work the waveguide property of not allowing propagation below the cut-off frequency is utilised in designing the support system. The suspended ridge line is connected to the outer wall by shorted stubs lines which have a cut off frequency higher than the operation frequency of the main ridge waveguide. In this case, the stubs are designed at 110 GHz cut off frequency, giving $a = 750 \mu\text{m}$, $b = 600 \mu\text{m}$, $s = 300 \mu\text{m}$ and $d = 200 \mu\text{m}$. The ridges of the stubs hold the suspended ridge of the main line waveguide. Ideally the stubs will be invisible to the signal at the designed frequency.

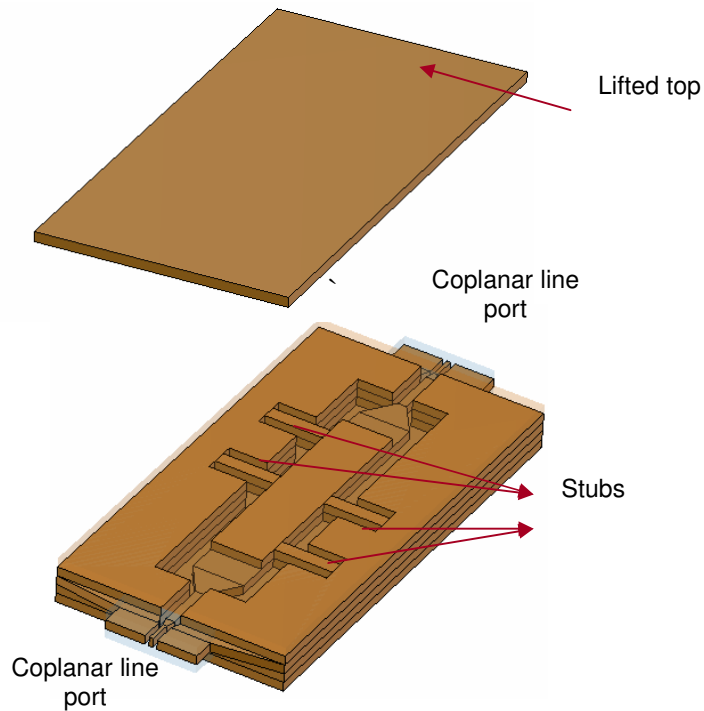


Figure 3.15: Back to back coaxial line to ridge waveguide transition circuit.

For measurement purposes, two transition circuits have been made back to back. In addition, each of the coaxial ports has been transitioned to a co-planar line, so that a probe station can be used. An optimisation to match the co-planar line to the rectangular coaxial line has been done using CST simulation software. The arrangements, together with the stubs, are shown in Figure 3.15. Figure 3.16 depicts the five layer expanded view of the structure. The size of the whole structure is 10.7 mm x 5.0 mm x 1.0 mm.

The structure is assembled by bonding five layers of gold coated SU-8 photoresist shown in Figure 3.16, each 200 μm thick. The manufacturing process is detailed in Chapter 2. The metal coated pieces of layer 3 and 4 before bonding to form a device structure are depicted in Figure 3.17.

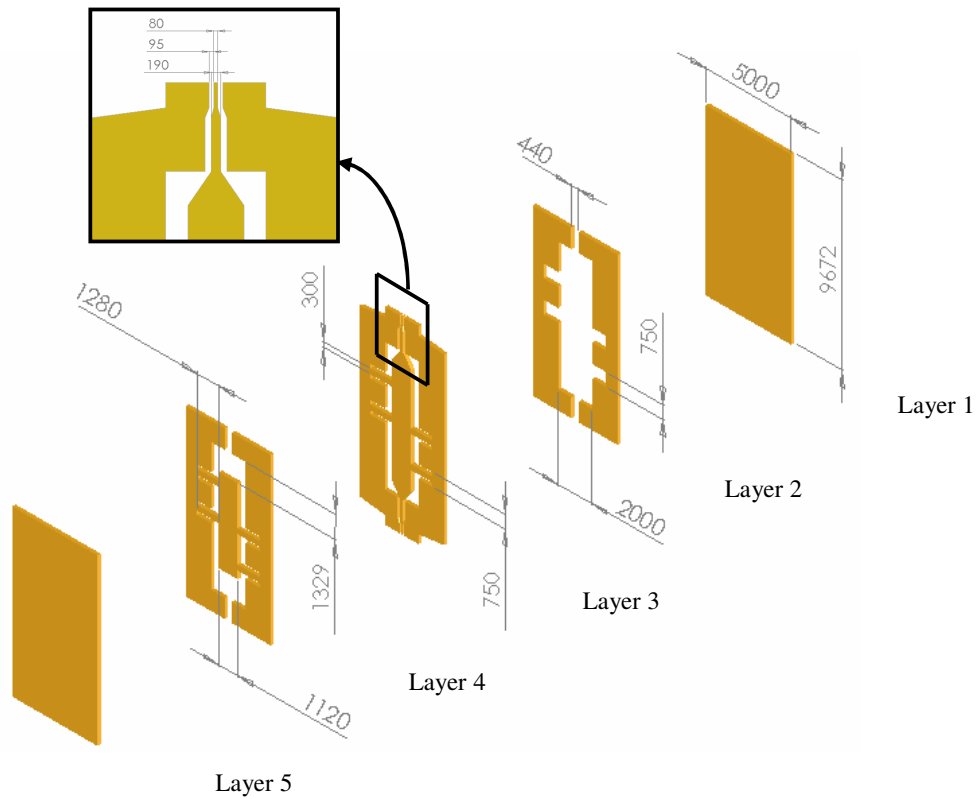


Figure 3.16: Five layers exploded view with all dimensions in μm

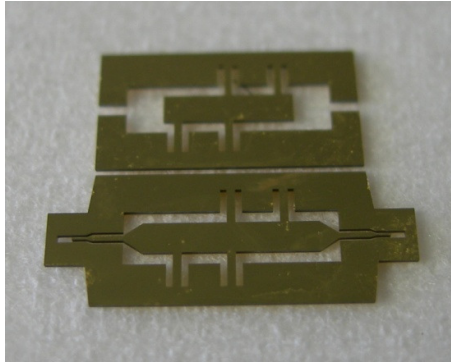


Figure 3.17: Metal coated pieces of layer 3 and 4.

The constructed structure has been measured using a wafer probe station connected to a vector network analyzer. A line-reflect-reflect-match (LRRM) full two port calibration has been done before the measurement. The same measurement setup has been implemented in [10]. The setup is detailed in Appendix A.

Figure 3.18 shows a comparison of simulated and measured response. The measured return loss is better than 12 dB from 60 GHz to 90 GHz with insertion loss about 1 dB. The return loss result shows that the transition is well matched within the frequency range. However, some misalignment of the layers during the process of assembling the structure may cause deviation in measurement results, particularly shown in the insertion loss plot. Overall, the measurement result agrees well with the simulation.

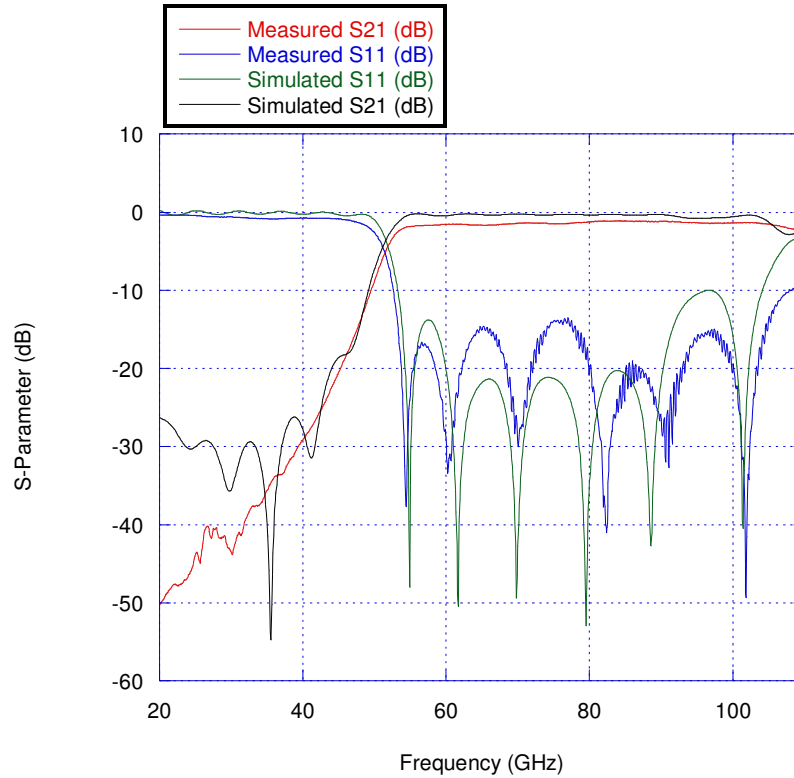


Figure 3.18: Simulated and measured response of the transition.

In order to see the effect of the stubs in the structure, the circuit has been simulated again with a different stub length, L , and separation, S , as shown in Figure 3.19 and Figure 3.20, respectively. The length is stepped at $125\ \mu\text{m}$ from $1500\ \mu\text{m}$ to $2000\ \mu\text{m}$, while S is fixed at $1840\ \mu\text{m}$. The separation is stepped at $250\ \mu\text{m}$ from $1000\ \mu\text{m}$ to $2000\ \mu\text{m}$ with L fixed at $1840\ \mu\text{m}$. The response shows very slight differences with the changes, but the differences are quite obvious at lower frequency when the separation is changed. This is due to the junction effect when the ridge of the stubs is connected to the ridge of the main waveguide. It can be seen as an asymmetrical thick slit in the main waveguide. The changes in length are less influential as the stubs are designed at higher order mode cut-off frequency. However, the responses still follow the same pattern.

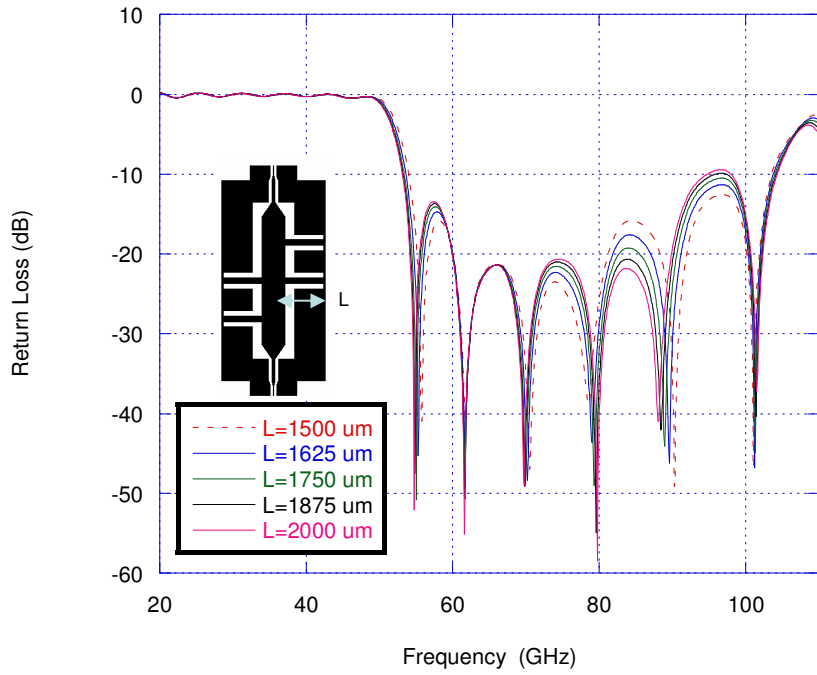


Figure 3.19: Simulated responses for different stub length with $S = 1840 \mu\text{m}$.

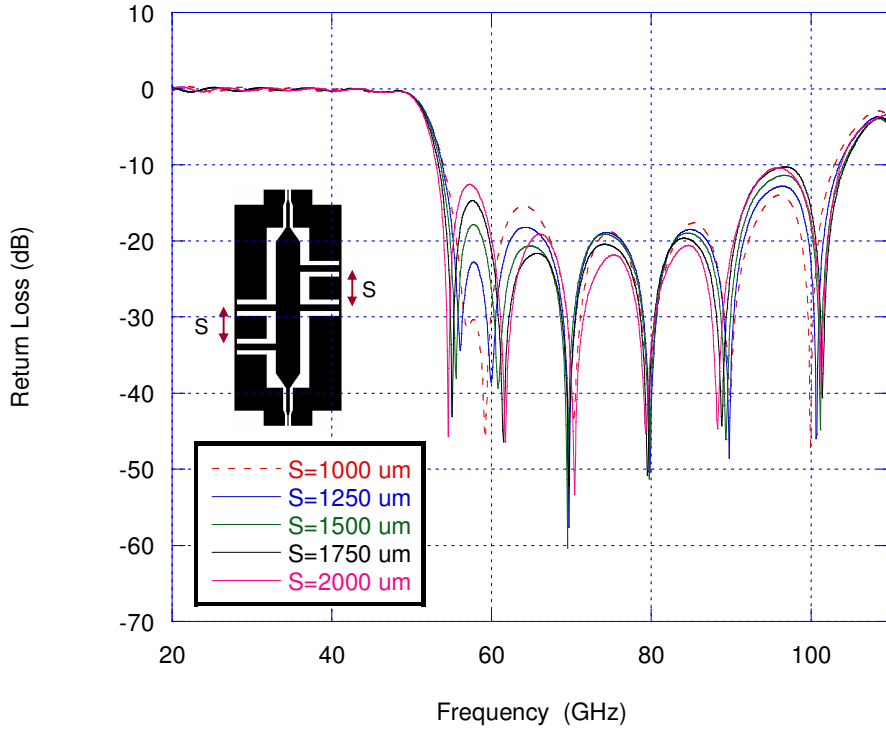


Figure 3.20: Simulated responses for different stub spacing with $L = 1840 \mu\text{m}$.

3.7 Summary

A successful design of a micromachined rectangular coaxial line to ridge waveguide transition has been presented here. This design has been published in [38]. The transition will be used later in feeding the horn antenna and the slot waveguide antenna in Chapter 4. The responses of the stubs with different lengths and spacing are depicted in Figure 3.19 and Figure 3.20, showing the advantage of using a higher order mode ridge waveguide in the flexibility of placing the supporting shorted stub in circuits. The CPW to rectangular coaxial line transition is designed to be applied on each structure for measurement purposes. The rectangular coaxial line discussed in this chapter will be implemented again in designing the Butler matrix in Chapter 5.

References

- [1] L. P. B. Katehi, G. M. Rebeiz, T. M. Weller, R. F. Drayton, H. J. Cheng, and J. F. Whitaker, "Micromachined circuits for millimeter- and sub-millimeter-wave applications," in *IEEE Antennas and Propagation Magazine*. vol. 35, 1993, pp. 9-17.
- [2] K. Chang, *Handbook of Microwave and Optical Components* vol. 1: John Wiley & Sons, 1989.
- [3] N. J. Cronin, *Microwave and Optical Waveguides*. Bristol: J. W. Arrowsmith Ltd., 1995.
- [4] D. M. Pozar, *Microwave Engineering*, Third ed.: John Wiley & Sons, 2005.
- [5] H. Henri, S. Gonzague, V. Matthieu, C. Alain, and D. Gilles, "Ultra low loss transmission lines on low resistivity silicon substrate," in *IEEE MTT-S International Microwave Symposium Digest*, 2000, pp. 1809-1812
- [6] K. Takahashi, U. Sangawa, S. Fujita, M. Matsuo, T. Urabe, H. Ogura, and H. Yabuki, "Packaging using microelectromechanical technologies and planar components," *IEEE Transactions on Microwave Theory and Techniques*, vol. 49, pp. 2099-2104, 2001.
- [7] K. J. Herrick, T. A. Schwarz, and L. P. B. Katehi, "Si-micromachined coplanar waveguides for use in high-frequency circuits," *IEEE Transactions on Microwave Theory and Techniques*, vol. 46, pp. 762-768, 1998.

- [8] J. R. Reid, E. D. Marsh, and R. T. Webster, "Micromachined Rectangular-Coaxial Transmission Lines," *IEEE Transactions on Microwave Theory and Techniques*, vol. 54, pp. 3433-3444, 2006.
- [9] I. Llamas-Garro, "Micromachined Microwave Filters," in *School of Engineering*. vol. PhD Birmingham: The University of Birmingham, 2003.
- [10] M. J. Lancaster, Jiafeng Zhou, Maolong Ke, Yi Wang, Kyle Jiang, "Design and High Performance of Micromachined K-Band Rectangular Coaxial Cable," *IEEE Transactions on Microwave Theory and Techniques*, vol. 55, pp. 1548-1553, 2007.
- [11] T. S. Chen, "Determination of The Capacitance, Inductance, and Characteristic Impedance of Rectangular Lines," *IEEE Transactions On Microwave Theory And Techniques*, vol. 8, 1960.
- [12] C. M. Weil, "The Characteristic Impedance of Rectangular Transmission Lines with Thin Centre Conductor and Air Dielectric," *IEEE Transactions on Microwave Theory and Techniques*, vol. 26, pp. 238-242, 1978.
- [13] S. B. Cohn, "Thickness Correction for Capacitive Obstacles and Strip Conductors " *IRE Transaction on Microwave Theory and Techniques*, vol. 8, pp. 638-644, 1960.
- [14] B. C. Wadell, *Transmission Line Design Handbook*: Artech House, Inc., 1991.
- [15] *CST Microwave Studio*: CST GmbH, Darmstadt, Germany., 2006.
- [16] S. B. Cohn, "Properties of Ridge Waveguide," *Proceedings of IRE*, vol. 35, August 1947.
- [17] S. Hopper, "The Design of Ridged Waveguide," *IRE Transactions on Microwave Theory and Techniques*, vol. 3, pp. 20-29, 1955.
- [18] J. R. Pyle, "The Cutoff Wavelength of the TE_{10} Mode in Ridged Rectangular Waveguide of Any Aspect Ratio," *IEEE Transactions on Microwave Theory and Techniques*, vol. 14, pp. 175-183, 1966.
- [19] W. J. Getsinger, "Ridge Waveguide Field Description and Application to Directional Couplers," *IRE Transaction on Microwave and Techniques*, vol. 10, pp. 41-50, 1962.
- [20] J. P. Montgomery, "On the Complete Eigenvalue Solution of Ridged Waveguide," *IEEE Transactions on Microwave Theory and Techniques*, vol. 19, pp. 547-555, 1971.
- [21] J. R. H. Wolfgang, Miles N. Burton, "Closed-Form Expressions for the Parameters of Finned and Ridged Waveguides," *IEEE Transactions on Microwave Theory and Techniques*, vol. 30, pp. 2190-2194, 1982.
- [22] Y. Utsumi, "Variational analysis of ridge waveguide modes," *IEEE Transactions on Microwave Theory and Techniques*, vol. 33, pp. 111-120, 1985.
- [23] W. Sun, C. A. Balanis, "MFIE Analysis and Design of Ridged Waveguides," *IEEE Transactions on Microwave Theory and Techniques*, vol. 41, pp. 1965-1971, 1993.
- [24] J. Helszajn, *Microwave Planar Passive Circuits and Filters*: John Wiley & Sons, 1994.
- [25] J. Helzajn, *Ridge Waveguides and Passive Microwave Components*. London: Institute of Electrical Engineers, 2000.
- [26] C. Bruns, P. Leuchtman, R. Vahldieck, "Analysis and Simulation of 1-18 GHz Broadband Double Ridged Horn Antenna," *IEEE Transactions on Electromagnetic Compatibility*, vol. 45, pp. 55-60, 2003.
- [27] A. R. Mallahzadeh, A. A. Dastranj, H. R. Hassani, "A Novel Dual Polarized Double Ridged Horn Antenna for Wideband Applications," in *Progress In Electromagnetics Research B*. vol. 1, 2008, pp. 67-80.

- [28] Z. Shen, C. Feng, "A New Dual Polarized Broadband Horn Antenna," *IEEE Antennas and Wireless Propagation Letters*, vol. 4, pp. 270-273, 2005.
- [29] M. Botello-Perez, H. Jardon-Angular, I. G. Ruiz, "Design and Simulation of a 1 to 14 GHz Broadband Electromagnetic Compatibility DRGH Antenna," in *International Conference on Electrical and Electronics Engineering*, Mexico, 2005, pp. 118-121.
- [30] Y. Tikhov, In Sang Song, Jong Hwa Won, Jeong Phil Kim, "Compact Broadband Transition From Double Ridge Waveguide to Coaxial Line," *IET Electronic Letters*, vol. 39, pp. 530-532, 2003.
- [31] M. R. Boyd, "Parallel Plate Lie Transition Section Between a Coaxial Line and Ridged Waveguide," in *US Patent*, 1965.
- [32] I. Llamas-Garro, A. Corona-Chavez, "Micromachined Transmission Lines for Millimeter-wave Applications," in *16th IEEE International Conference on Electronics, Communications and Computers*, Mexico, 2006.
- [33] Y. Wang, Maolong Ke, M. J. Lancaster, F. Huang, "Micromachined Millimeter-Wave Rectangular-Coaxial Branch-ine Coupler with Enhanced Bandwidth," *IEEE Transactions of Microwave Theory and Techniques*, vol. 57, pp. 1655-1660, 2009.
- [34] S. V. Robertson, "A 10-60 GHz Micromachined Directional Coupler," *IEEE Transactions of Microwave Theory and Techniques*, vol. 46, pp. 1845-1849, 1998.
- [35] G. Mathaei, *Microwave Filters, Impedance Matching Networks, and Coupling Structures*: Artech House, 1985.
- [36] J.-S. Hong and M. J. Lancaster, *Microstrip Filters For RF/Microwave Applications*: John Wiley & Sons, 2001.
- [37] I. Llamas-Garro, M. J. Lancaster, P. S. Hall, "A Low loss Wideband Suspended Coaxial Line Components," *Microwave Optical Letter*, vol. 43, pp. 93-95, 2004.
- [38] N. A. Murad, M. J. Lancaster, Y. Wang, and M. Ke, "Micromachined Rectangular Coaxial Line to Ridge Waveguide Transition," in *10th Annual Wireless and Microwave Technology Conference Florida*, U. S., 2009, pp. 1-5.

Chapter 4

Micromachined Antennas

4.1 Introduction

An antenna is basically a transitional device between guiding structures and free space. Ideal conditions would allow all the generated energy to be radiated. In real applications, losses are present due to the material and the environment. Efforts to minimise the losses are significant especially at high frequencies to allow optimum performances.

At millimetre wavelengths, the fabrication tolerance levels are crucial as the size shrinks with the shorter wavelengths. Micromachining is an alternative to the conventional drilling and machining techniques in fabricating antennas. This chapter focuses on three types of micromachined antennas. They are the patch antenna, the horn antenna and the ridge waveguide slot antenna. These antennas are chosen as they are good candidates for applications at millimetre wave frequencies with low profile and sturdy structures to provide directive beams. The three antennas exhibit different beam of radiation pattern which allow

different physical configuration in real applications. For instance, the patch has a broadside radiation pattern which is different from the horn antenna. Furthermore, the use of SU-8 micromachining method is demonstrated for different antennas which introduce different constraint in construction, which need to be taken into account in the design.

This chapter presents on the literature and design of the three antennas. Measurement results are presented here, except for the patch antenna. Comparison between the antennas is presented in the conclusion at the end of the chapter.

4.2 Micromachined Patch Antenna

Patch antennas or microstrip antennas came to attention in 1970's after Howell and Munson developed the first practical microstrip antenna [1]. Their low profile characteristic makes them easily installed on any flat surface such as on aircraft, spacecraft and even satellites. Patch antennas can be designed with the radiating elements and the feed lines photo-etched on a dielectric material. The dielectric layer separates two parallel conductors with the ground layer at the bottom and the patch on the other side, as shown in Figure 4.1.

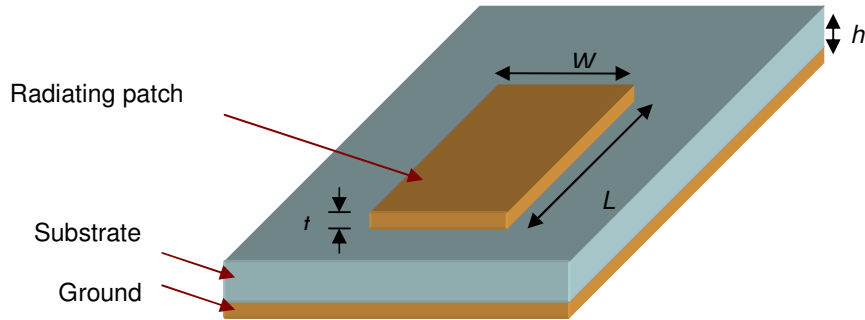


Figure 4.1: Microstrip patch antenna

The microstrip patch antenna is a very popular radiator in planar integration technologies [2]. The major issue of this antenna is the existence of the substrate higher order modes and the surface waves. The excitation of the substrate higher order modes can be avoided by operating the antenna below the first higher order mode cut-off frequency. The substrate mode cut-off frequency is given by [2]

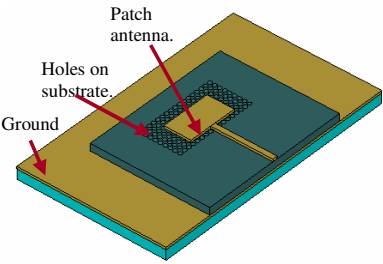
$$f_c = \frac{nc}{4d\sqrt{\epsilon_r - 1}}, \quad (4.1)$$

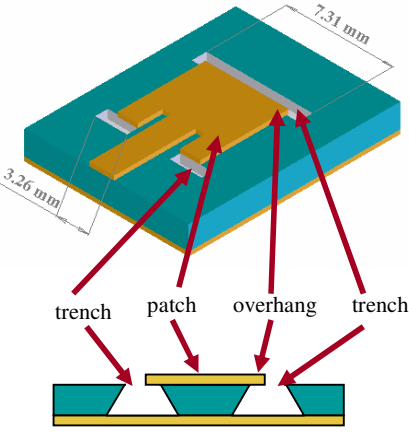
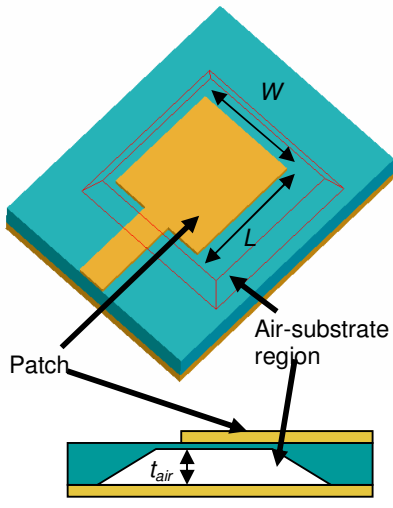
where n is the number of the mode which is 1 for the first higher order mode, c is the speed of light, d is the thickness of the substrate, and ϵ_r is the relative dielectric constant of the material used.

A surface wave can be referred to as a propagating mode guided by the air-dielectric surface for a dielectric substrate on a conductor ground plane, even without the upper conductor strip [3].

At high frequencies, a number of studies were initiated to improve the performance of patch antennas by suppressing the surface waves. A hole drilling approach is depicted in Table 4.1 (a) and was discussed in [4]. The efficiency of the antenna was improved by 22 %. Later, the holes are etched by micromachining instead of drilling. Trenches below the patch radiating edges shown in Table 4.1 (b) proposed in [5] enhanced the bandwidth by 0.5 % compared to the untrenched patch. A selective etching technique was implemented in [6] to remove the substrate underneath the antenna. The micromachined cavity lowers the effective dielectric permittivity and consequently suppresses the surface waves. The walls of the cavity were slanted as shown in Table 4.1 (c) due to the anisotropic etching technique used. The bandwidth improved by 64 % compared to the conventional patch antenna. The enhanced antenna also improved the efficiency by 28 %.

Table 4.1 The early micromachined patch antennas.

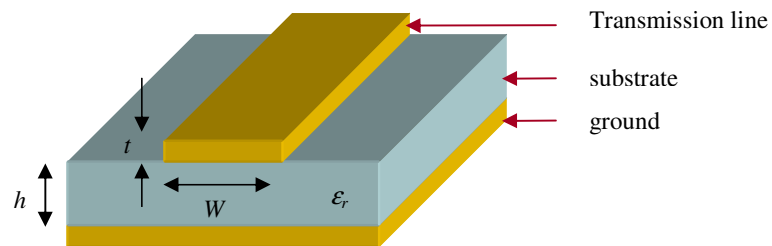
Structure	Frequency	Performance	Reference
 <p>(a)</p>	<p>12.8 – 13.0 GHz</p>	<p>A wide bandwidth of 4.6% was achieved. The efficiency was improved by 22% from 48 %</p>	<p>[4]</p>

	<p>10.0 – 14.0 GHz</p>	<p>The trenches increased the resonating frequency. Thus, larger size of patch can be implemented at a fixed frequency. A 5.2 % bandwidth was achieved, which was 0.5 % higher than the un-trenched one.</p>	<p>[5]</p>
 <p>(c)</p>	<p>20.0 GHz and 12.5-13.5 GHz scale model.</p>	<p>Increase in bandwidth and efficiency.</p>	<p>[6]</p>

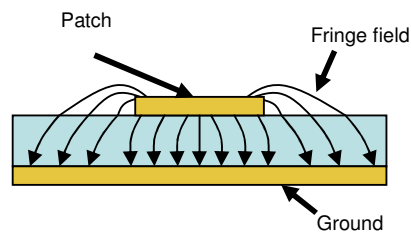
In this study, the antenna is made suspended in the air, totally disregarding the substrate related issue. The thick SU-8 photoresist micromachining technique discussed in Chapter 2 is used to build the structure. The design will be discussed further in the next section.

4.2.1 Patch Antenna Design

Rectangular patch antennas can be analysed using various modelling techniques. The transmission line model is well known in analysing a rectangular and square patch antenna. This type of model is used here as it is easy to illustrate the concepts. A microstrip line and its electric fields are shown in Figure 4.2.



(a) Microstrip line.



(b) Electric field lines.

Figure 4.2: Microstrip line and its electric field lines.

A microstrip patch antenna design procedure with a simplified formulation is given as follows [7, 8] :

1. Specify the dielectric constant, ϵ_r , the operating frequency, f_0 (in Hz), and the dielectric thickness, h .
2. Calculate the practical width; W , that leads to good radiation efficiencies.

$$W = \frac{1}{2f_0\sqrt{\mu_0\epsilon_0}} \sqrt{\frac{2}{\epsilon_r + 1}} \quad . \quad (4.2)$$

3. Determine the effective dielectric constant.

$$\epsilon_{eff} = \frac{\epsilon_r + 1}{2} + \frac{\epsilon_r - 1}{2} \left[1 + 12 \frac{h}{W} \right]^{\frac{1}{2}} \quad . \quad (4.3)$$

4. Determine the length extension, ΔL .

$$\Delta L = 0.412h \frac{(\epsilon_{eff} + 0.3) \left(\frac{W}{h} + 0.264 \right)}{(\epsilon_{eff} + 0.258) \left(\frac{W}{h} + 0.8 \right)} \quad . \quad (4.4)$$

5. Determine the actual length, L .

$$L = \frac{1}{2f_0\sqrt{\epsilon_{eff}}\sqrt{\mu_0\epsilon_0}} - 2\Delta L \quad . \quad (4.5)$$

Note that from the design steps above, the antenna element width, W , and length, L , basically depend on the wavelength, λ_0 , of the resonant frequency, f_0 . As it is proportional to the wavelength, the dimensions are reduced with the increasing of the resonant frequency.

The fields at the edges of the patch are ‘fringed’ as shown in Figure 4.2 (b). The fringing fields act as an additional length to the patch and influence the resonant frequency. Thus, the length of the patch has been extended at each end by a distance of ΔL , which can be calculated by using (4.4).

It can be seen from the field lines in Figure 4.2 (b) that some of the waves travel in the air and some in the substrate. Thus, the effective dielectric constant, ϵ_{eff} , is introduced to account for fringing and the wave propagation in the line [7]. However, in this study, no substrate is involved, leaving the patch suspended in the air. Therefore, the effective dielectric constant is unity.

The next step after finding the patch dimensions is to determine the feeding method. There are several ways to feed a patch antenna as shown in Figure 4.3.

A microstrip side feed (Figure 4.3 (a)) is an integration of another microstrip line with an impedance transformation connecting the patch to the input port. This kind of feed allows a simple integration on the same surface; however, it may introduce a coupling between the feed lines and the patch elements. To avoid the coupling on the same surface, an aperture or electromagnetic coupling (Figure 4.3 (c)) can be implemented by locating the microstrip feed line on different layers and coupling the power to the patch through an aperture. A coaxial line feed (Figure 4.3 (b)) is a very straightforward technique which places the coaxial line at the impedance matching point on the patch. However, it is not easy to implement at millimetre wavelengths.

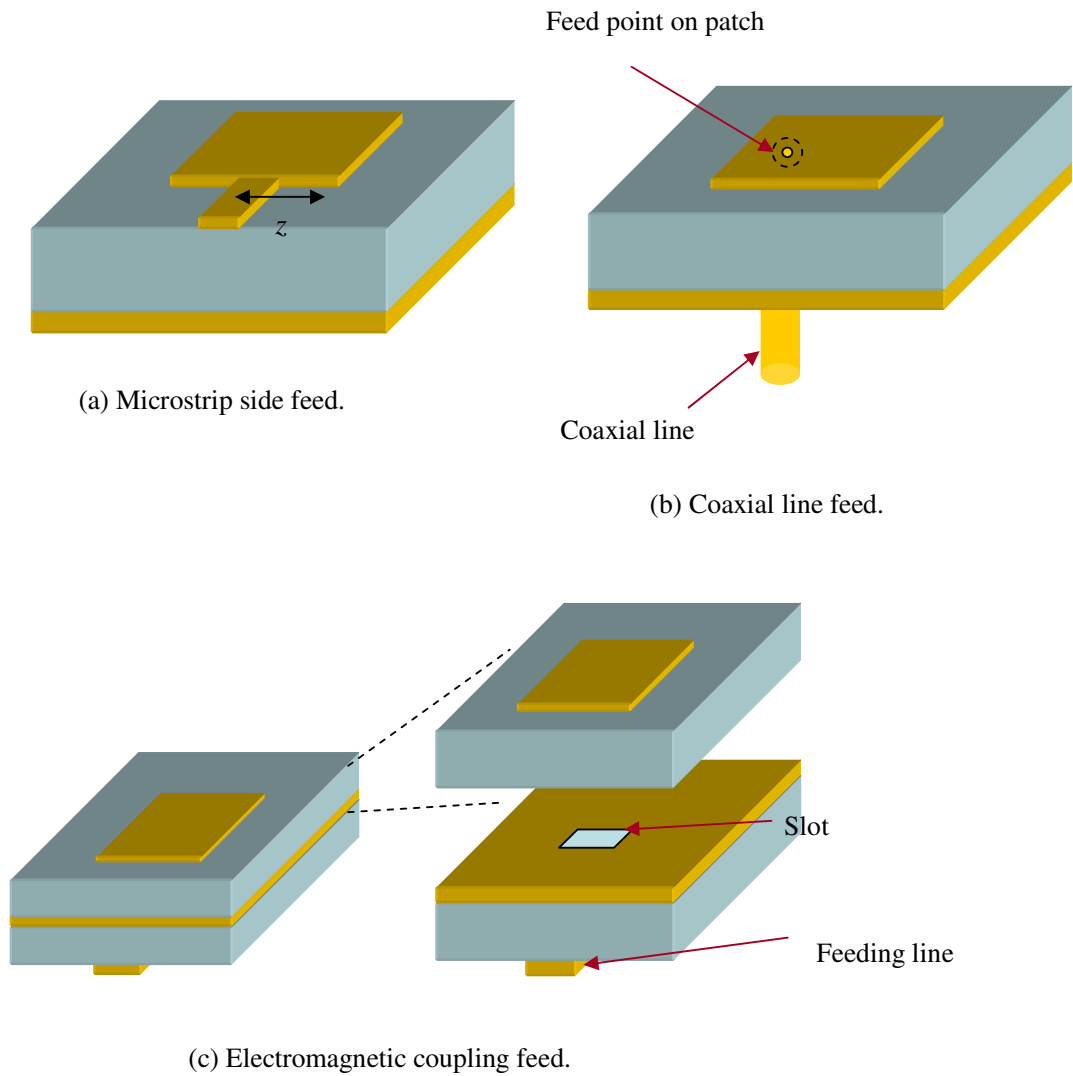


Figure 4.3: The patch antenna and most common feeding types.

For this project the side feed as shown in Figure 4.3 (a) is chosen. However, instead of the microstrip feed, a transition from a rectangular coaxial line onto the patch is applied. The feed is chosen here to have the line holding the suspended antenna and attached directly to the inner conductor of the coaxial line. For feeding purposes, the input admittance of a microstrip patch antenna can be calculated by [9]

$$Y_L = \frac{2G}{\left[\cos^2(\beta z) + \frac{G^2 + B^2}{Y_0^2} \sin^2(\beta z) - \frac{B}{Y_0} \sin(2\beta z) \right]}. \quad (4.6)$$

The distance from the edge, z , is shown in Figure 4.3 (a). In the figure, it is chosen to be at the centre of the edge to symmetrically feed the patch. Y_0 is the characteristic admittance of a microstrip line, while G is the radiation admittance and B is derived from the characteristic impedance. The variables are given by

$$G = \frac{1}{R_r}, \quad (4.7)$$

$$R_r = \frac{120\lambda_0}{1 - \frac{(k_0 h)^2}{24}}, \quad (4.8)$$

$$k_0 = \frac{2\pi}{\lambda_0}, \quad (4.9)$$

$$B = \frac{k_0 \Delta L \sqrt{\epsilon_{eff}}}{Z_0}, \quad (4.10)$$

$$Z_0 = \frac{377}{2\pi \sqrt{\epsilon_{eff}}} \ln \left(\frac{8h}{W} + 0.25 \frac{W}{h} \right). \quad (4.11)$$

Figure 4.4 shows the five layers air suspended patch antenna structure designed here using the above mentioned equations. The patch is designed at 63 GHz centre frequency. The dimensions are calculated using (4.2) to (4.5) giving the width and the length as 2.381 mm and 2.104 mm, respectively. The input impedance of the patch, $Z_L = 548 \Omega$ is determined by using (4.6) to (4.11). A quarter wavelength transformer is exploited to transform the impedance of the patch to the port impedance ($Z_{in} = 50 \Omega$). The characteristic impedance of the transformer is calculated using (3.15), giving a value of 166Ω . The width of the feed line is obtained by implementing the impedance into (4.11). All dimensions are optimized using CST software [10] to obtain the desired response at the designed frequency. The optimized dimensions are shown in Figure 4.4.

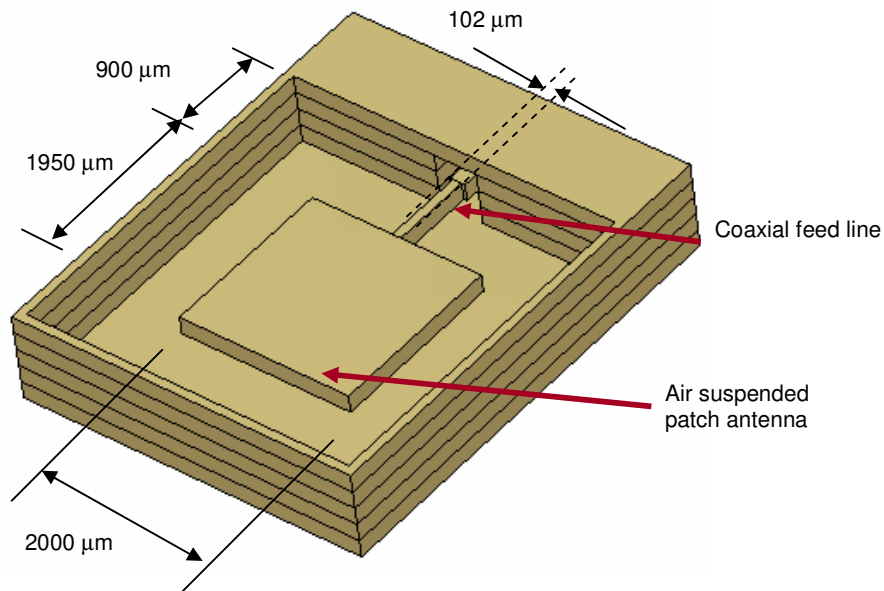


Figure 4.4: The single patch antenna fed by a rectangular coaxial line.

The performance of the antenna has been simulated using CST simulator software. The antenna resonates at the desired frequency of 63 GHz with return loss of -36.7 dB as shown in Figure 4.5. The -10 dB bandwidth is a very narrow 5.8 %. However, this is wider than the bulk micromachined membrane supported patch proposed in [11]. The bandwidth is calculated from the return loss plot by

$$BW = \frac{f_2 - f_1}{f_0} \times 100\% , \quad (4.7)$$

f_1 and f_2 are the lower and the upper frequencies at -10 dB in the return loss response.

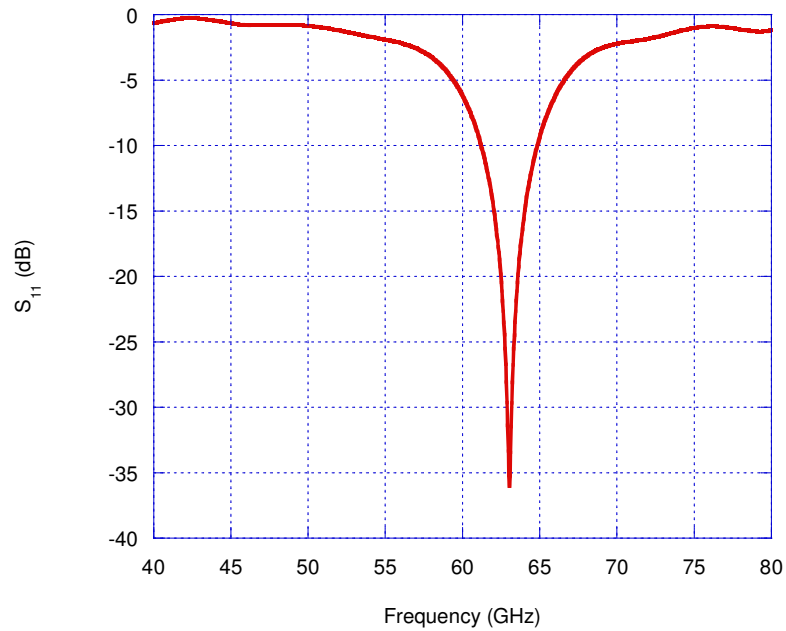
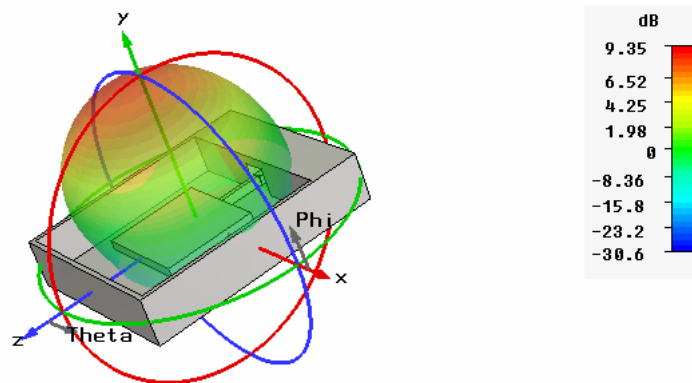
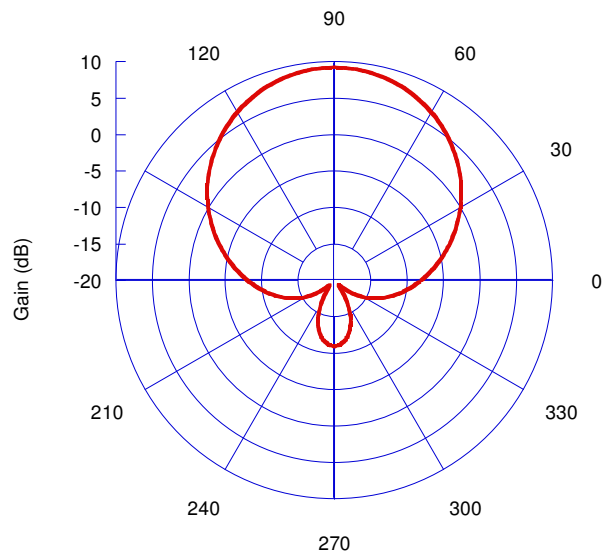


Figure 4.5: The simulated return loss of the single patch antenna.

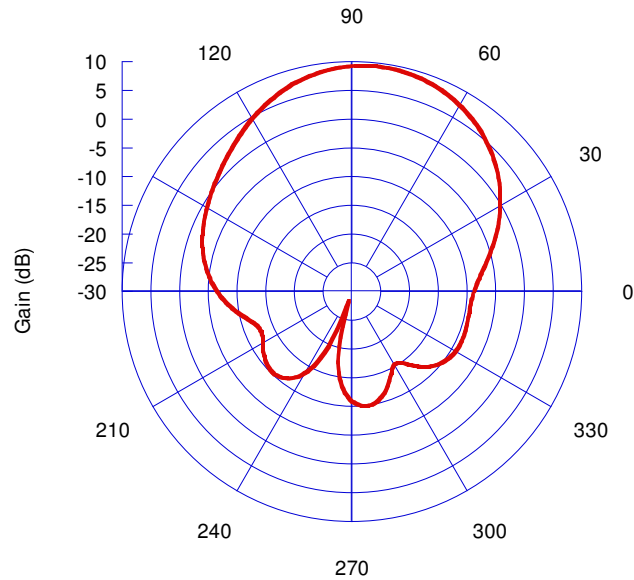
The radiation pattern of the designed single patch antenna is shown in Figure 4.6. The antenna radiates at 63 GHz with of 9.4 dB realized gain. An H-plane half power beamwidth (HPBW) of 65.3° and a very low side lobe level (SLL) of -20.1 dB are observed. The E-plane HPBW is 57.7° and the side lobe level (SLL) is -18.4 dB.



Radiation pattern 3D view



H-plane radiation pattern, ($\theta: 90^\circ$)



E-plane radiation pattern, ($\phi: 90^\circ$).

Figure 4.6: The simulated radiation pattern of the single patch antenna at 63 GHz.

Notice from Figure 4.4 that the feeding line width is $100\ \mu\text{m}$, which is very tiny and might be at risk when integrated further with other circuitry. Therefore, the antenna needs a better support system. A post supported patch was introduced in [12]. Two supporting posts were connected to the ground below the patch and one post connected to the CPW-feeding line. Another way of supporting an air suspended patch is using stubs as presented in [13]. The patch here is simply supported by supporting lines placed at the minimum voltage points as shown in Figure 4.7. This will minimise the effect of the added lines on the overall performance of the antenna. The same technique is used in [14], but manufactured with different technology at 6.3 GHz design frequency. The antenna is simulated again with the

support lines. The performance agrees well with the non-supported patch structure with low return loss at the designed frequency, as shown in Figure 4.8. The radiation pattern is shown in Figure 4.9.

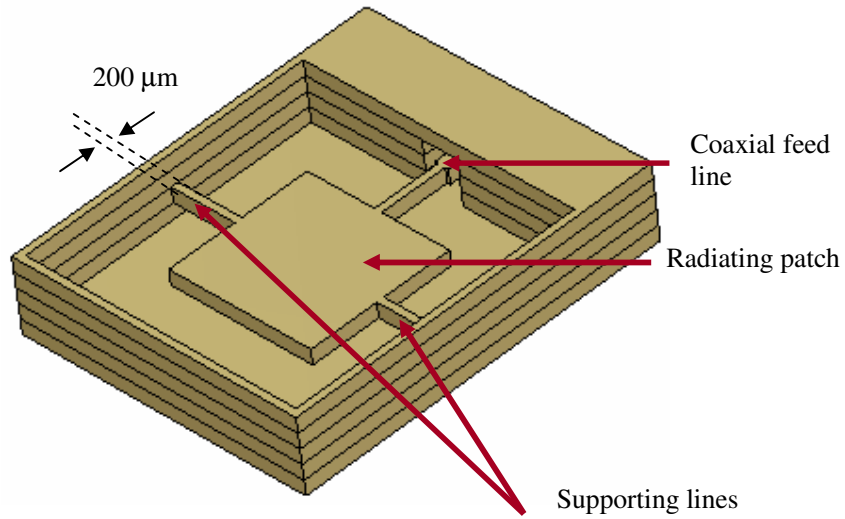


Figure 4.7: A patch antenna with two supporting lines.

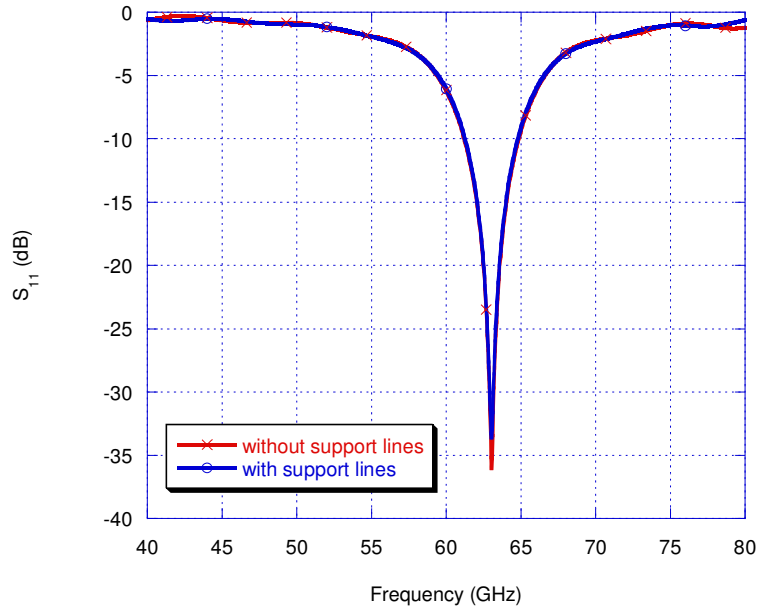
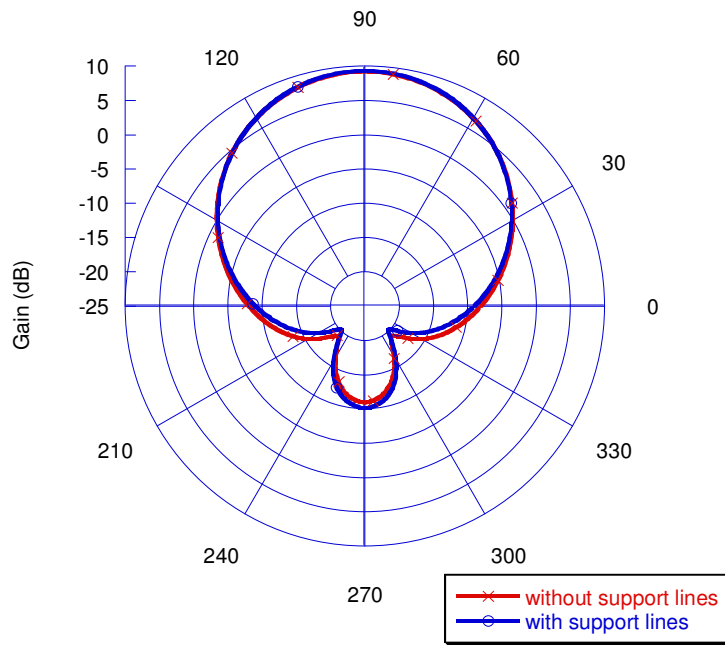
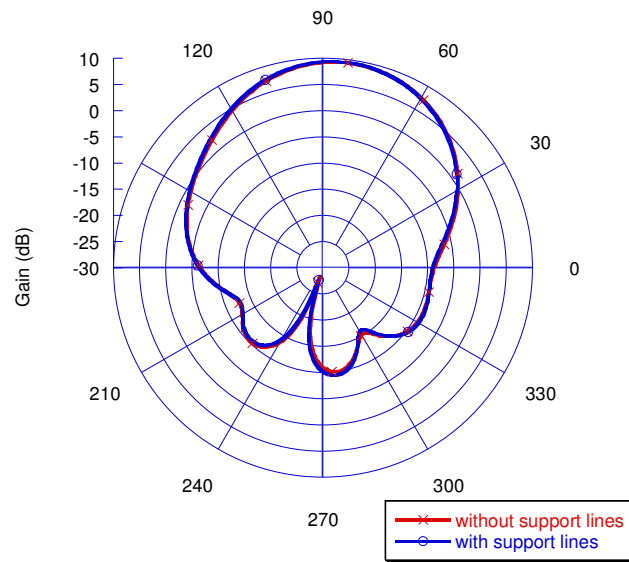


Figure 4.8: Simulated return loss.



H-plane radiation pattern, ($\theta: 90^\circ$)



E-plane radiation pattern, ($\phi: 90^\circ$)

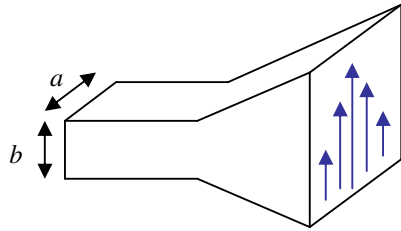
Figure 4.9: Simulated radiation patterns at 63 GHz.

The proposed supporting lines at minimum voltage points is a good solution in holding the air suspended antenna without sacrificing the performance of the antenna. However, the patch antenna is not fabricated and measured experimentally here. The experiment on the array of this patch antenna will be discussed in the next chapter.

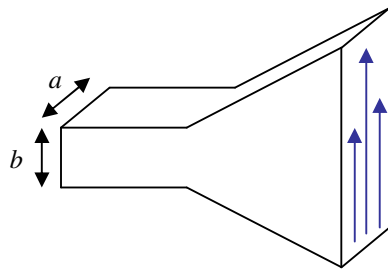
4.3 Micromachined Horn Antenna

Horn antennas are widely used, especially as feed elements for communication dishes and astronomy satellites. It can be envisioned as a waveguide with flaring at the end. The most common horn antenna types are shown in Figure 4.10.

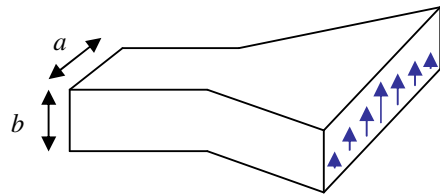
The shape of the horn can vary depending on the desired radiation characteristic. For instance, a pyramidal horn antenna shown in Figure 4.10 (a) is preferred for high gain applications. The H-plane horn antenna illustrated in Figure 4.10 (c) has a lower gain characteristic compared to pyramidal and E-plane sectoral horn (Figure 4.10 (b)). It is chosen in this study because the flare can be easily implemented in the five-layer micromachining technique proposed in this thesis.



(a) Pyramidal horn antenna.



(b) E-plane sectoral horn antenna.



(c) H-plane sectoral horn antenna.

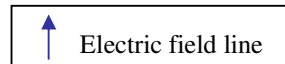


Figure 4.10: Horn antennas.

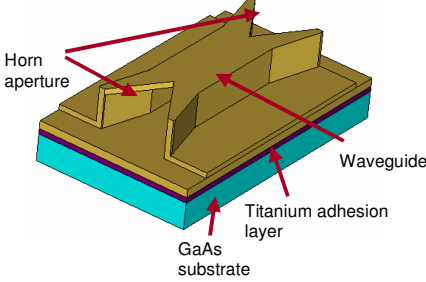
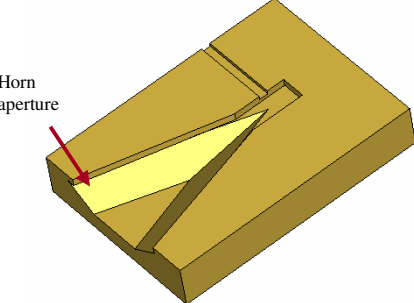
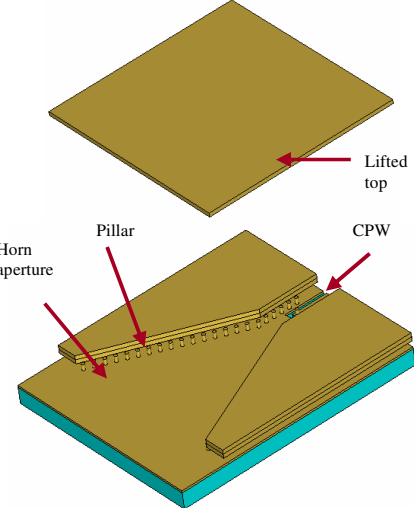
Some works on micromachined horn antennas have been reported. Table 4.2 shows three examples of micromachined horn antennas designed at millimetre wave frequencies. Two horn antennas were integrated to couple power into and out of a micromachined waveguide in [15] (Table 4.2 (a)). The structure was built on an extensive GaAs substrate with a

titanium and gold base layer above the substrate. A sacrificial photoresist layer was used to create the hollow in the waveguide and horn aperture. The main beam was found to be elevated at 27° upwards from the horn horizontal H-plane.

An octagonal micromachined horn antenna (Table 4.2 (b)) at 585 GHz was discussed in [16] yielding symmetric E-plane and H-plane beam patterns. A crystallographic etching of silicon and ultraviolet lithography of an ultra-thick SU-8 photoresist technique was proposed. The crystal planes of the silicon substrate and the thickness of the photoresist controlled the shape of the horn. A scale model at X-band was built and measured for verification. The agreement between the measured radiation pattern and the HFSS modelling was better in the scale model than in the micromachined horn. Low reflected fields in an anechoic chamber resulted in a better performance at X-band compared to the measurement performance at millimetre wave carried out on the optical table.

Micromachined integrated H-plane horn antennas (Table 4.2 (c) and (d)) were presented in [17] and [18]. Pillars with uniform spaces were fabricated on top of a metalized substrate as a lower horn side wall to allow a coplanar waveguide (CPW) feeding line to excite a signal into the antenna. Another two layers of silicon were stacked on top of the pillars as the upper side wall and covered with a top plate. However, some discrepancies between simulated and measured results are observed in [17]. Inaccurate dimensions and failure of pillars may have contributed to the disagreements in the results. These were scrutinized in their post-fabrication simulations.

Table 4.2 Micromachined horn antennas.

Structure	Frequency	Performance	Reference
 <p>(a)</p>	<p>140 – 200 GHz</p>	<p>HPBW of 31° in vertical plane and 23° in horizontal plane were achieved. The main beam elevated at 27° upwards from the horn horizontal H-plane.</p>	<p>[15]</p>
 <p>Half of the octagonal horn structure</p> <p>(b)</p>	<p>585 GHz</p>	<p>A 21.6° of HPBW was achieved. The sidelobe level is 17 dB down from the main beam peak.</p>	<p>[16]</p>
 <p>(c)</p>	<p>60 GHz</p>	<p>Achieved a high gain of 14.6 dBi. Inaccurate dimensions and failure of pillars may have contributed to the disagreements between simulated and measured results</p>	<p>[17],[18].</p>

The H-plane horn proposed in this work is linearly flared in one plane. It is built by using five layers of metal coated SU-8 thick photoresist as discussed in Chapter 2. The technique proposed here has the advantage of being dielectric free with all layers processed simultaneously. No sacrificial layer is involved, thus minimizing the cost. Furthermore, the shape of the horn is not governed by the etching process as it was in [16]. A rectangular coaxial line to ridge waveguide transition is used to excite a signal into the horn. Therefore, the side wall is made sturdy with metal coated SU-8 photoresist avoiding the pillar issue discussed above. Moreover, the horn has a very short length. This reduces the overall area and the usage of the SU-8 photoresist material.

4.3.1 H-plane Horn Antenna Design

In designing a horn antenna, a phase error, δ_e , is an important parameter that controls the directivity of the antenna. Figure 4.11 shows the wave curvature at the horn aperture. The field lines show the dominant mode expanding to a cylindrical wave [19, 20].

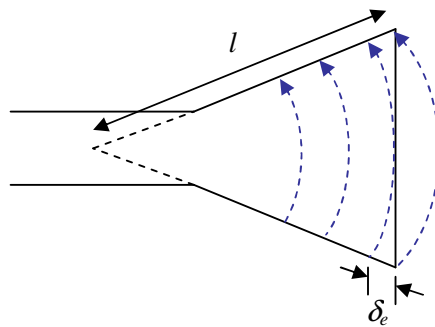


Figure 4.11: Phase error due to the wave curvature in the horn aperture.

The slant length of the horn, l , is the radius of the curvature at the aperture. The path difference between an ideal plane wave and the curved wave in the aperture is known as the phase error. This phase error contributes to losses in gain, a broadening of the radiation pattern, an increase of the sidelobe levels, and obliteration of the nulls. A simplified expression of an approximate model with error correction for small flare angle is given by [20];

$$\delta_e = \frac{a_1^2}{8l}. \quad (4.8)$$

The horn aperture, a_1 , is shown in Figure 4.12.

Studies on the gain curve of a H-plane antenna in [7, 19] show that an optimum gain occurs at $\delta_e = \frac{3}{8}\lambda$. The antenna design at the optimum gain given in [7] is only applied for a large aperture of about two wavelengths with an early assumption of zero reflection at the aperture discontinuity [20]. Furthermore, the gain presented in most literature was related to high gain (20-30 dB) horns. It was proved in [21] that the calculation was not accurate for horns with gain at about 15 dB or less. This is due to the standard approximation that leads to inaccuracy in phase error calculation and consequently error in gain estimation. The error contributes to imprecise optimum gain horn design. Some modifications were introduced to the theory. However, the optimum gain design proposed the waveguide dimension width, a , to height, b of 2:1. This is not applied here as the ridge waveguide feeding the horn is designed with a very small height compared to the width.

The H-plane horn antenna (Figure 4.12) in this work is designed with the aperture fixed at a wavelength in size, to fit into an array later. The array will be discussed in Chapter 5.

Therefore, a simple design formula assuming a path error of 0.25λ given in [22] is used to estimate the length with a wavelength aperture.

$$l = \frac{a_1^2}{2}. \quad (4.9)$$

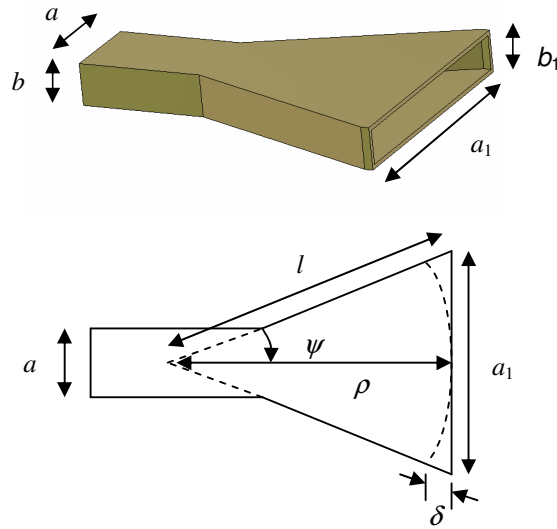


Figure 4.12: H-plane sectoral horn antenna.

The calculation gives the length of the horn to be half wavelength. An optimization using CST software has been applied giving $a_1 = 4180 \mu\text{m}$, $b_1 = 600 \mu\text{m}$, and $l = 2187 \mu\text{m}$. The five-layer structure and its layouts are shown in Figures 4.13 and 4.14, respectively.

The throat of the horn is connected to a rectangular coaxial line to ridge waveguide transition in order to feed the antenna. The transition has been detailed in the previous chapter. The performance of the horn together with the transition has been simulated using CST software and validated through a measurement.

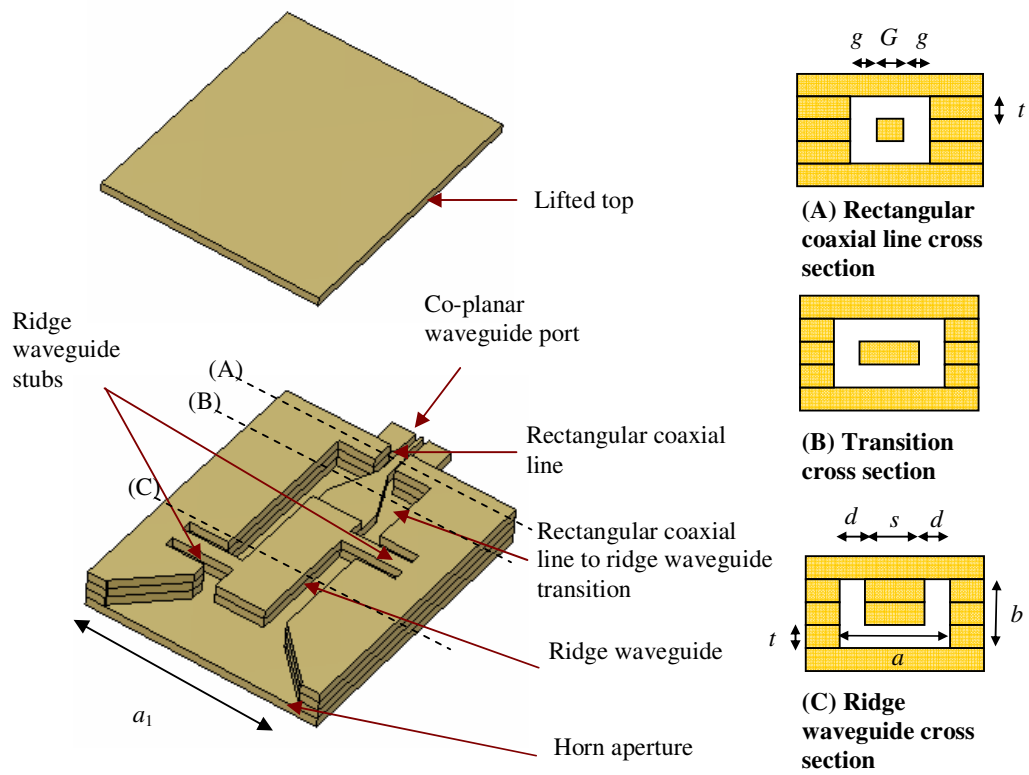


Figure 4.13: The H-plane horn structure.

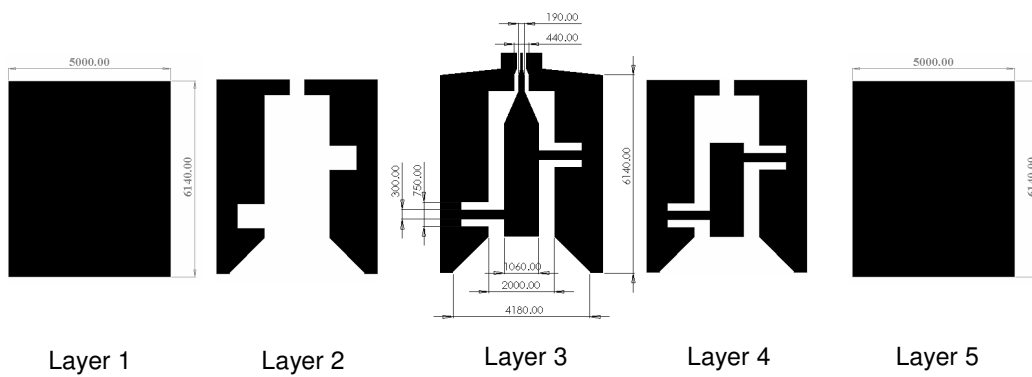


Figure 4.14: The layer layouts (all dimensions are in μm).

The simulation in lossless environment shows that structure is well matched with low return loss at the desired frequency as shown in Figure 4.15. The bandwidth from the simulated return loss plot is 4%. A 3D view and the H-plane plot of the radiation pattern are depicted in Figure 4.16. The simulation shows the antenna radiates with 48° half power beamwidth (HPBW) in the H-plane and 8.8 dB realized gain.

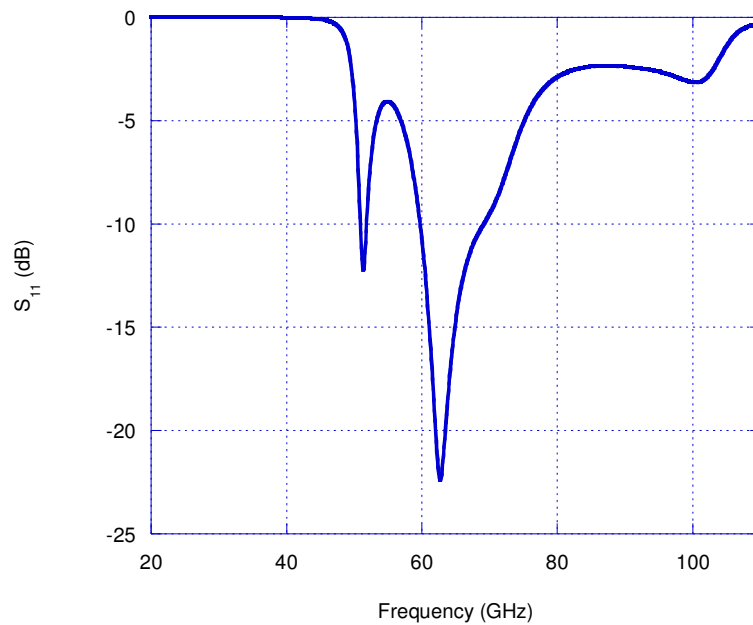
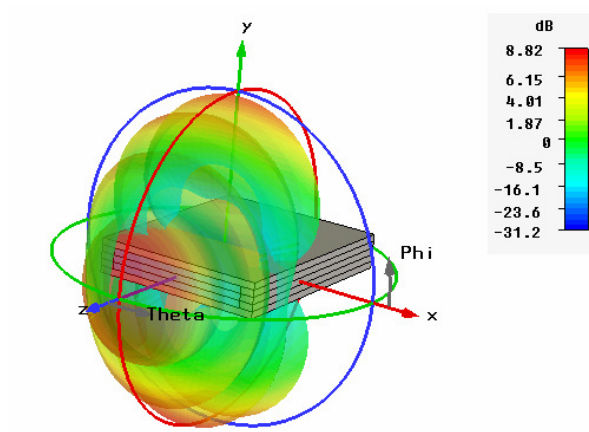
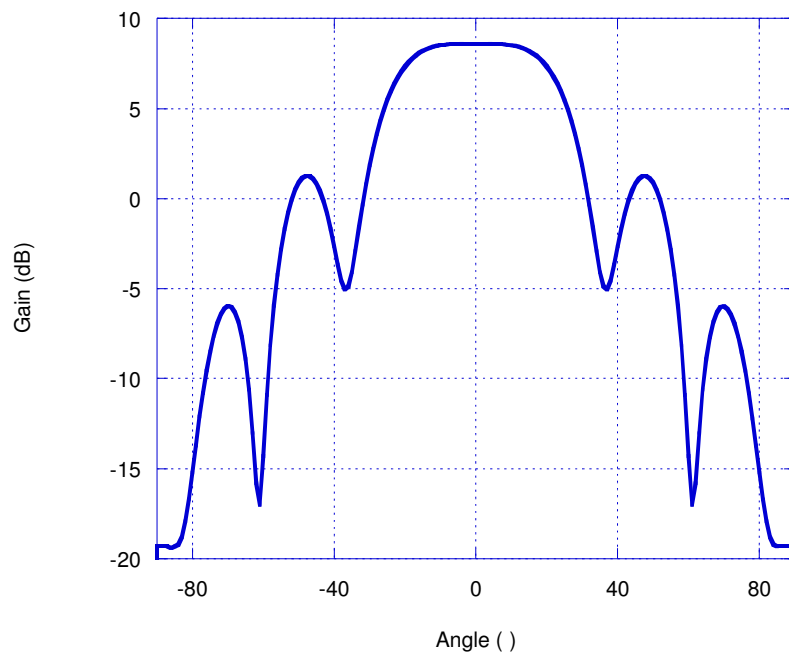


Figure 4.15: Simulated return loss of the integrated H-plane horn antenna.



Radiation pattern 3D view



H-plane radiation pattern ($\phi = 0$)

Figure 4.16: Simulated radiation pattern of the integrated H-plane horn antenna.

The horn antenna has been manufactured and the performance is validated by an experimental test. The measurement is done using an on-wafer probe measurement setup detailed in Appendix A.

A broader bandwidth in the measured return loss is observed in Figure 4.17. Losses within the structure due to manufacturing processes are thought to cause the disagreement between the measured and the simulated plot. The H-plane radiation pattern is depicted in Figure 4.18. The measured pattern generally follows the simulated pattern. However, it is hard to determine the HPBW from the measured response due to the ripples in the main lobe. Reflections from the surround might cause the ripples in the pattern.

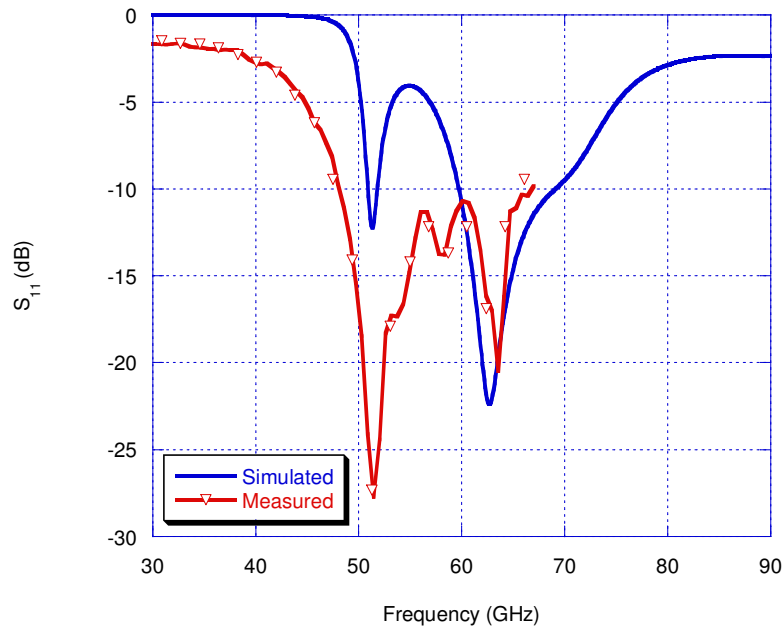


Figure 4.17: Simulated and measured return loss.

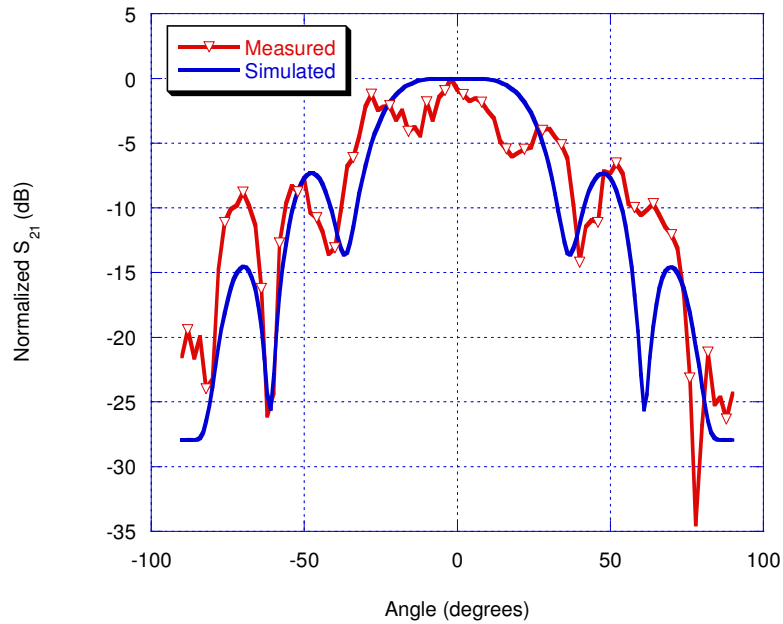
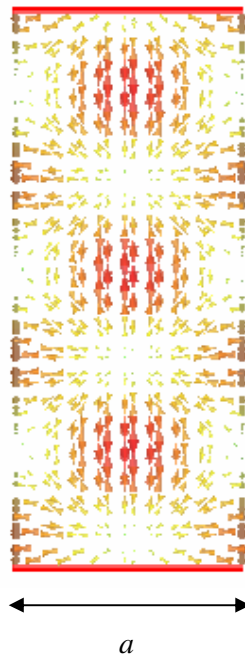
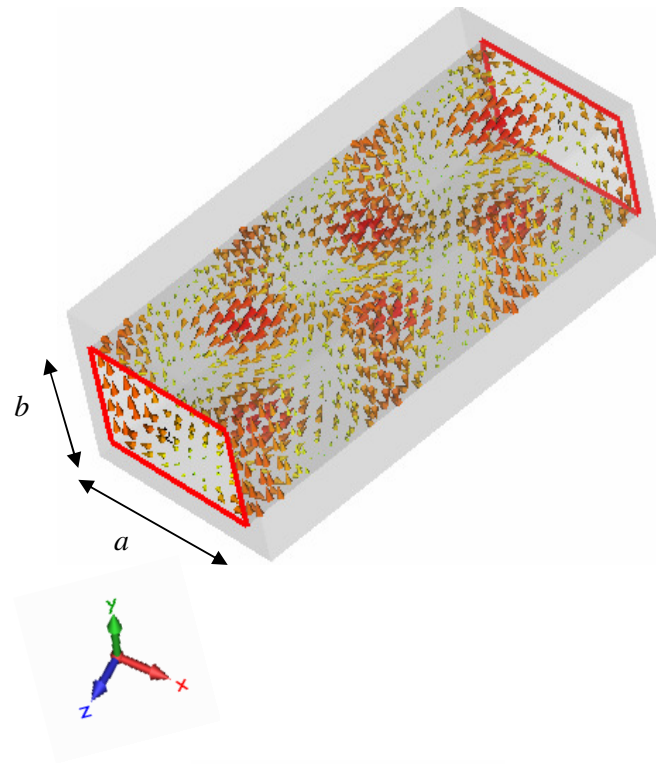


Figure 4.18: Simulated and measured radiation pattern at 63 GHz.

4.4 Ridge Waveguide Slot Antenna

This section discusses the ridge waveguide slot antenna including the design and the measurement. A ridge waveguide is used but the concept of a conventional rectangular waveguide is presented here as a basic overview.

Waveguide slot antennas are good candidates for high gain millimetre wave applications because the waveguide is a low loss transmission. The signal radiates through the slots on the waveguide walls providing the slots cut the surface current lines [20]. The dominant mode surface current lines for a rectangular waveguide and several ways of cutting the slots are shown in Figure 4.19 and Figure 4.20, respectively.



Top view

Figure 4.19: Rectangular waveguide dominant mode surface current.

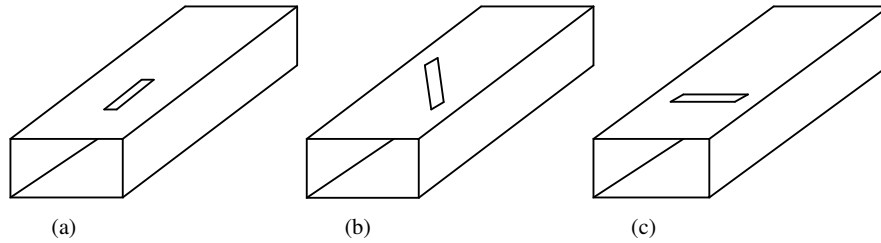


Figure 4.20: Slots on waveguide.

The energy is coupled out of the slot when the slot is aligned with the transverse component of the surface current flowing across it. The magnitude of coupled energy depends on the current density at the centre of the slot, the slot thickness and frequency. If the slot is aligned parallel to the surface current vector, it is known as a non-radiating slot. No energy is expected to radiate through the slot.

To understand how it works, let us consider the longitudinal slot in Figure 4.20 (a) placed at the centre of the waveguide with surface current lines shown in Figure 4.19. The z-component of the current does not need to travel around the slot as it is very thin. The x-component of the current may contribute to the free space radiation as the slot cuts the lines and forces them to travel around the slot. However, the x-component is zero at this position. Therefore, the slot does not radiate and is known as a non-radiating slot. The inclined slot shown in Figure 4.20 (b) is commonly used in the narrow wall.

The transverse slot in the broad wall of the waveguide as shown in Figure 4.20 (c) are not commonly used for two main reasons : 1) the grating lobes in the radiation pattern cannot be avoided due to the requirement of one-guided wavelength spacing between the slots, and 2) it is impossible to achieve a low side lobe level in the radiation pattern with limited range of coupling versus slot offset [23]. Possible solutions for the problems are to fill the waveguide with homogenous dielectric to reduce the guided wavelength, or to use a spatial filter to

suppress the grating lobes. Both problems addressed above were overcome in [23] by using inhomogeneous dielectric loads in the waveguide.

The slot antenna proposed here is air filled, having the advantage of avoiding the dielectric losses, as mentioned earlier. A longitudinal slot that would fit into the five layers structure design is preferred in this thesis. The antenna will be integrated with the transition and the coupler to form the beam, which will be discussed in Chapter 5.

The most referred-to work on conventional waveguide slot antenna design is Stegen's experimental curve that is available in [19, 20]. The measurements were carried out based on round end slots with a width of 1.5875 mm and a wall thickness of 1.27 mm in a WR-90 waveguide. The design procedure used is based on [24] with a length adjustment for the square end slots. However, Stegen's work was based on a conventional rectangular waveguide.

A decade later, a design procedure for slot arrays fed by a single ridge waveguide was reported in [25] with a ridge waveguide width of a half free space wavelength. Mutual coupling between the slots was taken into account giving different offsets on the slots. The longitudinal slot array antenna was measured above 70 GHz in [26]. It is manufactured with an integrated flange using micromachining techniques and plastic moulding process. The eight slots give a 9.6 dB gain and 13.5 dB side lobe level at 76.8 GHz.

The ridge waveguide slot antenna designed at 63 GHz presented here is air filled and very robust with higher order mode stubs holding the suspended lines within the circuit.

4.4.1 Ridge Waveguide Slot Antenna Design

The waveguide slot antenna and its equivalent circuit are illustrated in Figure 4.21. The design refers to work pioneered by Stevenson with the following assumptions: 1) a perfectly conducting thin wall, 2) a narrow slot, 3) a slot length nearly equal to half the free-space wavelength, and 4) a perfectly conducting ground plane of infinite extent [20, 27].

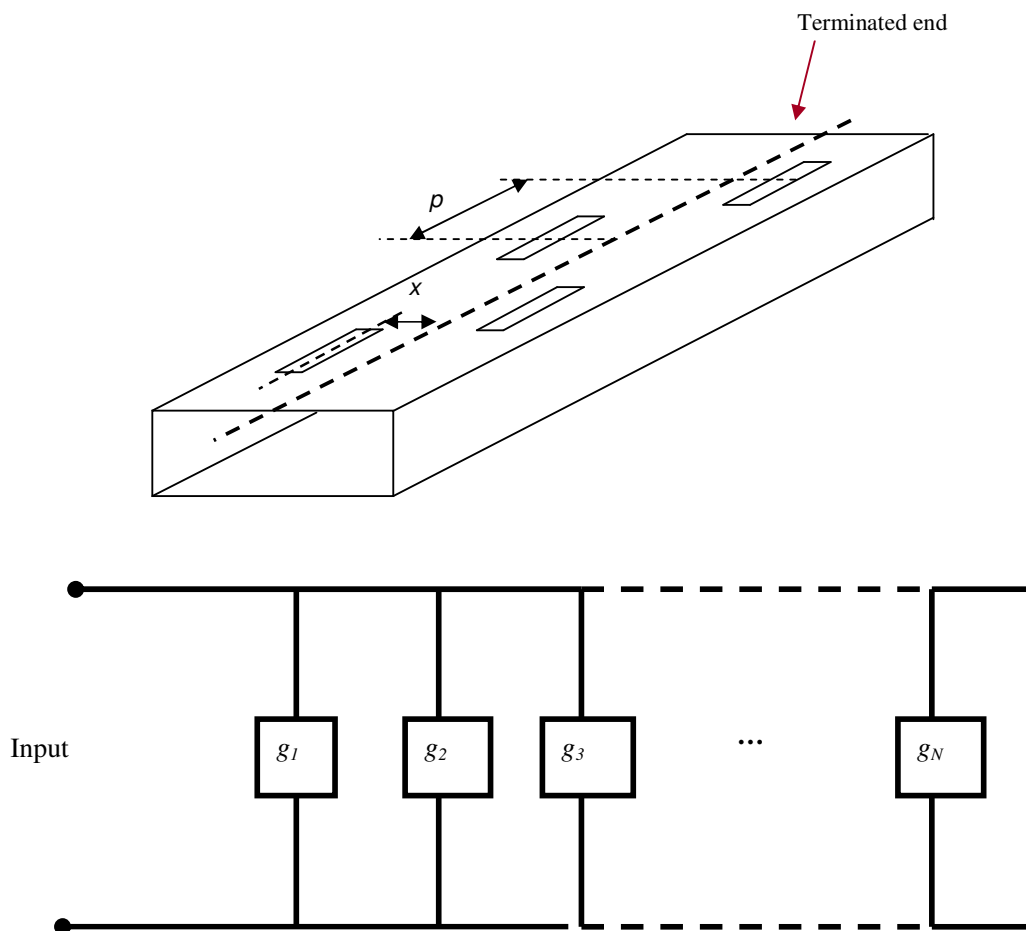


Figure 4.21: Waveguide longitudinal slot antenna and its equivalent circuit.

Referring to Figure 4.21, properly aligned slots cut on the waveguide wall will perturb the current distribution and couple energy out of the waveguide. The slots are spaced at half wavelengths. This will denote a 180° change of phase. Thus, the neighbouring slots are out of phase and the radiation will be cancelled out. Therefore, an offset is introduced to add another 180° and put them in phase.

The ridge waveguide longitudinal slot antenna design steps applied are as follows:

1. The ridge waveguide dimensions have been presented in Chapter 3. The same waveguide is used here.
2. The slot spacing is calculated to be half guided wavelength of the 63 GHz operating frequency. Theoretically, the half wavelength contributes to 180° electrical spacing, making each slot out of phase with its adjacent slot. The slots are alternate on the opposite sides of the centreline to make them radiate in phase.
3. The number of slots, n , is chosen based on the desired gain and beamwidth. An eight longitudinal slot configuration is selected here.
4. In order to get the maximum radiated power, the array of the slots needs to match the input. Thus, the equivalent shunt conductance of the array is fixed to unity.

$$g_e = \sum_{n=1}^N g_n = 1 \quad (4.12)$$

The normalized conductance is calculated based on the chosen number of slots, n .

$$g_n = \frac{1}{n}. \quad (4.13)$$

5. The resonance length of the slot is calculated at the desired operating frequency. Figure 9-7 in [19] shows that the resonant length of standard WR-90 round ended slot is $0.483 \lambda_0$ at zero offset. The resonant length of the slot is found to be a function of the offset, x , or the displacement from the centre of the waveguide. Elliot and Kurtz [24] estimate that the resonant length for a square ended slot in an infinitely thin wall as $0.464 \lambda_0$. The length can be corrected by using Stegen's experimental data in [19] as the slot is moved off-centre in the waveguide. However, optimisation using CST software is carried out here to obtain a resonant length for square ended slots at the desired frequency.
6. The displacement of the slots from the centreline, x , is determined from [20]

$$g_n = 2.09 \frac{\lambda_g}{\lambda_0} \left(\frac{a}{b} \right) \left(\cos^2 \frac{\pi \lambda_0}{2 \lambda_g} \right) \left(\sin^2 \frac{\pi x}{a} \right). \quad (4.14)$$

7. The slot width is estimated by scaling the slot width from Stegen's measurement of the WR-90 waveguide [19]. Stegen's measurements were based on a slot width of 1.5875 mm with 1.27 mm wall thickness. It also can be determined to be one-twentieth of the wavelength [24].
8. The ridge waveguide is terminated with a short circuit (enclosed in metal) at a distance of quarter wavelength from the centre of the last slot. The shorted end will let the signal to reflect back into the line and radiated through the slots.

The above design details are based on the early assumptions mentioned at the beginning of this section. Furthermore, the mutual coupling effect is also neglected. A ridge waveguide is

used here with a very small height, $b = 600 \mu\text{m}$. The smaller b -dimension will lengthen the slots [28] and make the adjacent slot ends closer to each other. This will increase the mutual coupling. Therefore, the dimensions determined are optimized using CST software to obtain a matched structure at 63 GHz frequency. It is done by setting a goal to get a minimum return loss at the desired frequency. All parameters are set to be optimised automatically in order to meet the goal. The calculated dimensions and optimized values are presented in Table 4.3.

Table 4.3 Ridge waveguide slot antenna dimensions.

	Calculated	Optimized by CST software
Slot resonant length, l	2209 μm	3200 μm
Slot width, w	250 μm	250 μm
Offset, x	141 μm	140 μm
Slot spacing, p	2381 μm	3860 μm

Figure 4.22 shows the structure and the five layers layout. The antenna is fed by a rectangular coaxial line to ridge waveguide transition with higher order mode stubs holding the ridge in the main waveguide. The performance of the designed antenna has been estimated by modelling using CST software. The simulated return loss and radiation pattern are depicted in Figures 4.23 and 4.24, respectively.

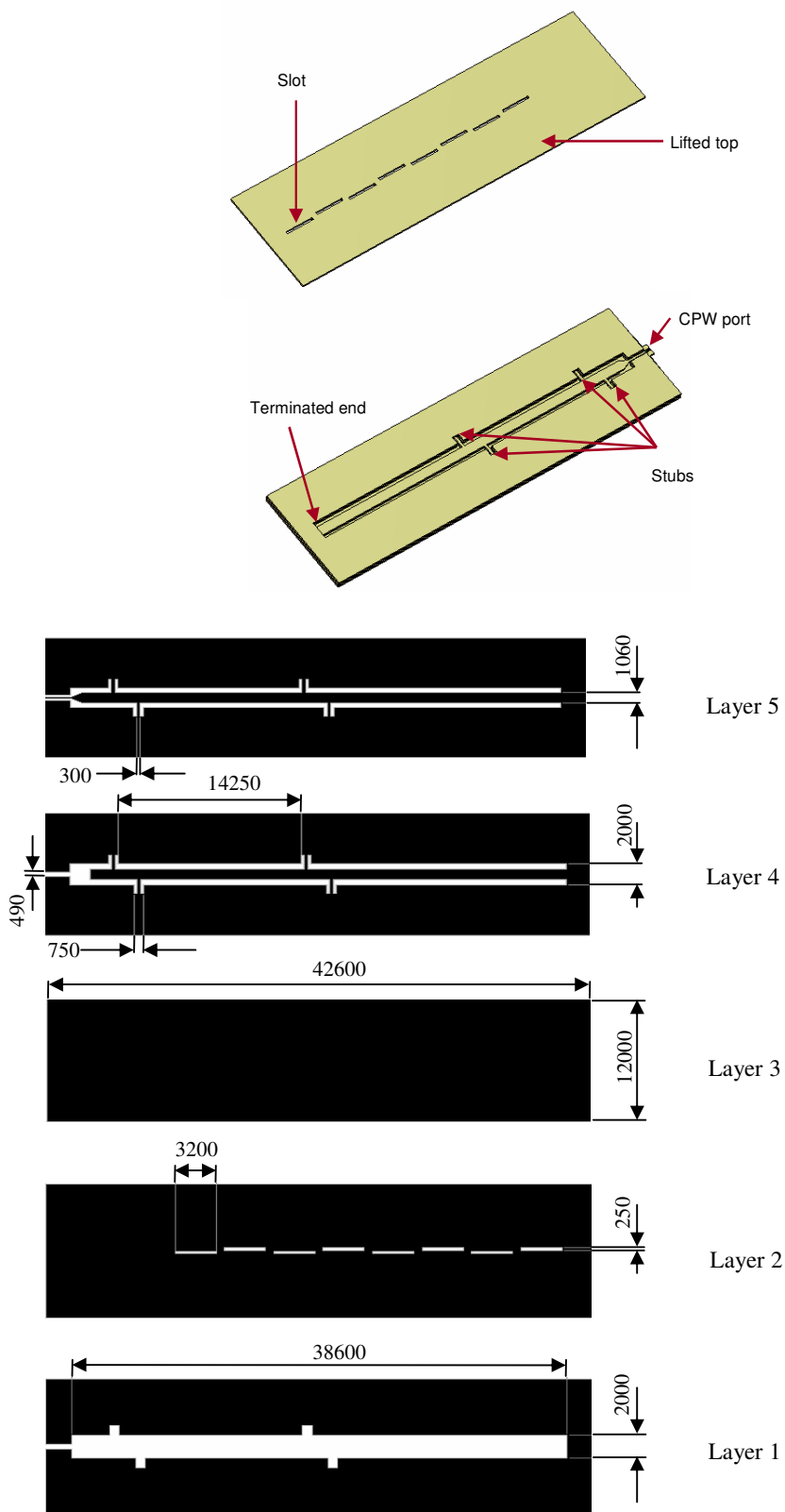


Figure 4.22: Ridge waveguide slot antenna and the layer layouts.

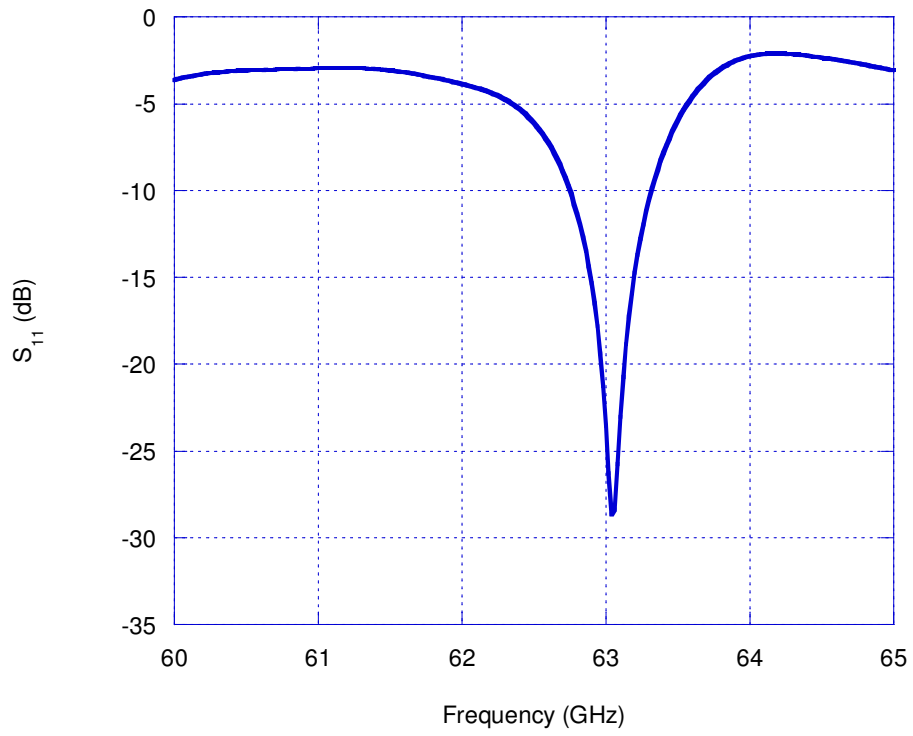
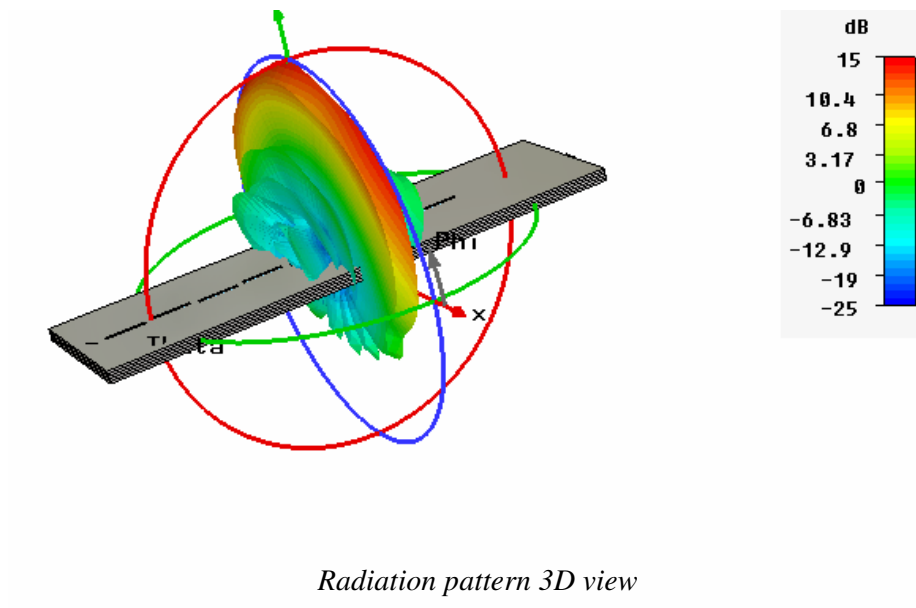
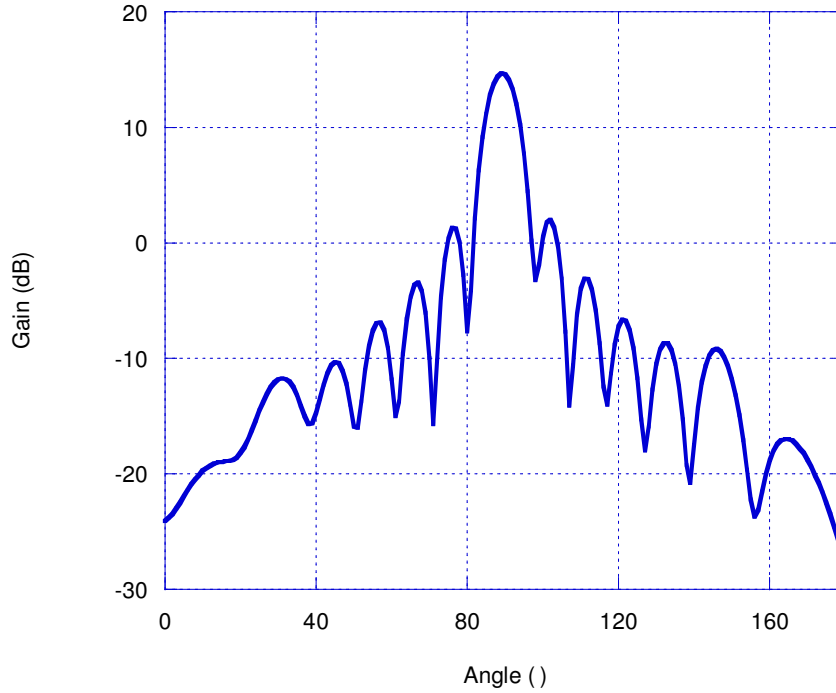


Figure 4.23: Simulated return loss of the waveguide slot antenna.





H-plane radiation pattern, ($\theta : 0^\circ$)

Figure 4.24 Simulated radiation pattern of the waveguide slot antenna at 63 GHz.

The antenna is matched at 63 GHz with -28.7 dB return loss. A very narrow -10 dB bandwidth of 0.9 % is determined from the plot. The antenna radiates at a resonant frequency of 63 GHz with 14.7 dB gain. A low side lobe level of -12.7 dB is observed.

The main lobe is tilted at 1° towards the load. This happens due to the progressive phase shift when the inter-element spacing is slightly greater or less than one-half guided wavelength. The inclined angle to the normal, θ' , of the waveguide is given by [19]

$$\sin \theta' = \frac{\lambda_0}{\lambda_g} - \frac{\lambda_0}{2l}. \quad (4.15)$$

Equation (4.13) shows that the beam peak angle is frequency dependent. The beam angle will move towards the load end when the frequency is increased.

The antenna has been manufactured and tested. A low return loss of -18.5 dB is observed at 63 GHz, as shown in Figure 4.25. However, the measured radiation pattern is far from expected, as shown in Figure 4.26. This may happen due to imperfections on the waveguide wall. Layer curvature observed before the bonding process may result in air gaps between the joined layers, consequently causing signal losses. Thus, the signal may not radiate as expected.

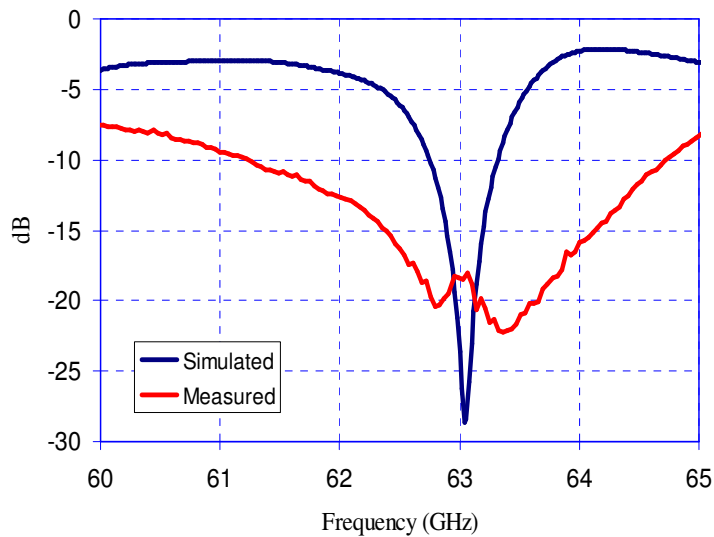


Figure 4.25 Simulated and measured return loss.

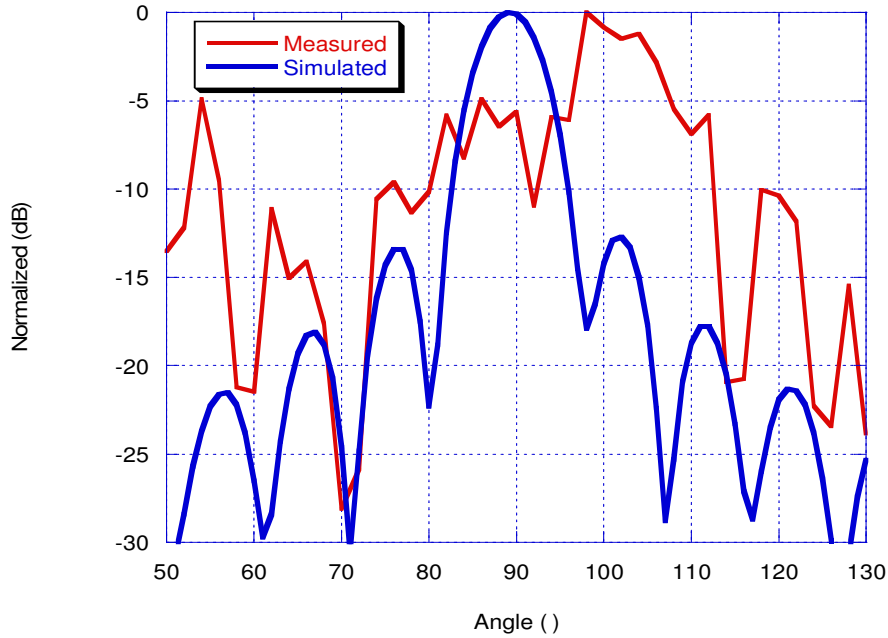


Figure 4.26 Simulated and measured radiation pattern.

4.5 Summary

Table 4.4 shows the performance comparison of the antennas at 63 GHz, including the return loss (S_{11}), half power beamwidth (HPBW), side lobe level (SLL) and the realized gain.

The patch and the slot antennas exhibit a very high gain compared to the horn antenna. The low gain characteristic was expected from an H-plane sectoral horn antenna. The slot antenna is very directive with smallest HPBW compared to the other two antennas.

Table 4.4 Comparisons of the antenna performances at 63 GHz.

		Simulated	Measured
Air suspended patch antenna	S_{11} :	-36.7 dB	-
	Bandwidth :	5.2 %	-
	HPBW :	65.1°	-
	SLL :	-20.3 dB	-
	Gain :	15.3 dB	-
H-plane horn antenna	S_{11} :	-22.8 dB	-18.3 dB
	Bandwidth :	14.6 %	29.4 %
	HPBW :	48°	-
	SLL :	-7.7 dB	-
	Gain :	8.8 dB	-
Ridge waveguide slot antenna	S_{11} :	-28.6 dB	-18.5 dB
	Bandwidth :	0.9 %	4.9 %
	HPBW :	7.9°	-
	SLL :	-12.7 dB	-
	Gain :	14.7 dB	-

A new micromachined H-plane horn antenna integrated with a rectangular coaxial line to ridge waveguide transition has been designed and tested here. The ridge which is normally extended with curvature into the horn aperture is stopped at the antenna throat. This antenna is sturdy and suitable for use at millimetre wavelength [29]. It possesses a wide bandwidth

compared to the other two antennas. Modifications could be implemented in future to suit other applications of the antenna.

The single patch antenna has not been tested experimentally. A patch array structure is manufactured and tested, but it will be discussed in Chapter 5. The simulation shows that the antenna is matched with narrow bandwidth but very wide HPBW and very high realized gain.

The ridge waveguide slot antenna is also an excellent candidate for millimetre wavelength applications. However, the height of the ridge needs to be greater. This will help to reduce the resonant length of the slot and therefore reduce the overall surface area. A large surface area with a thin layer thickness gives difficulty in the micromachining manufacturing process. The thin layers with large area are easily bent and curved. This may result in fractures on the structure and imperfect walls during the bonding process. The ridge waveguide slot antenna here has been fabricated and measured. Imperfections introduced into the structure during the fabrication process may have contributed to degradation in the measurement results.

The antenna array performances will be presented in Chapter 5 with the Butler matrix beamforming configuration.

References

- [1] I. Bahl and P. Bhartia, *Microstrip Antenna*: Artech House, 1980.
- [2] B. G. Duixian Liu, Ullrich Pfeiffer, Janusz Grzyb, "Advanced Millimeter-wave Technologies," 2009.
- [3] J.-S. Hong and M. J. Lancaster, *Microstrip Filters For RF/Microwave Applications*: John Wiley & Sons, 2001.

- [4] G. P. Gauthier, A. Courtay, and G. M. Rebeiz, "Microstrip Antennas on Synthesized Low Dielectric Constant Substrate," *IEEE Transactions on Antennas and Propagation*, vol. 45, pp. 1310-1314, 1997.
- [5] Q. Chen, V. F. Fusco, M. Zheng, and P. S. Hall, "Micromachined Silicon Antenna," in *International Conference on Microwave and Millimeter Wave Technology*, Washington DC, 1998, pp. 289-292.
- [6] I. Papapolymerou, R. F. Drayton, and L. P. B. Katehi, "Micromachined Patch Antennas," *IEEE Transactions on Antennas and Propagation*, vol. 46, pp. 275-283, 1998.
- [7] C. A. Balanis, *Antenna Theory Analysis and Design*, 2nd ed.: John Wiley & Sons, 1997.
- [8] Y. Huang and K. Boyle, *Antennas : From Theory to Practice*: John Wiley & Sons, 2008.
- [9] I. J. Bahl and P. Bhartia, *Microstrip Antennas*: Artech House Inc., 1980.
- [10] *CST Microwave Studio*: CST GmbH, Darmstadt, Germany., 2006.
- [11] P. Sharma and S. K. Koul, "Design and Development of Millimeter Wave Micromachined Patch Antennas," *IETE Journal of Research*, vol. 55, pp. 40-50, 2009.
- [12] J.-G. Kim, H. S. Lee, H.-S. Lee, J.-B. Yoon, and S. Hong, "60-GHz CPW-fed post-supported patch antenna using micromachining technology," *IEEE Microwave and Wireless Components Letters*, vol. 15, pp. 635-637, 2005.
- [13] Y. Wang, M. L. Ke, and M. J. Lancaster, "Micromachined Air Filled Patch Antennas for Millimeter Wave Applications," *Microwave and Optical Technology Letters*, vol. 52, pp. 1345-1347, 2010.
- [14] T. Y. Lee and P. Gardner, "Air-spaced Beamforming Patch Antenna Array," *IET Electronic Letters*, vol. 40, pp. 714-715, 2004.
- [15] J. W. Digby, C. E. Collins, B. M. Towlson, L. S. Karatzas, G. M. Parkhurst, J. M. Chamberlain, J. W. Bowen, R. D. Pollard, R. E. Miles, D. P. Steenson, D. A. Brown, and N. J. Cronin, "Integrated micro-machined antenna for 200 GHz operation," in *IEEE MTT-S International Microwave Symposium Digest 1997*, pp. 561-564.
- [16] J. L. Hesler, K. Hui, R. K. Dahlstrom, R. M. Weikle, T. W. Crowe, C. M. Mann, and H. B. Wallace, "Analysis of an octagonal micromachined horn antenna for submillimeter-wave applications," *IEEE Transactions on Antennas and Propagation*, vol. 49, pp. 997-1001, 2001.
- [17] B. Pan, Y. Li, G. E. Ponchak, M. M. Tentzeris, and J. Papapolymerou, "A Low-loss Substrate-independent Approach for 60 GHz Tranceiver Front-end Integration Using Micromachining Technologies," *IEEE Transactions on Microwave Theory and Techniques*, vol. 56, pp. 2779-2788, 2008.
- [18] B. Pan, L. Yuan, G. E. Ponchak, J. Papapolymerou, and M. M. Tentzeris, "A 60-GHz CPW-Fed High-Gain and Broadband Integrated Horn Antenna," *Antennas and Propagation, IEEE Transactions on*, vol. 57, pp. 1050-1056, 2009.
- [19] H. Jasik, *Antenna Engineering Handbook*: McGraw Hill Inc., 1961.
- [20] R. C. Johnson, "Antenna Engineering Handbook," 3 ed, 1993.
- [21] D. C. Hawkins and F. Thompson, "Modifications to the theory of waveguide horns," *IEEE Proceedings-H*, vol. 140, pp. 381-386, 1993.
- [22] F. R. Connor, *Antennas*: Edward Arnold, London, 1989.

- [23] J. Joubert, "A Transverse Slot in the Broad Wall of Inhomogeneously Loaded Rectangular Waveguide for Array Applications," *IEEE Microwaves and Guided Letters*, vol. 5, pp. 37-39, 1995.
- [24] R. S. Elliot and L. A. Kurtz, "The Design of Small Slot Arrays," *IEEE Transactions on Antennas and Propagation*, vol. 26, pp. 214-219, 1978.
- [25] D. Y. Kim and R. S. Elliot, "A Design Procedure for Slot Arrays Fed by Single Ridge Waveguide," *IEEE Transactions on Antennas and Propagation*, vol. 36, pp. 1531-1536, 1988.
- [26] Y.-K. Fuh, A. Margomenus, Y. Jiang, and L. Lin, "Micromachined W-band Plastic Slot Array Antenna with Self Aligned and Integrated Flange," in *International Solid State Sensors, Actuators and Microsystems Conference USA*, 2009, pp. 2122-2125.
- [27] A. F. Stevenson, "Theory of Slots in Rectangular Waveguides," *Journal of Applied Physics*, vol. 19, pp. 24-38, 1948.
- [28] R. S. Elliot, *Antenna Theory and Design*: Prentice Hall, Inc., 1981.
- [29] N. A. Murad, M. J. Lancaster, P. Gardner, M. L. Ke, and Y. Wang, "Micromachined H-Plane Horn Antenna Manufactured Using Thick SU-8 Photoresist " *IET Electronics Letters*, vol. 46, 2010.

Chapter 5

Micromachined Coupler and Butler Matrix

Beamforming

5.1 Introduction

This chapter discusses antenna beamforming using the Butler matrix configuration. A coupler as the main component in building the Butler matrix is presented first. A coupler in this context is a passive device that conveys energy to either one of two output ports.

A directional coupler can be represented as a multi-port network as shown in Figure 5.1. The structure can be considered to have four ports, which are the input, direct, coupled and isolated. Let us consider P_1 , P_2 , P_3 , and P_4 as the powers available at ports 1, 2, 3 and 4, respectively. The input power fed into port 1 will be directed to port 2 and coupled to port 3, while isolated or not transmitted to port 4. Hence, the two main parameters that describe the performance of the network are the *Coupling Factor* and the *Directivity* [1].

$$\text{Coupling Factor (dB)} = 10 \log \frac{P_1}{P_3} \quad (5.1)$$

$$\text{Directivity (dB)} = 10 \log \frac{P_3}{P_4} \quad (5.2)$$

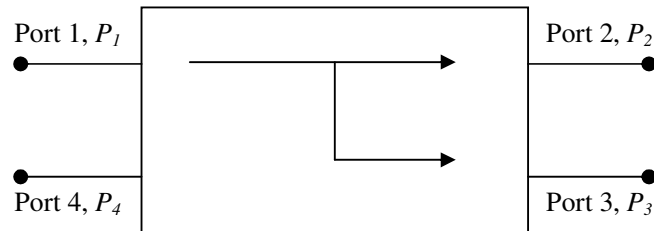


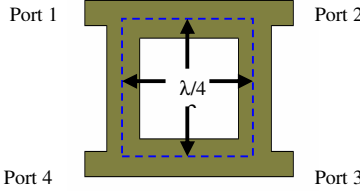
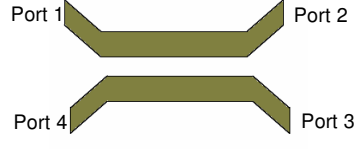
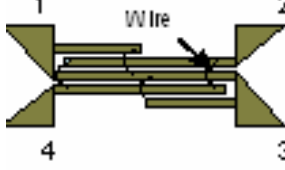
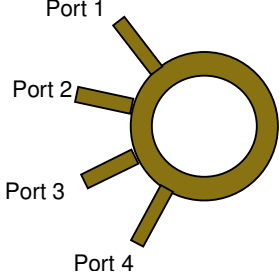
Figure 5.1: Four port network.

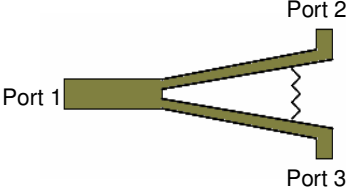
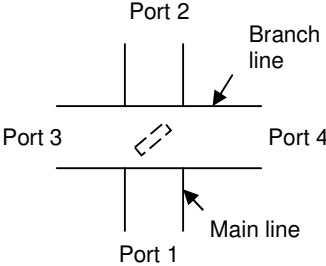
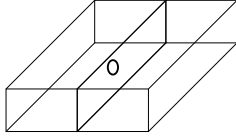
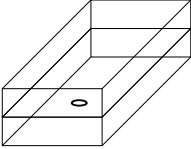
5.2 Types of Coupler

The characteristics of couplers can be varied and built using different types of transmission line. In most applications, a single section coupler exhibits a small bandwidth. A multi-section or cascaded structure can enhance the bandwidth.

Table 5.1 gives a summary of different types of coupler.

Table 5.1 Different types of coupler [1-3].

Coupler	Structure	Characteristics
Branch line coupler (BLC).		<p>The bandwidth is limited to a maximum of 20%. It can be increased by using multiple sections in cascade. Bandwidth can also be increased by using stubs in the structure[4]. This coupler is easy to design and can be built by using any transmission line.</p>
Coupled line.		<p>Multisections can increase the bandwidth but the coupling will be low. Striplines are preferred in building this kind of coupler. It possesses weak coupling. A tight coupling requires lines that are close to each other.</p>
Lange Coupler.		<p>Easily achieved 3dB coupling factor compared to coupled line. This coupler can be manufactured using any type of transmission line. It needs wire bonding between lines which is not preferred in the micromachining technique used here.</p>
Ring hybrid.		<p>Up to 30% bandwidth can be achieved. An additional section or a symmetric ring circuit may increase the bandwidth. Coupling is normally 3dB. This coupler can be designed using any type of transmission line.</p>

Wilkinson Power divider.		<p>The multisection structure can increase the bandwidth. Direct power divider. No phase difference. This structure is a direct power divider.</p>
Cross guide.		<p>Coupling of this cross guide waveguide coupler is limited. 5dB might be achieved using reduced height crossed waveguide.</p>
Sidewall and top-wall waveguide coupler.		<p>Need central capacitive matching to give good performance at 3dB.</p>
Waveguide Bethe-hole coupler.		<p>Single-hole possesses a narrow bandwidth. Bandwidth can be improved by implementing multi-hole on the waveguide. It operates properly at its designed frequency, but the coupling level alters when it deviates from the designed frequency. This is an old fashioned waveguide coupler and rarely or no longer used.</p>

The branch line coupler is considered in this thesis due to its simplicity and the fact that it can be designed using any type of transmission line. The coupled line cannot be implemented using the rectangular coaxial line proposed here since the signal is shielded within the outer conductor. Waveguide couplers are not covered here as they are restricted to waveguide structures.

5.3 Hybrid Branch Line Coupler

The term hybrid describes the 90° phase difference between the two outputs of the coupler. The branch-line coupler has four symmetrical ports and is shown in Figure 5.2 in its microstrip form. For this coupler, any port can be an input port. Output ports are on the opposite side to the input port, while the port of the same side as the input port is isolated. For instance, if the input is from Port 1, then Port 2 and Port 3 become the outputs and Port 4 is isolated. The outputs are usually of equal amplitude but quadrature phase [3]. The coupling factor can be determined by the ratio of the shunt and series arm impedance (shown in Figure 5.2) and is optimised to maintain a proper match over the required bandwidth [1].

The coupler is designed using quarter wavelength transmission lines which are ideally matched at only one frequency. Thus, this coupler exhibits a narrow bandwidth, as mentioned in Table 5.1.

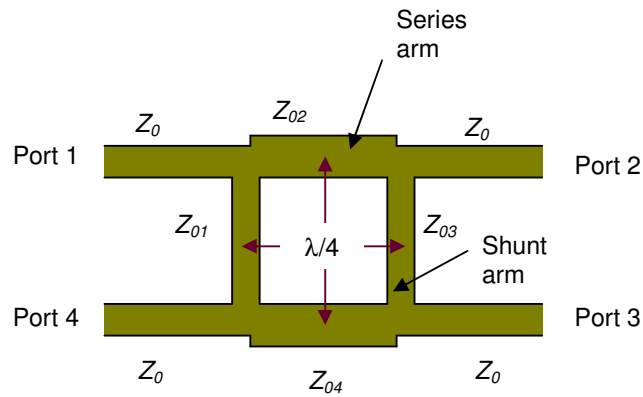


Figure 5.2: Hybrid 3-dB branch line coupler.

5.3.1 Odd and Even Mode Analysis

The branch line coupler can be analyzed using odd-mode and even-mode analysis [3]. Let us consider the branch line coupler circuit diagram shown in Figure 5.3 with all impedances normalized to Z_0 .

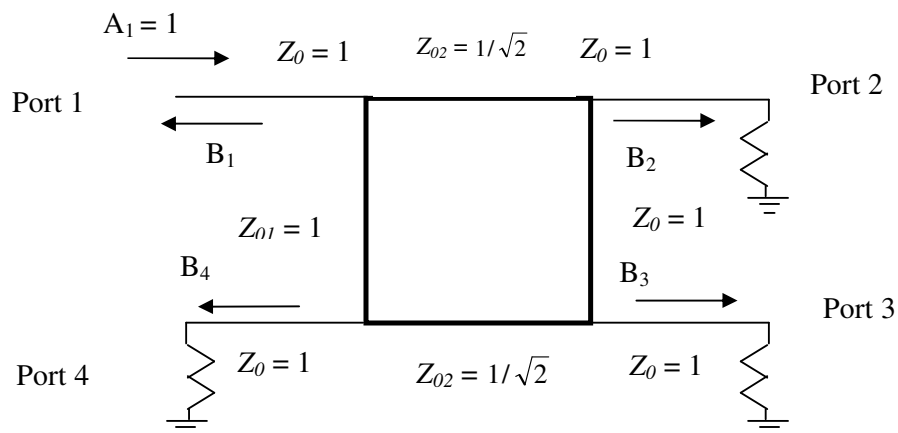


Figure 5.3: Circuit diagram of normalized branch line coupler.

Referring to Figure 5.3, A_1 is assumed to be an incident wave with amplitude of 1 at port 1. Due to the symmetry or anti-symmetry of the excitation, the four-port network can be decomposed into two decoupled two-port networks as shown in Figure 5.4(a) and 5.4(b).

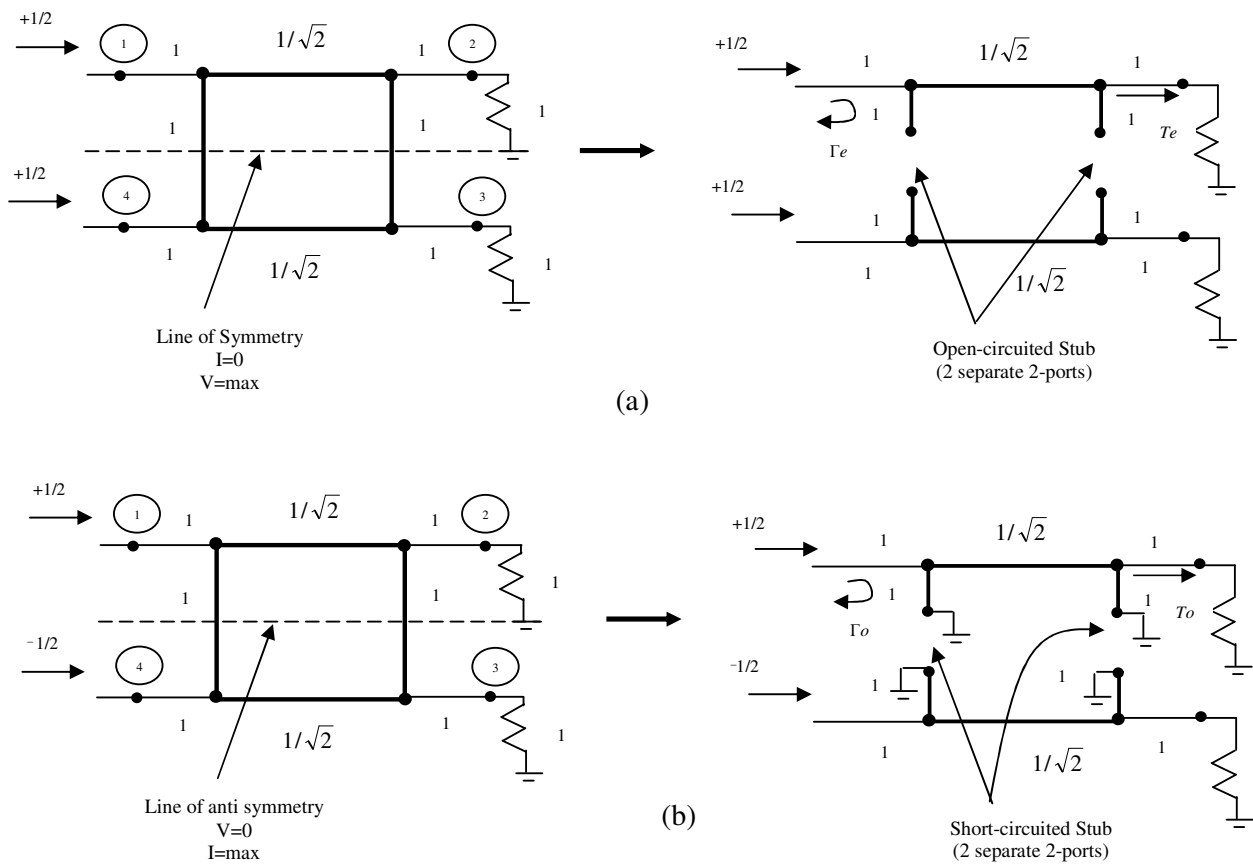


Figure 5.4: Decomposition of Branch Line Coupler into (a) even and (b) odd mode excitation [3].

The incident waves for the two-port are $+1/2$ and $-1/2$, as shown in Figure 5.4. The amplitude of the emerging wave at each port can be written as follows.

$$B_1 = \frac{1}{2}\Gamma_e + \frac{1}{2}\Gamma_o \quad , \quad (5.3)$$

$$B_2 = \frac{1}{2}T_e + \frac{1}{2}T_o \quad , \quad (5.4)$$

$$B_3 = \frac{1}{2}T_e - \frac{1}{2}T_o \quad , \quad (5.5)$$

$$B_4 = \frac{1}{2}\Gamma_e - \frac{1}{2}\Gamma_o \quad , \quad (5.6)$$

where Γ_e and Γ_o = even and odd mode of reflection coefficients for two port networks

T_e and T_o = even and odd mode of transmission coefficients for two port networks

The ABCD matrix multiplication of each cascade component of the even-mode two-port circuit is given as follows

$$\begin{bmatrix} A & B \\ C & D \end{bmatrix}_e = \underbrace{\begin{bmatrix} 1 & 0 \\ j & 1 \end{bmatrix}}_{\text{Shunt } Y=j} \underbrace{\begin{bmatrix} 0 & j/\sqrt{2} \\ j\sqrt{2} & 0 \end{bmatrix}}_{\lambda/4 \text{ line}} \underbrace{\begin{bmatrix} 1 & 0 \\ j & 1 \end{bmatrix}}_{\text{Shunt } Y=j} = \frac{1}{\sqrt{2}} \begin{bmatrix} -1 & j \\ j & -1 \end{bmatrix} \quad . \quad (5.7)$$

The admittance of the shunt open circuit $\lambda/8$ stubs is given by

$$Y = j \tan \beta \ell = j \quad . \quad (5.8)$$

The ABCD parameters can be converted to the S-Parameters that are equivalent to the reflection and transmission coefficients of the even mode.

$$\Gamma_e = \frac{A+B-C-D}{A+B+C+D} = \frac{(-1+j-j+1)/\sqrt{2}}{(-1+j+j-1)/\sqrt{2}} = 0 \quad (5.9)$$

$$T_e = \frac{2}{A+B+C+D} = \frac{2}{(-1+j+j-1)/\sqrt{2}} = \frac{-1}{\sqrt{2}}(1+j) \quad (5.10)$$

For the odd-mode, the ABCD matrix multiplication gives

$$\begin{bmatrix} A & B \\ C & D \end{bmatrix} = \frac{1}{\sqrt{2}} \begin{bmatrix} 1 & j \\ j & 1 \end{bmatrix} \quad . \quad (5.11)$$

Subsequently, the reflection and transmission coefficients of the odd-mode are

$$\Gamma_o = 0 \quad (5.12)$$

$$T_o = \frac{1}{\sqrt{2}}(1-j) \quad (5.13)$$

Substituting equations (5.9), (5.10), (5.12) and (5.13) into (5.3) to (5.6), the following results can be obtained that describe the fundamental operations of the branch line coupler.

$$B_1 = 0 \quad (\text{port 1 is matched}), \quad (5.14)$$

$$B_2 = -\frac{j}{\sqrt{2}} \quad (\text{half power, } -90^\circ \text{ phase shift from port 1 to port 2}), \quad (5.15)$$

$$B_3 = -\frac{1}{\sqrt{2}} \quad (\text{half power, } -180^\circ \text{ phase shift from port 1 to port 3}), \quad (5.16)$$

$$B_4 = 0 \quad (\text{no power to port 4}), \quad (5.17)$$

5.3.2 Design and Characteristics

A branch line coupler is designed with quarter wavelength lines at different impedances depending on the required characteristics. Referring to Figure 5.2, the characteristic impedances are given as follows [5].

$$Z_{01} = \frac{Z_{in}}{k} \quad , \quad (5.18)$$

$$Z_{02} = \sqrt{\frac{Z_{in} \cdot Z_{out}}{1+k^2}} \quad , \quad (5.19)$$

$$Z_{03} = \frac{Z_{01} Z_{out}}{Z_{in}} \quad , \quad (5.20)$$

$$Z_{04} = Z_{02} \quad , \quad (5.21)$$

$$k = \left| \frac{S_{31}}{S_{21}} \right| , \quad (5.22)$$

where Z_{in} is the input impedance, Z_{out} is the output impedance and k is the coupling factor. In this case, $Z_{in} = Z_{out} = Z_0$, while $k = 1$. Therefore, the impedances can be simplified as

$$Z_{01} = Z_{03} = Z_0 , \quad (5.23)$$

$$Z_{02} = Z_{04} = \frac{Z_0}{\sqrt{2}} , \quad (5.24)$$

where Z_0 is the characteristic impedance of the input line.

The branch line coupler here is designed using air filled rectangular coaxial lines. The impedances are translated into physical lines by using the procedure described in Chapter 3, section 3.2.1. The line dimensions are presented in Table 3.1. Again, a stub supporting structure is implemented here. The diagram is shown in Figure 5.5.

The stub placements can enhance the coupler bandwidth. A comparison between two different stub arrangements was presented in [4]. The bandwidth of the coupler with stubs placed at the corners of the coupler branches follows the conventional coupler bandwidth but is enhanced by 15% when they are moved a quarter wavelength away from the corners. Here, the bandwidth is not crucial. The stubs are placed at the corners of the branches.

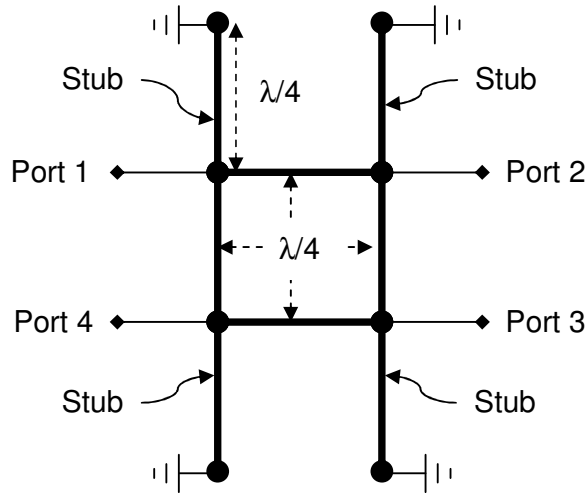


Figure 5.5: The branch line coupler with shorted stubs.

Practically, it is difficult to fit in the physical stubs into the transmission-line loop area in the middle of the structure. Therefore, the loop island (area is shown in Figure 5.6) is void, leaving the branches in semi-coaxial lines. The signal within this one side wall semi-coaxial line area is not fully covered. Therefore, the coupling within the structure is increased and the bandwidth is slightly broadened[4]. The impedances and dimensions of the semi-coaxial line determined by simulations are shown in Table 5.2. These dimensions are subject to junction effects. In practice, the junctions introduce parasitic reactance, which consequently alters the electrical length of the lines at the interconnecting junctions. Optimisation as described in [4] is carried out to achieve the required performance. The optimisation procedure adopted here start with adjusting the physical length of shunt and series arms to the desired centre frequency. Then, the impedance of the branch lines is tuned to balance the through (S_{21}) and coupled (S_{31}) outputs. The optimised dimensions are also presented in Table 5.2.

Table 5.2 The impedances (in ohms) and dimensions (in μm) of semi-coaxial lines.

g	Before optimization		After optimization (coupler)	
	W	Z_0	W	Z_0
135	380	50.0	320	54.4
135	690	35.4	570	40.0

The performance of the designed structure is estimated by modelling in CST software. Figure 5.6 shows the structure without the outer wall to assist viewing. The faded blue area represents the air between the outer and the inner conductor wall.

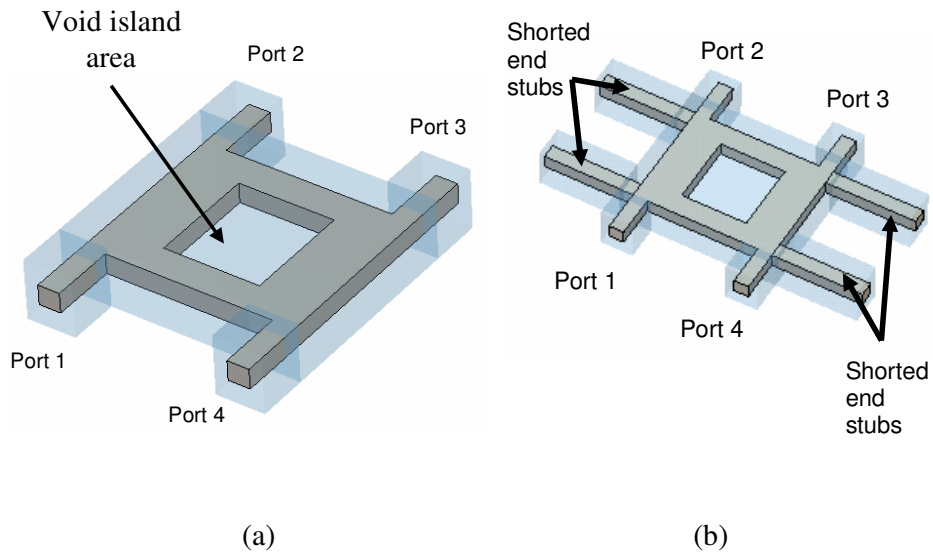


Figure 5.6: Branch line coupler (a) without and (b) with stubs.

The performances of the structure are shown in Figures 5.7 and 5.8, respectively. The insertion loss here denotes the ratio of the output power at the through and couple ports to the input power. Ideally, the input power is spread equally between these two output ports, which denote -3.0 dB of insertion loss at the desired frequency. Without stubs, the transmitted power at port 2 is -3.05 dB and the coupled power at port 3 is -3.01 dB. The output phase difference is 90.01° . The -1.0 dB bandwidth is 27.0 %, calculated from the response. The return loss and isolation are better than -25.0 dB at the desired frequency.

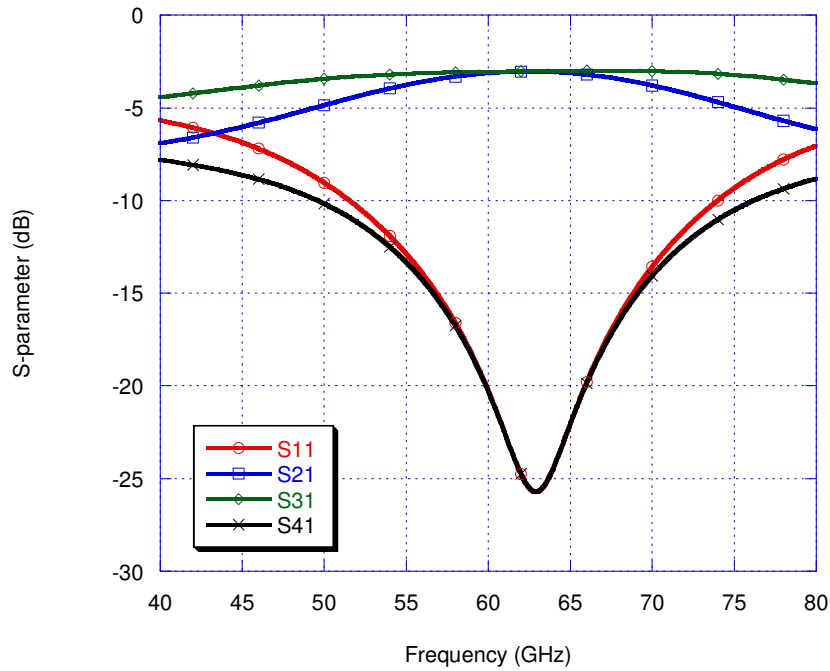


Figure 5.7: Simulated S-parameters of the coupler without stubs.

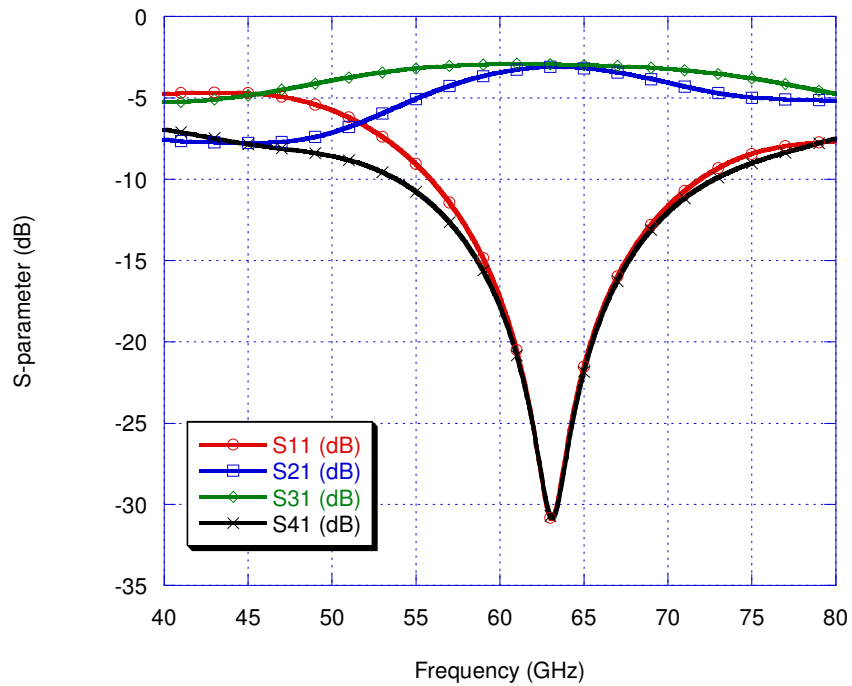


Figure 5.8: Simulated S-parameters of the coupler with stubs.

The coupler with supporting stubs shown in Figure 5.6 (b) is optimised to get the desired response. The return loss is better than -30.0 dB at 63 GHz with a transmitted power of -3.10 dB and -2.92 dB is coupled to port 3. The phase difference between the two output ports is 90.11°.

The above designed coupler with supporting stubs at the branch corners will be implemented in the next section to form the beam of the antenna array. The input from different ports will form the beam at two different angles due to the phase difference of the output ports.

5.4 Butler Matrix Beamforming

The Butler matrix introduced by Butler [6] consists of N input ports with an equal number of output ports. A signal introduced at one particular input port produces equal amplitude but constant phase difference between all output ports. Therefore, the beam of an antenna array can be formed at certain angle in space by using the Butler matrix characteristic. Moody defined the phase difference between radiating element for N element Butler matrix as [7]

$$\Delta\psi = \pm \frac{2n-1}{N} \times 180^\circ, \quad (5.11)$$

where N is the order of the matrix and n is an integer varying from 1 to N . For instance, a 4x4 Butler matrix will give $\pm 45^\circ$ phase difference for output at ports 1 and 4, while $\pm 135^\circ$ phase difference will be gained at ports 2 and 3. Figure 5.9 shows a 4x4 Butler matrix network topology with the phase shift and phase difference tabulated in Table 5.2.

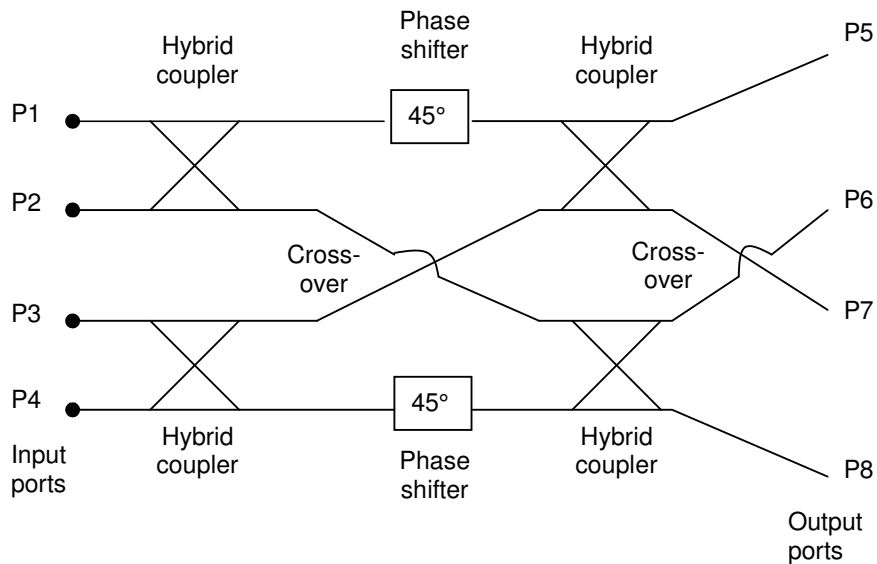


Figure 5.9: 4x4 Butler matrix topology diagram.

Table 5.3 Theoretical 4x4 Butler matrix phase difference between input and output.

	Input P1	Input P2	Input P3	Input P4
Output P5	-45	-135	-90	-180
Output P6	-90	0	-225	-135
Output P7	-135	-225	0	-90
Output P8	-180	-90	-135	-45
Phase difference between adjacent ouputs	-45	135	-135	45

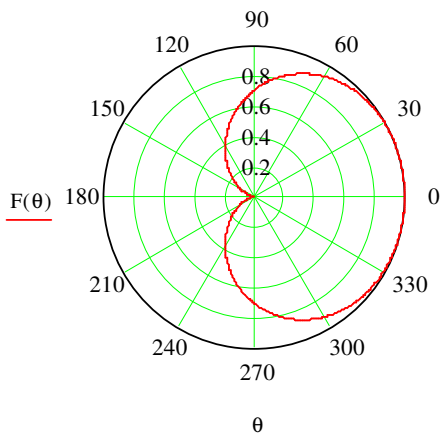
In this thesis, the principal 2x2 micromachined Butler matrix is demonstrated with three different antennas in the array. The Butler matrix is built by a single coupler without the phase shift and cross-over as in the 4x4 Butler matrix shown in Figure 5.9. The antennas have been presented in the previous chapter, which are the patch antenna, the H-plane horn antenna and the ridge waveguide slot antenna. The array factor will be discussed in the next section before presentation of the Butler matrix with the antenna array.

5.4.1 Array Factor

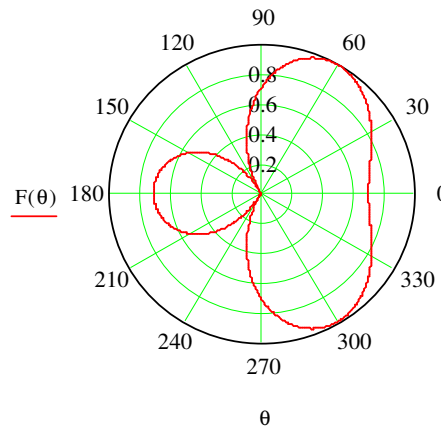
The antenna array beam pattern can be estimated theoretically by multiplying an array factor ($F(\theta)$) with the single element field pattern ($E(\theta)$). The array factor can be calculated by [8]

$$F(\theta) = \left| \sum_{n=0}^{N-1} (a_n \cdot e^{j\phi_n} \cdot e^{jkd_1 \cos(\theta)}) \right|, \quad (5.10)$$

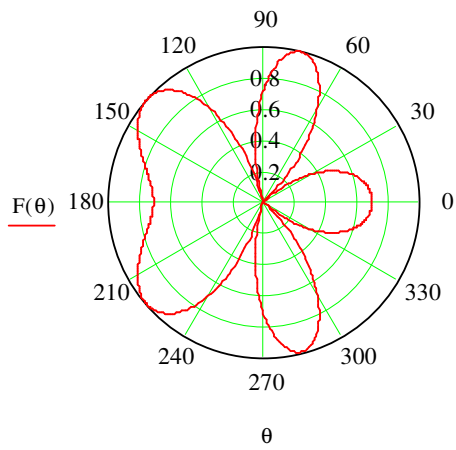
where N is the array elements and k is the wave-number given by $2\pi/\lambda$. a_n is the input power of n^{th} element while d_1 is the spacing between adjacent elements. For the hybrid quadrature branch line coupler used for the Butler matrix here, a_n is 0.5 which is half of the input power. The inter element distance is normally half wavelength or less. A larger distance may contribute to multiple maxima or grating lobes. Grating lobes are the lobes or beams that have comparable peak intensities to the desired beam. They are different from side lobes which have significant lower peak intensities compared to the desired beam. The grating lobe is defined in [8] as ‘a lobe, other than the main lobe, produced by an array antenna when the inter element spacing is sufficiently large to permit the in-phase addition of radiated fields in more than one direction’. Figure 5.10 shows the array factor plot for different antenna element distances.



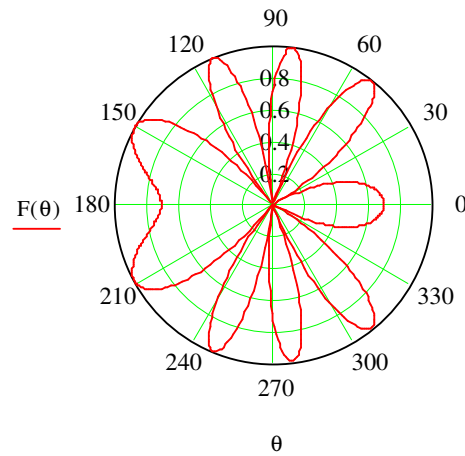
(a) Inter element spacing: 0.25λ



(b) Inter element spacing: 0.5λ



(c) Inter element spacing: λ



(d) Inter element spacing: 2λ

Figure 5.10: Array factor for different distances between 2 antenna elements.

Let us consider a field pattern for a patch antenna to demonstrate the array pattern. The field pattern for a single element patch antenna is given by [9]

$$E(\theta) = \frac{\sin\left(\frac{kW}{2}\cos(\theta)\right)}{\left(\frac{kW}{2}\right)\cos(\theta)}\sin(\theta), \quad (5.11)$$

where W is the width of the single patch element. The pattern is shown in Figure 5.11.

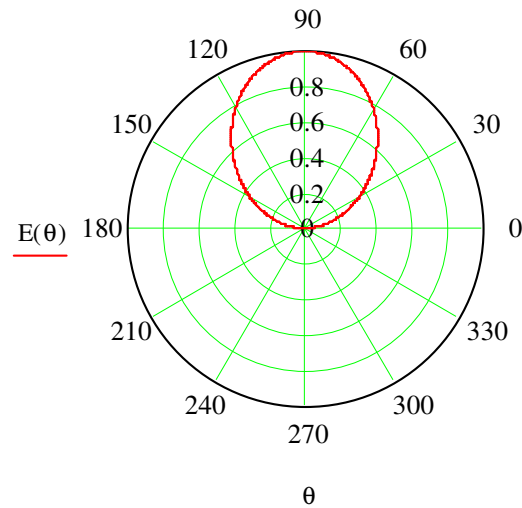


Figure 5.11: Calculated radiation patterns for single patch antenna.

The pattern for an array of two element patch antenna can be obtained by multiplying (5.10) and (5.11). The inter element distance is set to be half wavelength and the phase difference is 90° . The array factor plot is shown in Figure 5.10 (b). The field pattern of the array is plotted in Figure 5.12. The beams are formed at $\pm 16^\circ$ from the boresight.

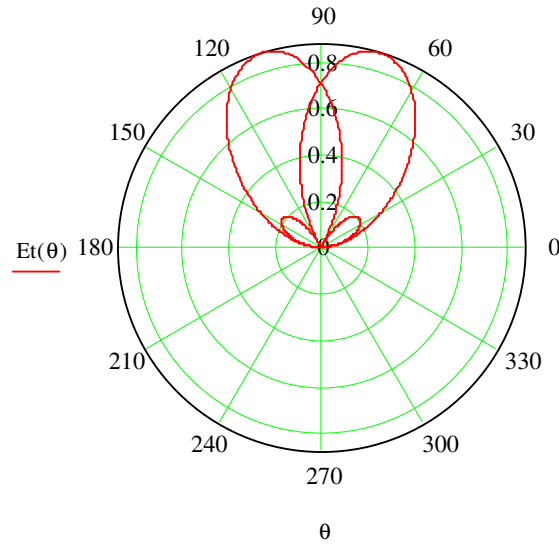


Figure 5.12: Calculated radiation patterns for 2 element patch antenna array.

5.4.2 Butler Matrix with a Patch Antenna Array

The micromachined patch antenna designed at a 63 GHz centre frequency was discussed in the previous chapter. The design is used here, but in an array of two patch elements. They are directly connected to the output ports of the coupler by a quarter wavelength transformer. The bend in the transition between the Butler matrix and the patch is placed to get a half wavelength distance between the two elements. Figure 5.13 shows the whole structure without the top layer that covers the ports and the Butler matrix to assist viewing. The overall structure size is $7.4 \text{ mm} \times 11.0 \text{ mm} \times 1.0 \text{ mm}$.

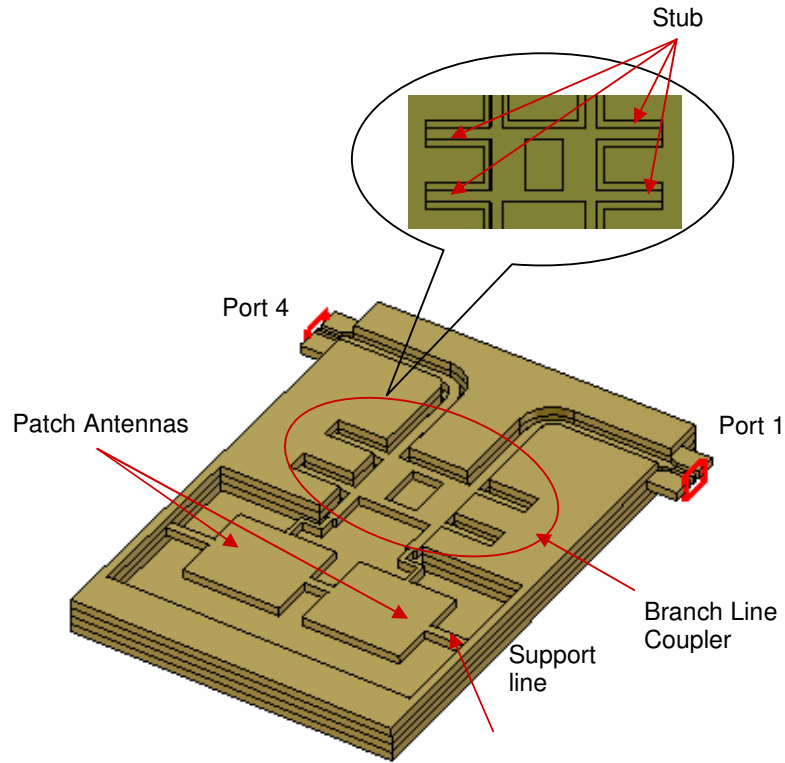


Figure 5.13: Butler matrix with a patch antenna array.

The design has been modelled in CST software. The structure is matched at the designed frequency with return loss of -23 dB and inter-port isolation of -15 dB, as shown in Figure 5.14. The simulated far-field radiation patterns with realized gain of 12 dB are depicted in Figure 5.15 with the input from port 1 and port 4. The H-plane patterns are shown in Figures 5.16 and 5.17. The quadrature phase difference between the output ports of the coupler allows the beam to be angled from the boresight. The broadside beam forms at 107° from the boresight with side lobe level of -8.9 dB when the input is on port 1. The half power

beamwidth (HPBW) of the main lobe is 36.6° . Input from port 4 led to the broadside beam at 73° from the boresight with -9.1 dB side lobe level. The beams are formed at $\pm 17^\circ$ from the centre of the patches when each of the two ports is fed individually, 1° different from the array factor calculation above.

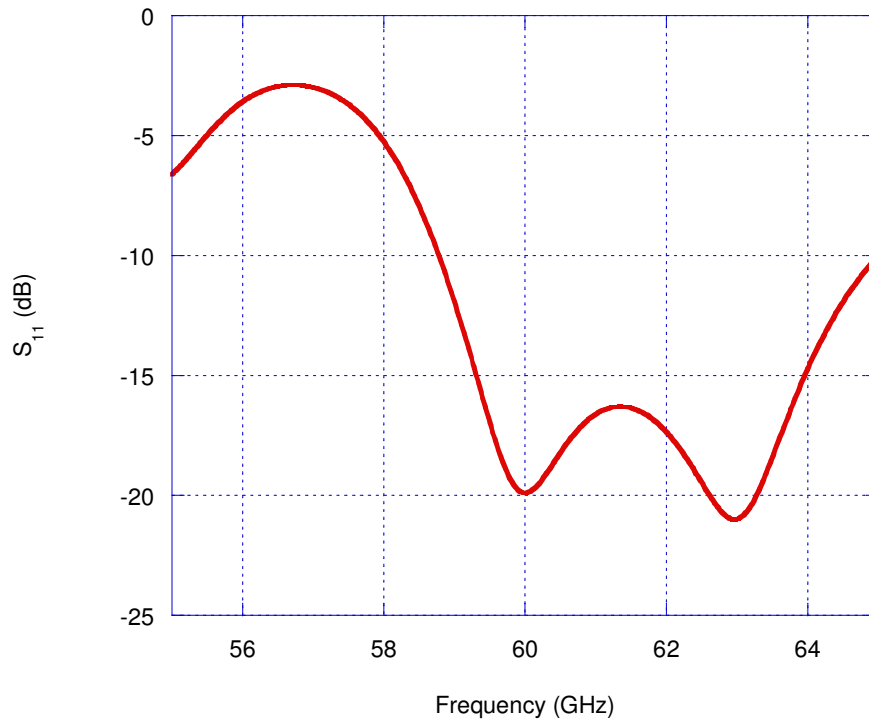
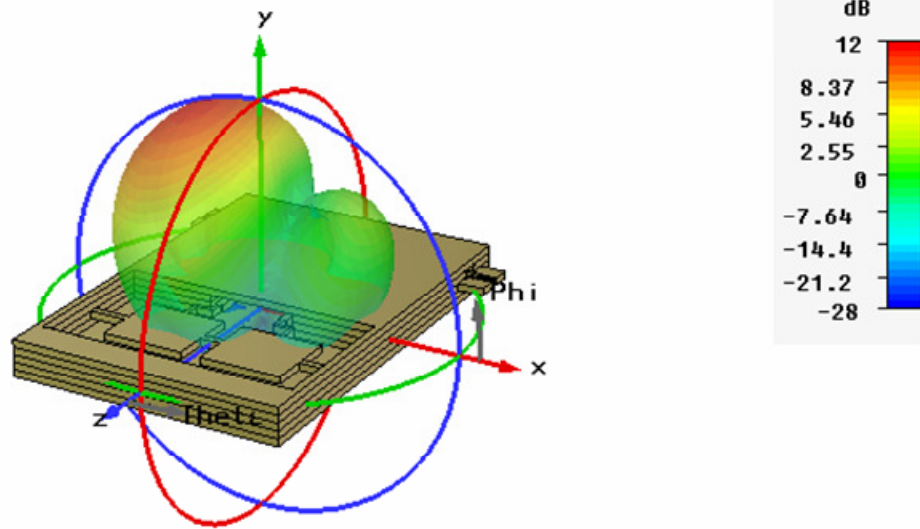
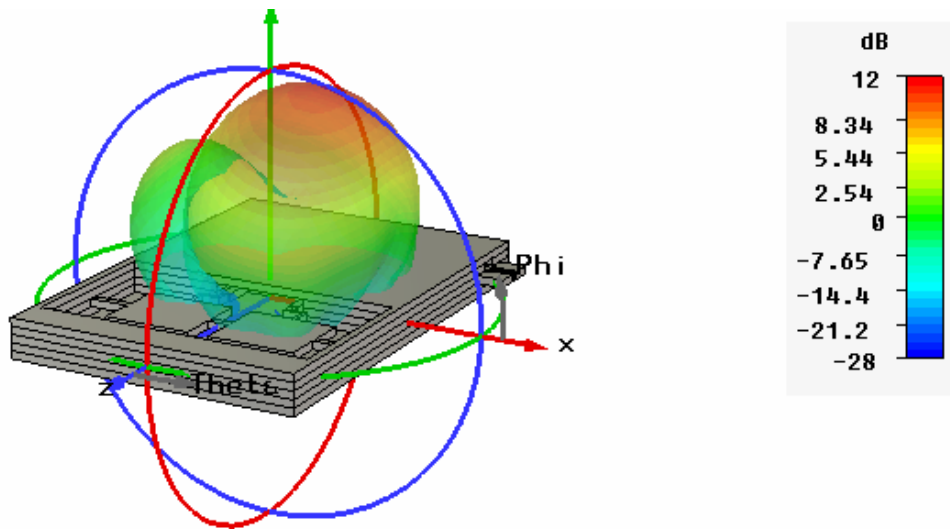


Figure 5.14: Return loss of the patch antenna array.



Input from port 1.



Input from port 4.

Figure 5.15: 3D radiation pattern of the patch antenna array.

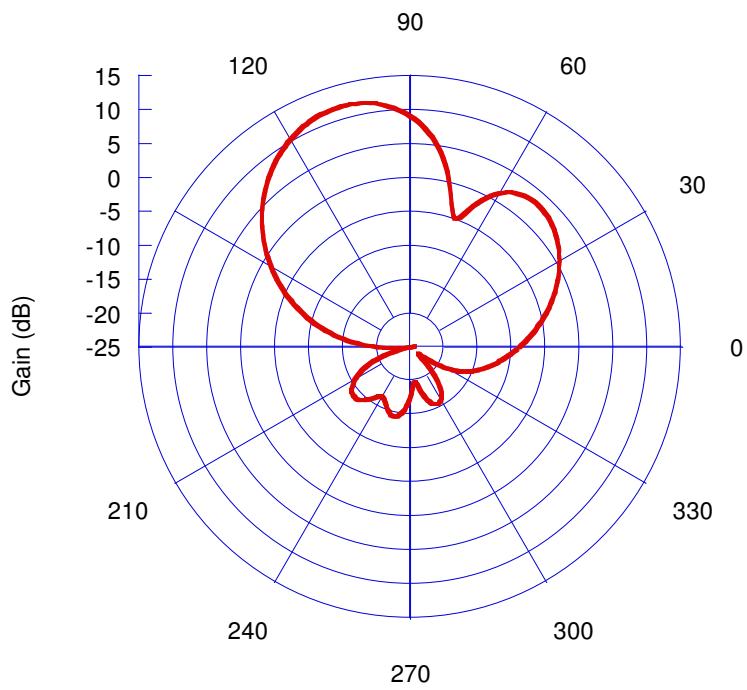


Figure 5.16: A simulated H-plane field pattern at 63 GHz with an input at port 1.

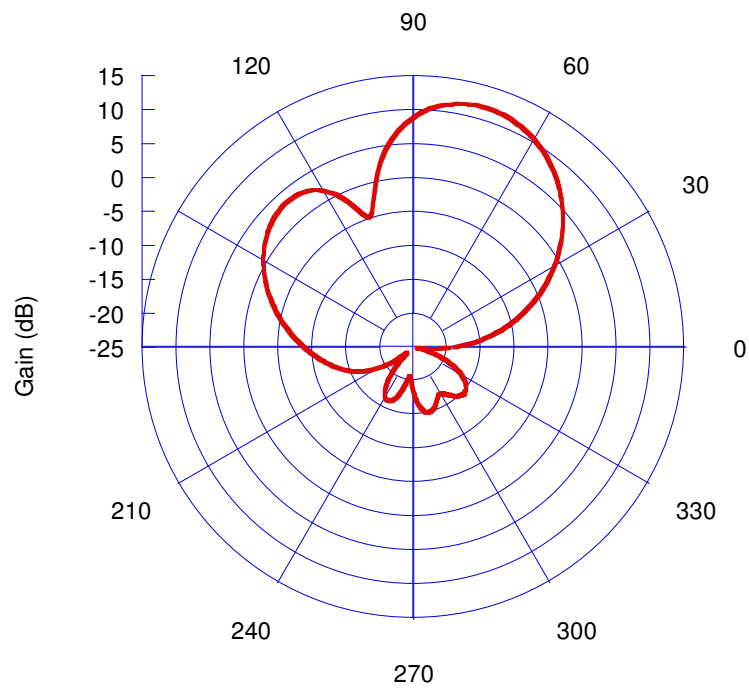


Figure 5.17: A simulated H-plane field pattern at 63 GHz with an input at port 4.

The structure has been manufactured using the thick SU-8 photoresist micromachining technique discussed in Chapter 2. Figure 5.18 shows the five layer exploded view. It consists of the inner conductors and the patch antenna as the middle layer (layer 3), sandwiched by two outer conductors layers (layers 2 and 4) and enclosed by top (layer 1) and bottom (layer 5) layers. The dimensions of layers 2, 3 and 4 are shown in Figure 5.19. All unconnected pieces at each layer are jointed by tethers that are broken off after bonding. The fabricated device has been measured using an on-wafer probe station connected to a vector network analyzer. The measurement setup is presented in Appendix A.

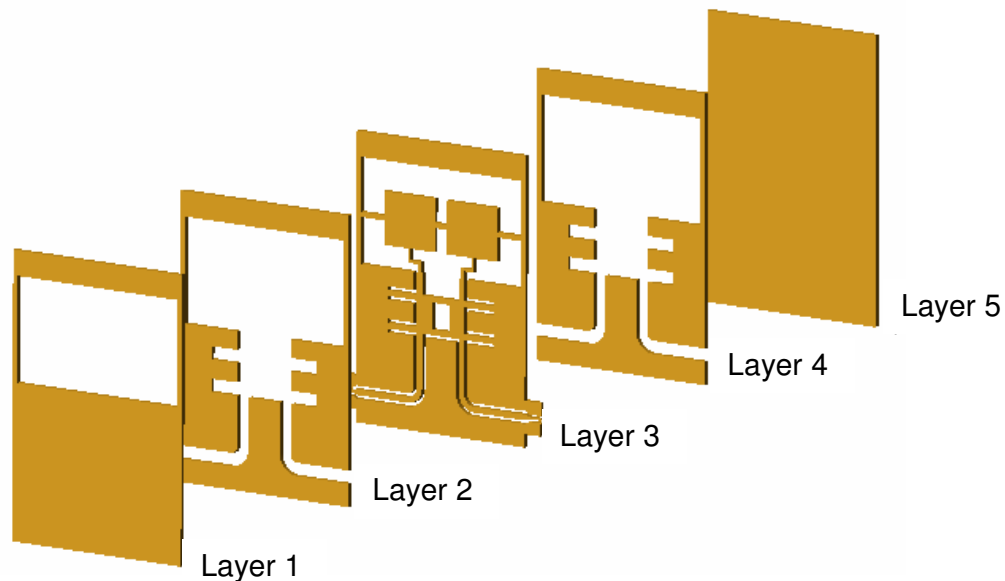


Figure 5.18: Five layer exploded view.

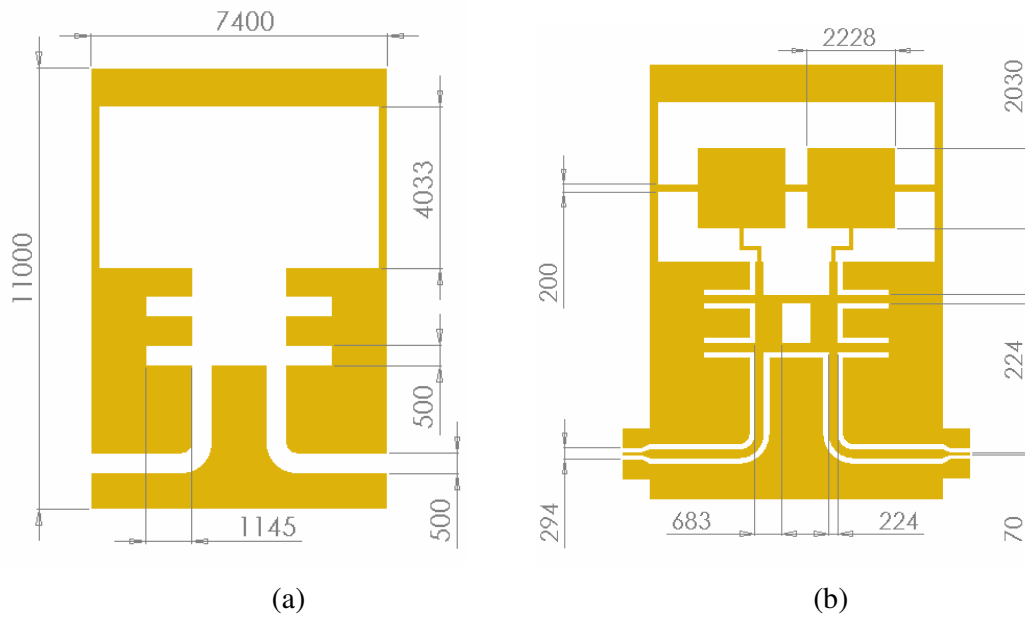


Figure 5.19: Dimensions (in μm) of (a) layers 2 and 4; and (b) layer 3 of the structure.

Figure 5.20 shows the measured and simulated return loss with the input from port 1 and port 4. A moving average, averaging every 3 adjacent data points, has been applied to the data to smooth the response for a better view. The return loss is better than -10 dB at the designed frequency. Some misalignment during fabrication may have resulted in a slightly higher return loss in the measurement response as compared with simulations. This resulted in a better isolation shown in Figure 5.21 as more power reflected back to the input port.

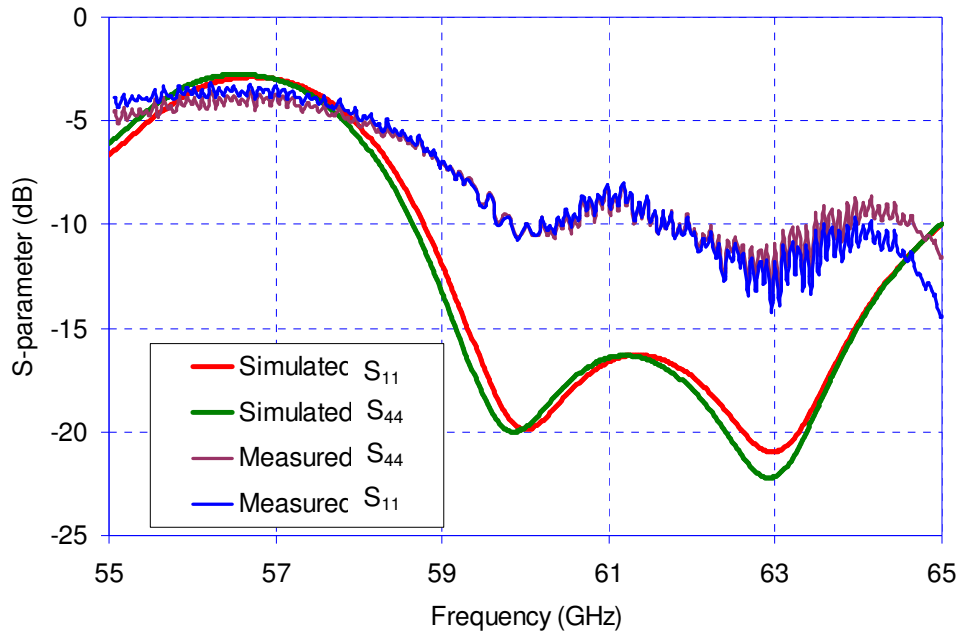


Figure 5.20: Simulated and measured return loss with input from port 1 (S_{11}) and port 4 (S_{44}).

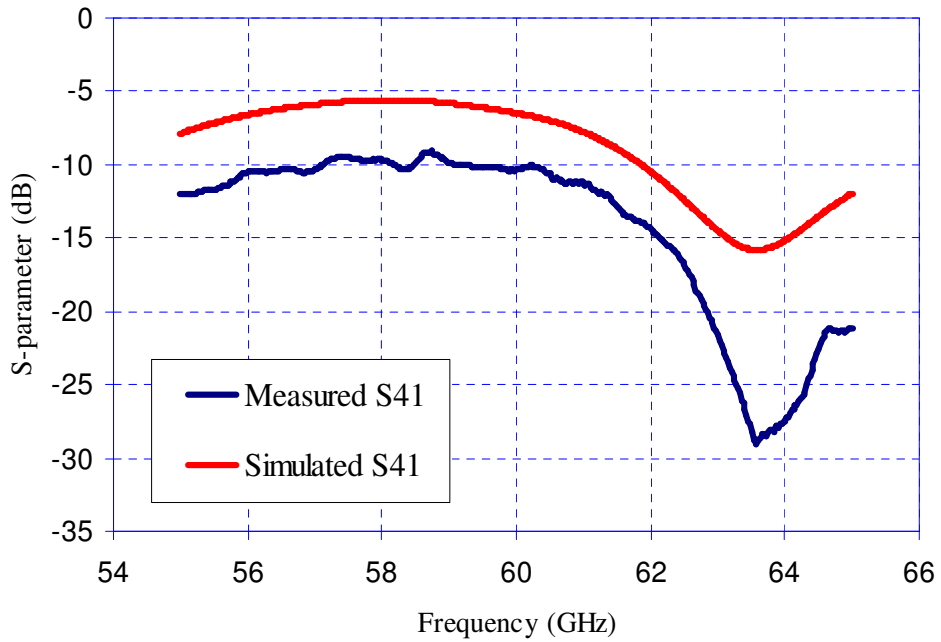


Figure 5.21: Simulated and measured inter-port isolation (S_{41}) of the patch antenna array.

The co-polar radiation pattern has been measured using a standard 20 dBi gain horn antenna as a transmitter. Due to some obstruction in the current measurement setup, it is not possible to measure below 40° and above 140°. The results are shown in Figure 5.22. The measured patterns are comparable to the simulated results, although there are more ripples due to reflections from the probe station surroundings.

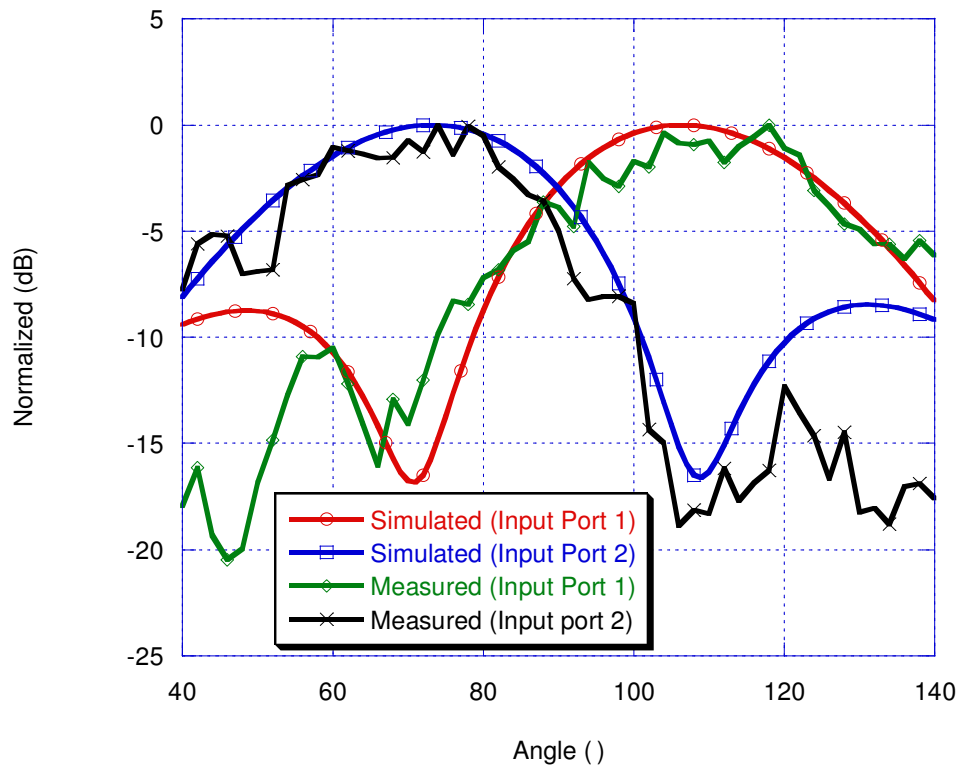


Figure 5.22: Simulated and measured H-plane radiation pattern of the patch antenna array.

5.4.3 Butler Matrix with a Horn Antenna Array

The beamforming technique using the Butler matrix discussed in the previous section is applied here, but the antenna is changed to the H-plane horn antenna array. Here, the distance between the two antennas is about $5/4$ wavelength. This is due to the horn aperture size and optimisation on the coupler and the horn interconnection using CST software. The structure without the top layer to assist viewing is shown in Figure 5.23. The horn with the rectangular coaxial line to ridge waveguide transition has been discussed in Chapter 4.

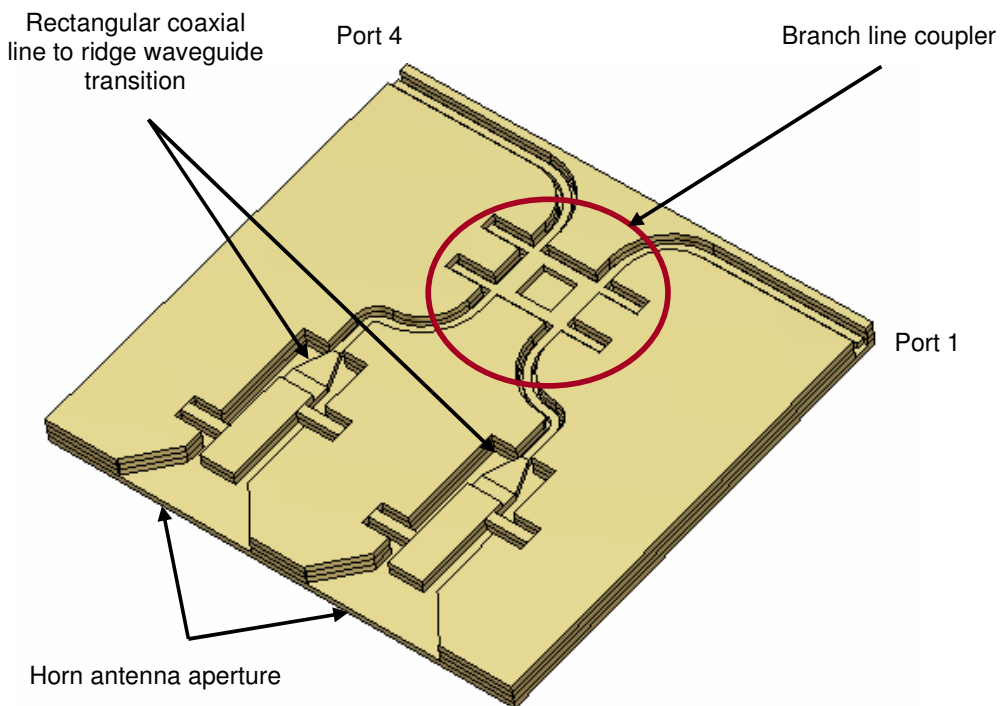


Figure 5.23: H-plane horn antenna array with Butler matrix structure without top layer.

The structure has been simulated using CST software, but not constructed. The return loss is better than -20 dB at the 63 GHz designed frequency as shown in Figure 5.24. The bandwidth is broad, which is 20.6%. The 3D radiation patterns are shown in Figure 5.25 with realised gain of 11.53 dB. The multiple lobes or high grating lobes are due to the separation distance between the two radiator elements, which is greater than a wavelength. The H-plane pattern with input from port 1 and port 4 are depicted in Figure 5.26 with the peak beam formed at $\pm 10^\circ$ from the broadside.

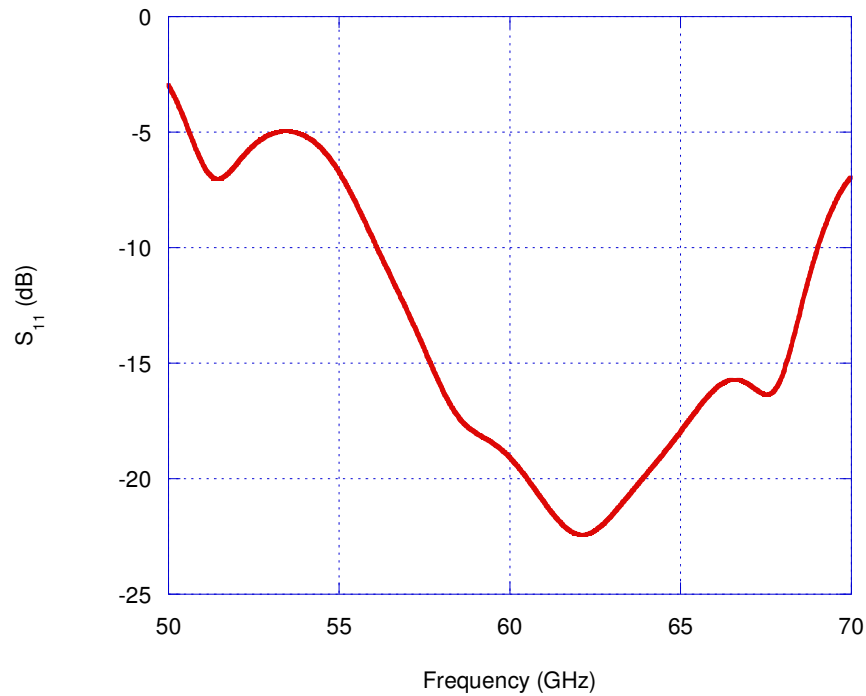
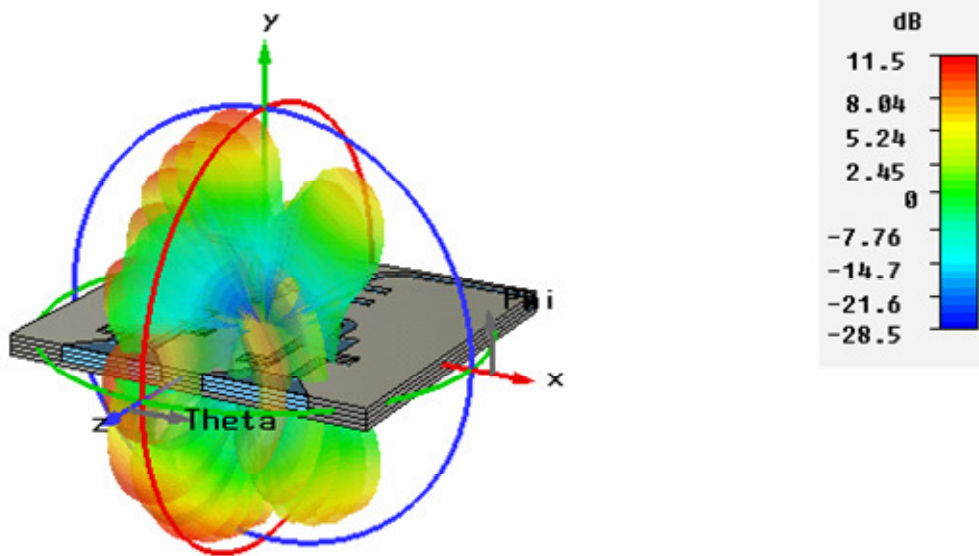
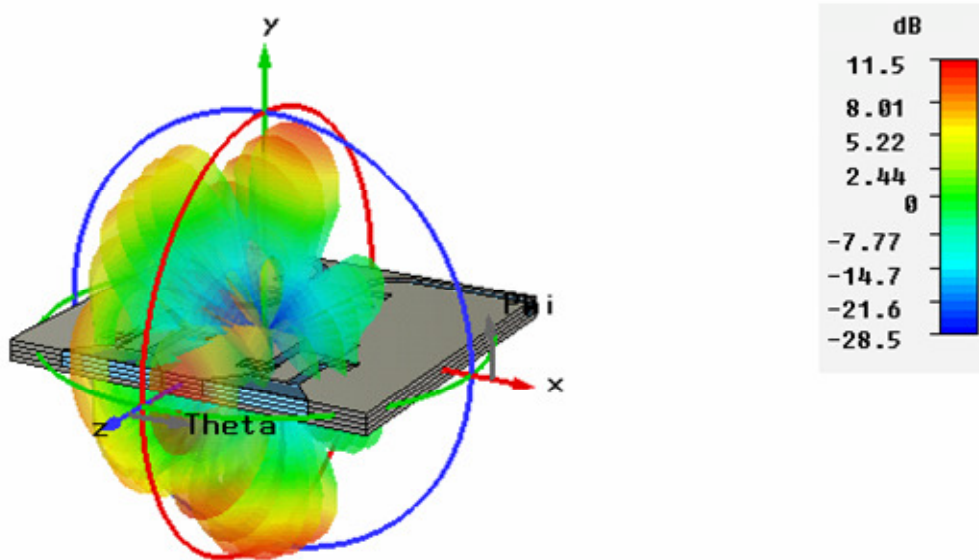


Figure 5.24: Simulated return loss of a BM with an H-plane horn antenna array.

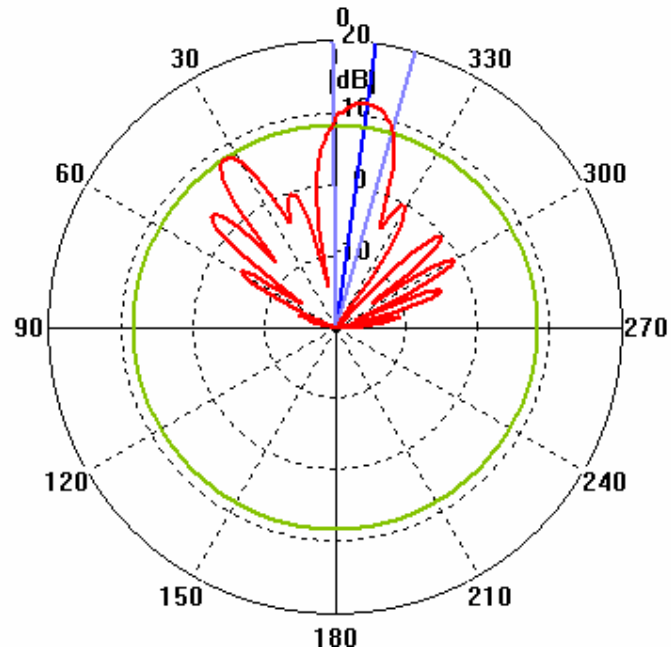


Input from port 1.

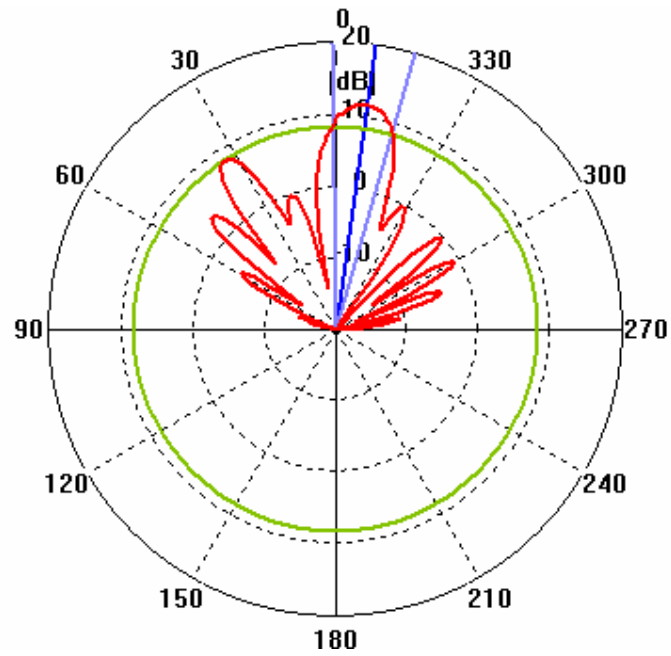


Input from port 4.

Figure 5.25: Simulated 3D radiation pattern of H-plane horn antenna array.



Input from port 1.



Input from port 4.

Figure 5.26: Simulated H-plane radiation pattern of H-plane horn antenna array.

5.4.4 Butler Matrix with a Ridge Waveguide Slot Antenna Array

In this section, an array of two ridge waveguide slot antennas attached to the branch line coupler output ports is discussed. The structure is shown in Figure 5.27. The distance between the two elements is 0.42λ , where the waveguide is designed with the transition immediately at the Butler matrix output without any bend or curve, as in the other two structures above.

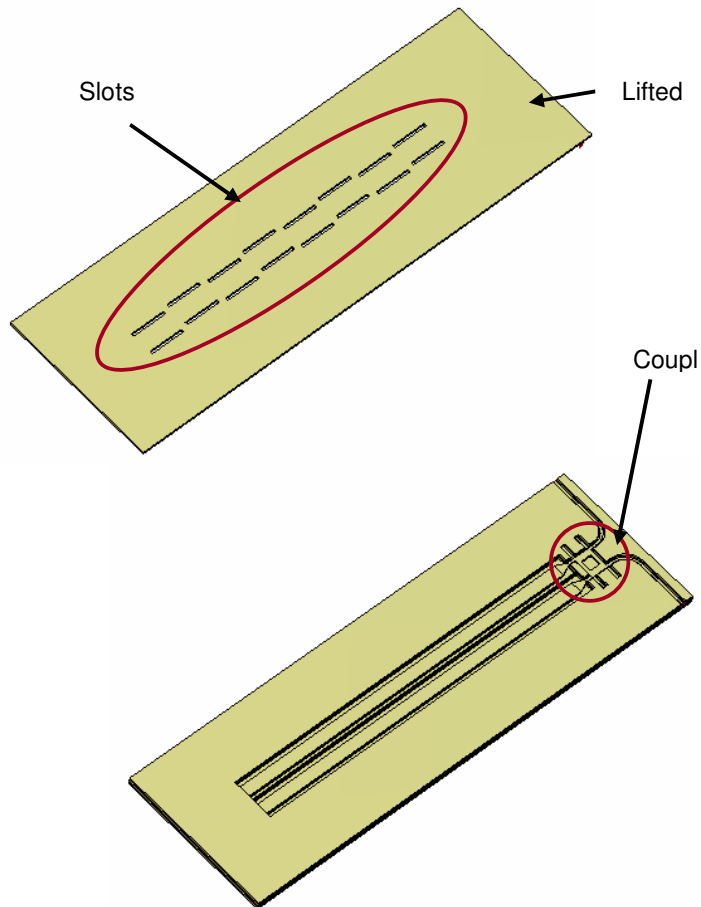


Figure 5.27: Butler matrix with a ridge waveguide slot antenna array.

The structure has been simulated using CST software, but not constructed. The return loss is better than -10 dB at the 63 GHz designed frequency as shown in Figure 5.28. The bandwidth is 12%. The 3D radiation patterns are shown in Figure 5.29 with a very high realised gain of 16.78 dB. The H-plane pattern with input from port 1 and port 4 are depicted in Figure 5.30 with the main beam formed at $\pm 49^\circ$ from the broadside.

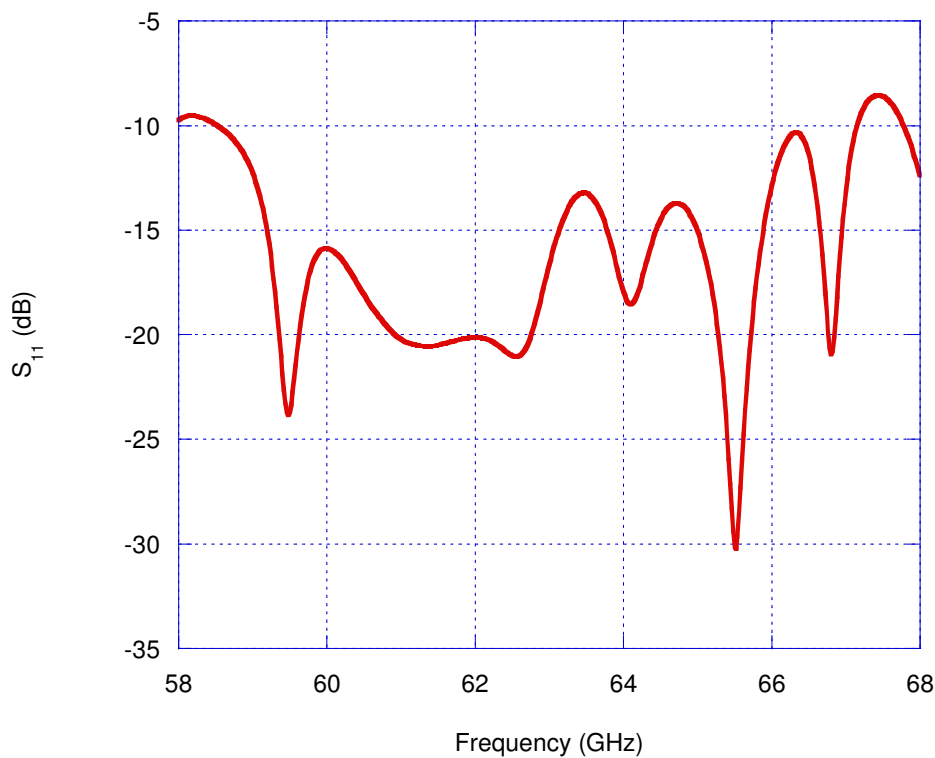
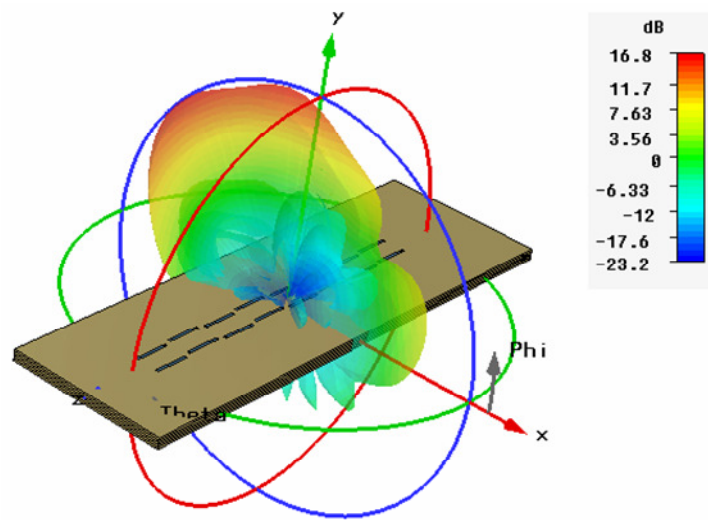
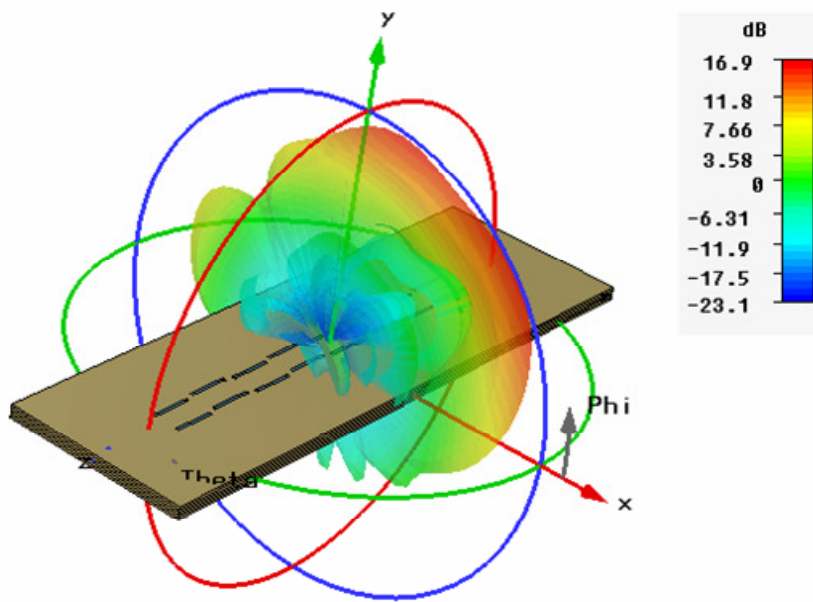


Figure 5.28: Simulated return loss of the Butler matrix with the ridge waveguide slot antenna array.

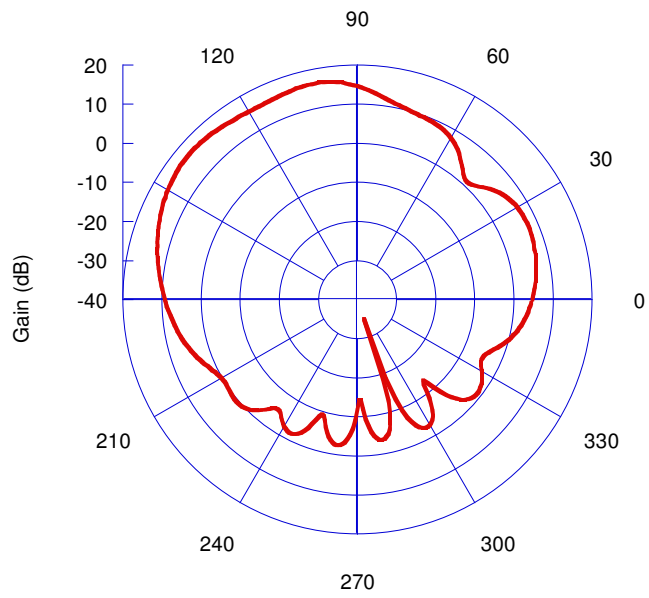


Input from port 1.

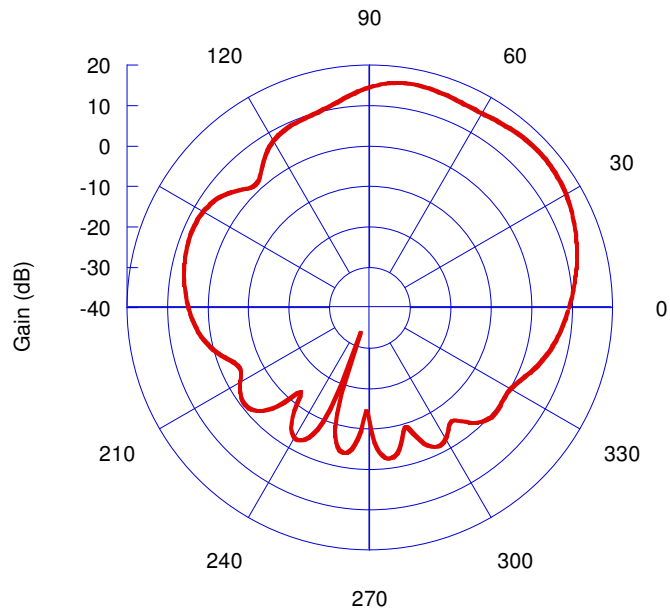


Input from port 4.

Figure 5.29: Simulated 3D radiation pattern of the ridge waveguide slot antenna array.



Input from port 1.



Input from port 4.

Figure 5.30: Simulated E-plane radiation pattern of the ridge waveguide slot antenna array.

5.5 Summary

Beamforming using a Butler matrix configuration has been presented with three different antenna arrays: a patch antenna array, an H-plane horn antenna array, and a ridge waveguide slot antenna array. The Butler matrix with patch antenna array has been demonstrated and successfully measured. However, there are losses shown by the measured S parameters that may occur due to gaps or imperfections between joined layers. The measured radiation pattern follows the simulated pattern with the beam formed at $\pm 17^\circ$. Reflections from the surroundings might cause ripples in the measured pattern. The surface current that travels to the ground may also cause these ripples.

The other two antenna arrays are discussed based on modelling simulations. Multiple maxima lobes are observed in the H-plane horn antenna array simulated radiation pattern. This occurred due to the spacing between the two antenna elements, which is about 1.5λ . The ridge waveguide slot antenna array is designed with a shorter distance between two elements, which is 0.42λ . The distance is the optimised distance between the two output ports of the Butler matrix.

The pattern obtained from the simulations and measurement above shows that the beam of the antenna array can be controlled by changing the distance between the array elements. The beam can also be directed by changing the phase difference between the elements.

References

- [1] K. Chang, *Handbook of Microwave and Optical Components* vol. 1: John Wiley & Sons, 1989.
- [2] R. S. Elliot, *An Introduction to Guided Waves and Microwave Circuits*: Prentice Hall, 1993.
- [3] D. M. Pozar, *Microwave Engineering*, Third ed.: John Wiley & Sons, 2005.
- [4] Y. Wang, M. Ke, M. J. Lancaster, and F. Huang, "Micromachined Millimeter-wave Rectangular Coaxial Branch-Line Coupler with Enhanced Bandwidth.," *IEEE Transaction on Microwave Theory and Techniques*, vol. 57, pp. 1655-1660, 2009.
- [5] R. K. Gupta, S. E. Anderson, and W. J. Getsinger, "Impedance-Transforming 3-dB 90-degrees Hybrids," *IEEE Transactions on Microwave Theory and Techniques*, vol. 35, pp. 1303-1307, 1987.
- [6] P. S. Hall and S. J. Vetterlein, "Review of radio frequency beamforming techniques for scanned and multiple beam antennas," *Microwaves, Antennas and Propagation, IEE Proceedings H*, vol. 137, pp. 293-303, 1990.
- [7] H. Moody, "The systematic design of the Butler matrix," *IEEE Transactions on Antennas and Propagation*, vol. 12, pp. 786-788, 1964.
- [8] C. A. Balanis, *Antenna Theory Analysis and Design*, 2nd ed.: John Wiley & Sons, 1997.
- [9] I. J. Bahl and P. Bhartia, *Microstrip Antennas*: Artech House Inc., 1980.

Chapter 6

Conclusions and Future Work

6.1 Conclusions

The work presented in this thesis focused on the design of micromachining structures, in particular for Butler matrix antenna beamforming for millimetre-wave applications. At microwave frequency, the Butler matrix can be built in microstrip with conventional machining. At millimetre-wavelength, the structure is shrunk in size. A precise manufacturing technology is needed. Thus, the thick SU-8 photoresist micromachining technology for coaxial cables and waveguides is used in this thesis. The advantages of this thick SU-8 photoresist micromachining technique include low cost, high aspect ratio, and nearly vertical wall. The use of coaxial cable eliminates cross-talk.

The structures are designed at 63 GHz which may be of benefit to inter-vehicle communication systems. Components involved in building the beamforming circuit here are the antennas, branch line coupler built by using rectangular coaxial lines, and the transitions

from the coaxial line to a ridge waveguide and a co-planar waveguide. Three antennas are discussed in this thesis. They are the patch antenna, the H-plane horn antenna, and the ridge waveguide slot antenna.

Four structures are manufactured to demonstrate the compatibility of the design with the thick SU-8 micromachining technique. They are (1) a back to back rectangular coaxial line to ridge waveguide transition, (2) the transition with an H-plane horn antenna, (3) the transition with a ridge waveguide slot antenna, and (4) a 2 x 2 Butler matrix with a patch antenna array which integrates all components designed in the five layer structure. All fabricated structures have been measured using an on-wafer probe station measurement setup.

The micromachined rectangular coaxial line to ridge waveguide transition has been designed with a tapered inner conductor connected to the lower part of the waveguide ridge. Higher order mode ridge waveguide stubs are used to support the ridge of the main waveguide. To the best of author's knowledge, this is the first time the concept of using the higher order mode ridge waveguide in supporting suspended lines in the thick SU-8 micromachined structure has been used. The measured S-parameters follow closely to the simulation. This demonstrates the reliability of the technology used in manufacturing the structure. Imperfections and the gaps between joined layers may results in some losses. The designed transition structure is useful in feeding horn and waveguide antennas.

The designed miromachined rectangular coaxial line to ridge waveguide has been implemented in feeding the H-plane horn antenna and the ridge waveguide slot antenna. An air-suspended patch antenna is also studied and the performance has been observed by modelling in CST software. The suspended patch is supported by a line connected the outer wall of the overall structure to a minimum voltage point at the edge of the patch.

The beam of the antennas has been steered by integrating the antenna array to a Butler matrix beamformer. The beamformer is designed by using a rectangular coaxial line branch line coupler. All suspended lines in the coupler are supported by quarter wavelength matching stubs. The coupler is designed with 3-dB coupling and quadrature phase. The quadrature phase between the outputs allows the beam to form at different angles. This has been demonstrated in the measurement of the manufactured patch antenna array with the Butler matrix structure. The beams are formed at $\pm 17^\circ$ as expected from the numerical simulation.

In summary, this thesis is about designing millimetre-wave components and circuit manufactured using the five layer metal coated of thick SU-8 photoresist micromachining technique. The measured performances on the manufactured structures demonstrate the compatibility of the designed structures with the mentioned processing technique.

6.2 Future Work

6.2.1 Studies on Fabrication Errors

More research can be done on the thick photoresist micromachining process to improve the performance of the manufactured structures. For instance, studies on the use of adhesive materials and the bonding process may solve the problem of imperfect wall, and the curvature of the layers once released. Studies on the ideal temperature in the processing steps may also help in improving the performance of the fabricated structure.

6.2.2 Broadband Butler Matrix and Wideband Antenna Array

In the future, smart transportation systems with anti collision and automated cruise radar at 77 GHz, and inter-vehicle communication at 63 GHz will benefit from having a broadband BM with wideband antenna array that covers both frequencies in one system. This will reduce power consumption and consequently minimise the cost.

6.2.3 Antenna Measurement at Millimetre-wave Frequencies

Using On-wafer Probe Station

An accurate antenna measurement is important to determine the performance of the real antenna. Theoretical prediction can be calculated but may be difficult for complex antenna here some idealisations or assumptions have to be made. Improvement of the measurement setup and error correction including the reflection effect due to the equipment and surrounding environment may help in achieving an accurate radiation and gain of the antenna.

6.2.4 Front end design and real application implementation.

Further studies can be applied to the front end design of the antenna beamforming circuit for smart transportation systems such as implementing signal processing to process informative signals, or by implementing switching structures to control the beam angle and the

beamwidth for a vehicle moving on the road. The implementation of micromachined beamforming components and circuits in inter vehicle communications in transportation systems will demonstrate the compatibility of the structure in real applications.

APPENDIX A

On Wafer Measurement Setup

All measurements in this thesis are conducted at the Emerging Device Technology (EDT) laboratory, The University of Birmingham. The measurements are done using an on-wafer Cascade Summit 9000 probe station connected to an Agilent Technologies E8361A (10MHz-67GHz) network analyser (PNA), depicted in Figure A1. A pair of 76 GHz ground-signal-ground-ground-signal-ground (GSG GSG) Picoprobes® are used. The probe is shown in Figure A2 and A3.

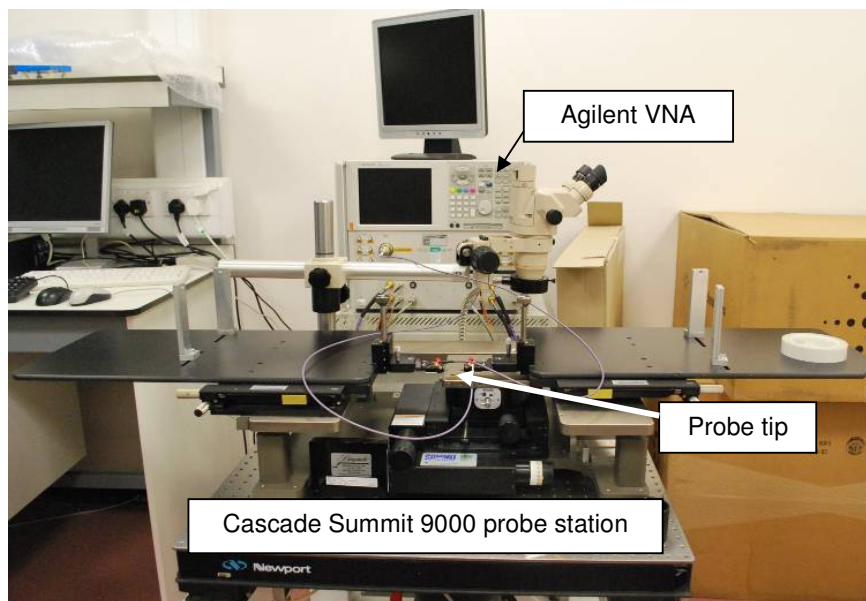


Figure A1: The probe station connected to the VNA.

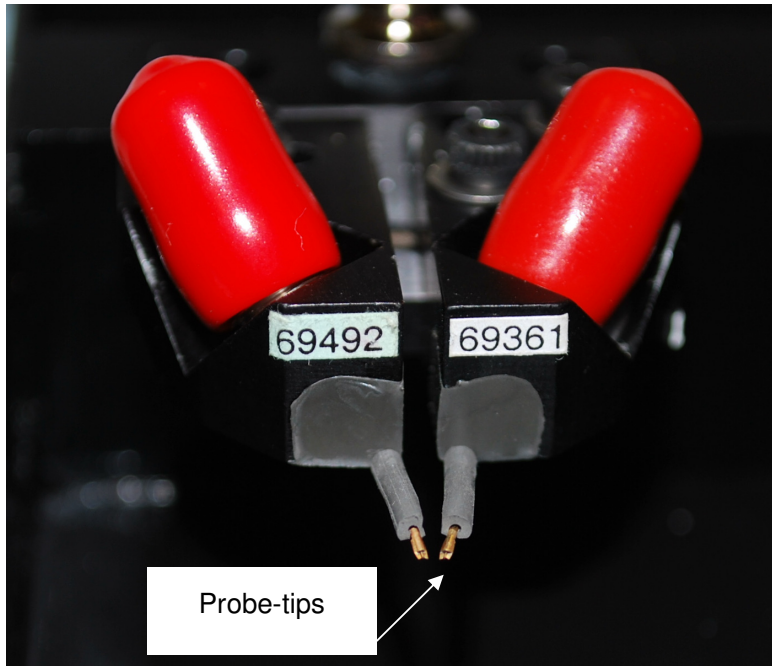


Figure A2: 76 GHz GSG Picoprobe®

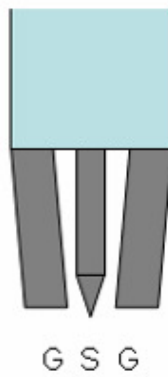


Figure A3: GSG Picoprobe® probe tips.

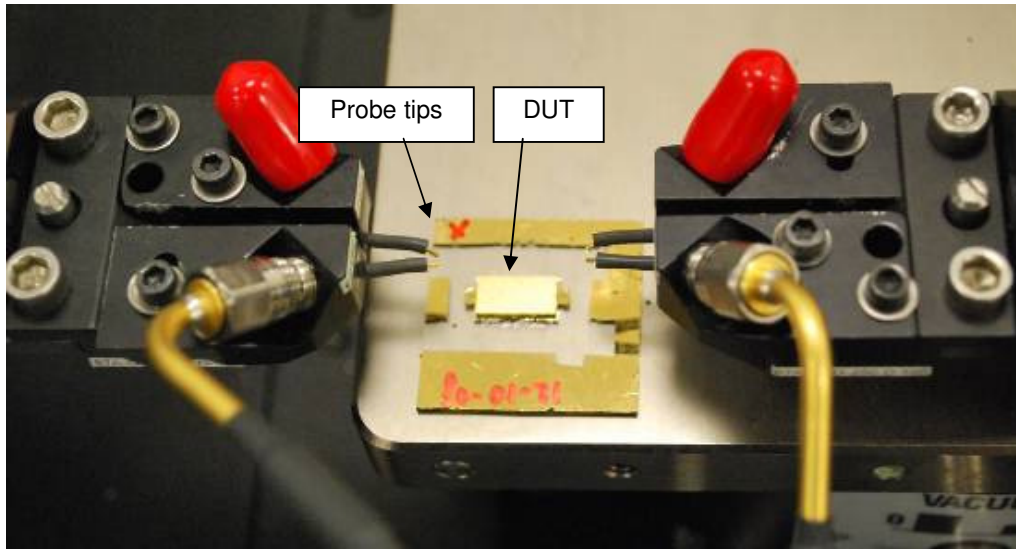
A calibration is performed before measuring the device under test (DUT). This is to calibrate out the unavoidable errors and losses in the microwave network analyser, cables, and the probe for on-wafer measurement. However, the accuracy of the calibration is limited by the accuracy of the standard used and care is exercised in doing the calibration. There are several calibration techniques available. Short-open-load-thru (SOLT) standards calculate the 12-term error model, while the thru-reflect-line (TRL) and line-reflect-line (LRL) are measured to characterize the 8-term error model. A line-reflect-reflect-match (LRRM) requires a 50Ω load, a thru and a reflect measurement, using a calibration kit or a standard provided by the manufacturer. Unlike the line-reflect-match (LRM) calibration technique, the load in LRRM is only measured at one of the two ports. Thus, discrepancies in the measured load impedance at both ports can be avoided¹. The LRRM technique is suitable for millimetre wave calibrations as the inconsistencies are negligible, thus the accurate modelling can be avoided. The LRRM is used in this work for two-port calibration, while SOL is carried out for one port calibration.

A.1 Two Ports Transmission Line Measurement

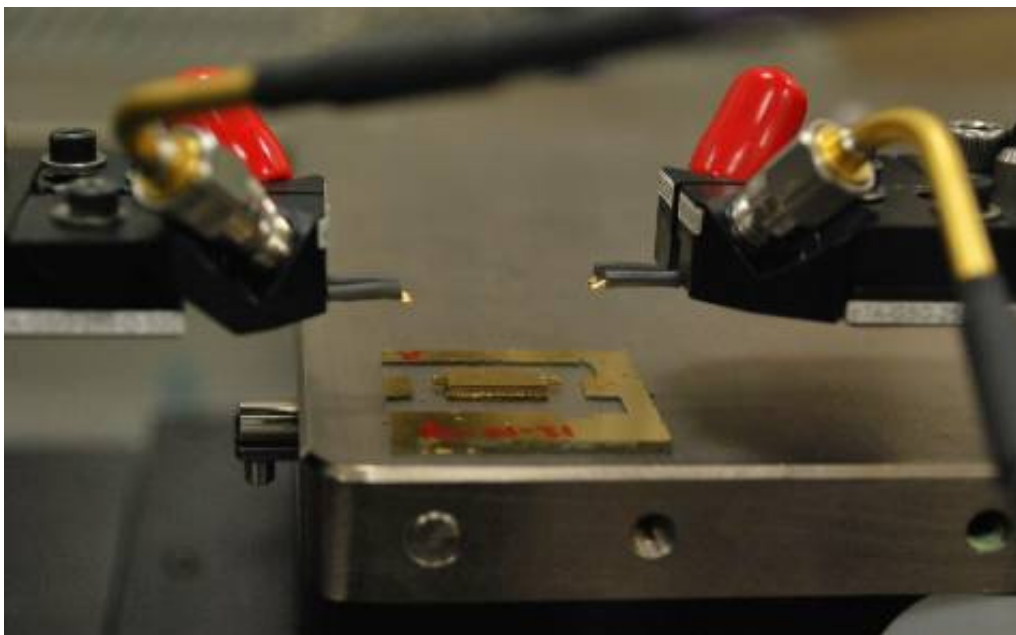
The setup is shown in Figure A1. Two standard coaxial cables are used to connect the probes to the PNA. Figure A4 shows the position of the probes and the DUT on the metal base before a contact is made. The probes are properly placed and positioned to make a contact between the tips and the co-planar line ports of the DUT. As the probe is lowered, the ground tips will contact the circuit first. A small over travel is needed to get a good contact. A further lowering of the probe will make the ground flex and then the signal tip

¹ A. Davidson, K. Jones, and E. Strid. *LRM and LRRM calibrations with automatic determination of load inductance*, ARFTG Conf., pages 29–30, Monterey, USA, Nov. 1990

will make contact. Once contact is made, the measurement begins and the PNA gives the S-parameter plot calculated with errors corrected from the calibration process.



Top view



Side view

Figure A4 Probes and DUT position.

A.2 Antenna Measurement

The return loss is measured to ensure a good match and that the signal is radiated instead of reflected back to the input port. A one-port calibration is carried out before the measurement. The same procedure presented in A.1 is performed.

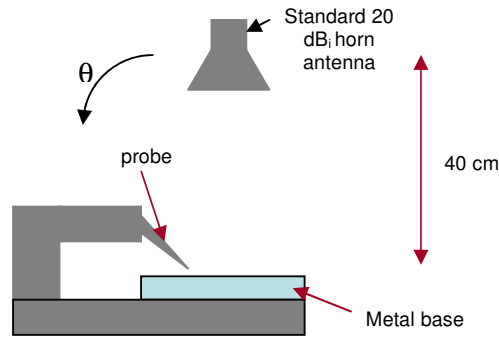


Figure A5: Side view of radiation pattern measurement setup 1.

The radiation pattern of the ridge waveguide slot antenna and the patch antenna array has been measured in the far field region by using the setup illustrated in Figure A5 and shown in Figure A6. A standard 20 dB_i horn antenna is aligned 40 cm above the antenna under test (AUT), which is placed on the metal base. For far field measurement, the distance between the two antennas is calculated based on $r > \frac{2D^2}{\lambda}$, where r is the distance, D is the largest dimension of the antenna and λ is the free space wavelength². Insufficient distance can introduce phase error, which consequently increases the side lobes level and lowers the gain. In addition, the null may be filled.

² C. A. Balanis, *Antenna Theory Analysis and Design*, 2nd ed.: John Wiley & Sons, 1997

The pattern is plotted by measuring the insertion loss; S_{21} for every 2° angle. The standard gain horn is moved along the foam rack shown in Figure A6. Then, the data acquired at the designed frequency is analysed and plotted against the angle.

The absorbing material (Emerson & Cumings's CV-3 unpainted RAM material) is used to partially shield the area as shown in Figures A7 and A8. This is to minimise the possible error due to surrounding reflections. Reflections from the surroundings introduce interference between directed and reflected waves and consequently produce field variations in amplitude and phase ripples³. There may even be a null in the measured pattern.

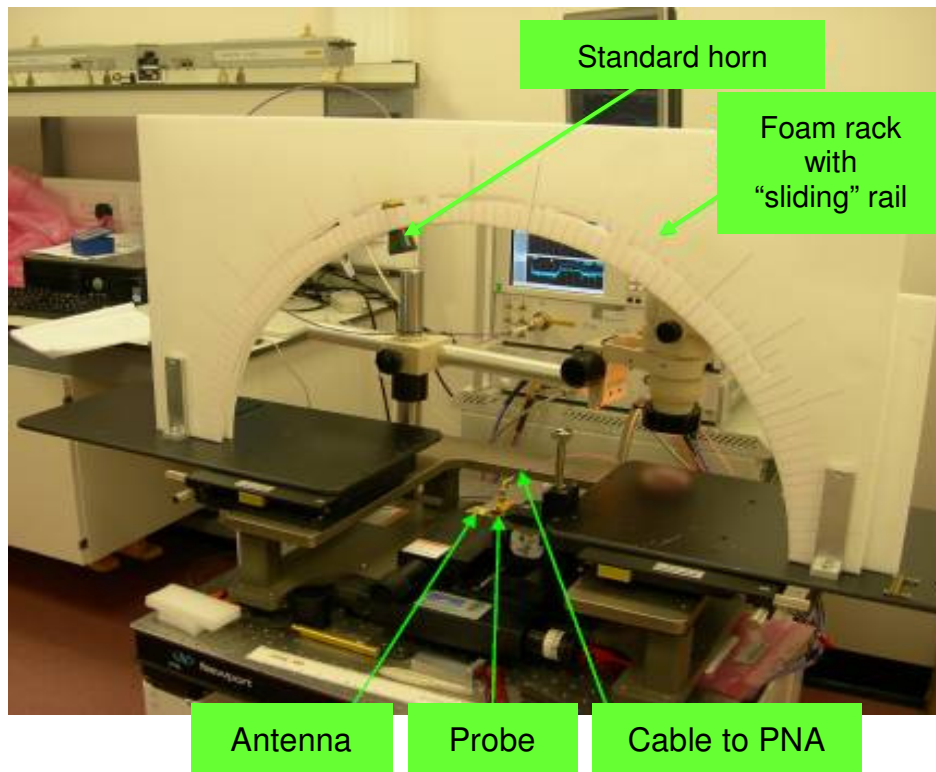


Figure A6: Initial setup without shielding.

³ J. D. Kraus, R. J. Marhefka. *Antennas for All Applications, 3rd ed.*: Mc-Graw Hill.



Figure A7: Partially shielded.

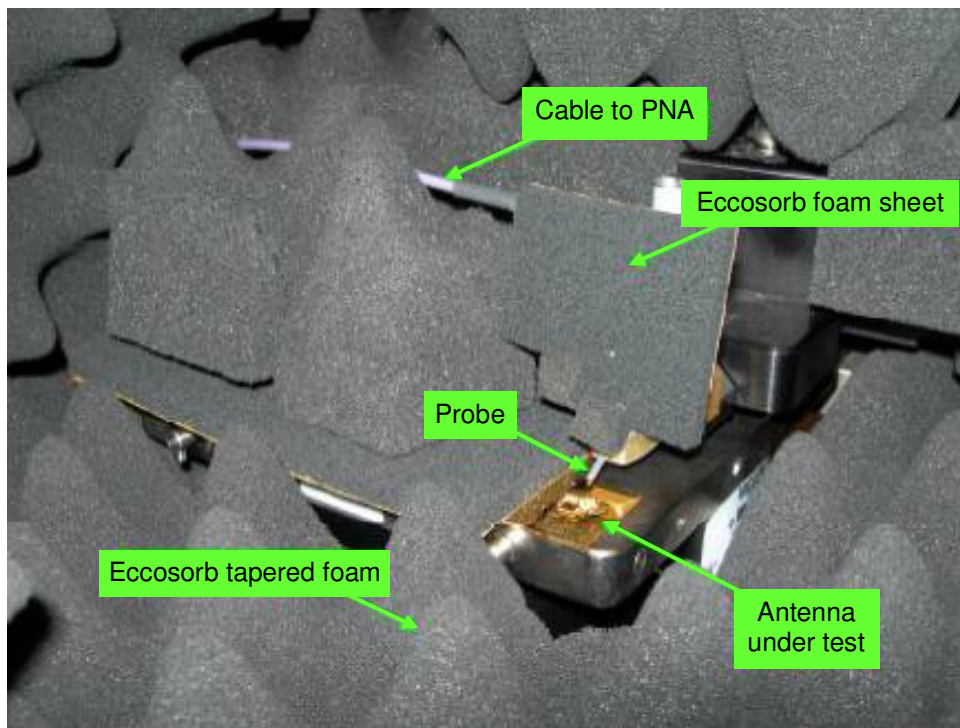


Figure A8: Localised view.

For the H-plane horn antenna, a different setup is made to measure the radiation pattern. It is illustrated in Figure A9. The measurement procedure is the same as above. Here the standard gain horn is aligned in the H-plane at 15 cm from the DUT.

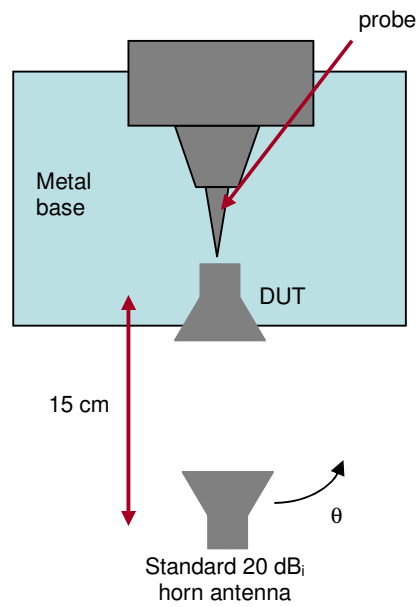


Figure A9: Top view of radiation pattern measurement setup 2 (for horn antenna).

APPENDIX B

Publication List

1. N. A. Murad, M. J. Lancaster, P. Gardner, M. L. Ke, and Y. Wang, "Micromachined H-plane horn antenna manufactured using thick SU-8 photoresist," *Electronics Letters*, vol. 46, pp. 743-745
2. N. A. Murad, M. J. Lancaster, Y. Wang, and M. Ke, "Micromachined Rectangular Coaxial Line to Ridge Waveguide Transition," in 10th Annual Wireless and Microwave Technology Conference Florida, U. S., 2009, pp. 1-5.
3. N. A. Murad, M. J. Lancaster, "Micromachined Microwave Circuits", The Graduate School Poster Conference, The University of Birmingham, June 2009.
4. N. A. Murad, M. J. Lancaster, Yi Wang, M. L. Ke. "Micromachined Millimeter-wave Butler Matrix with a Patch Antenna Array" Mediterranean Microwave Symposium 2009 (MMS2009) Tangiers, Morocco, 15-17 November 2009.
5. Yi Wang, M Ke, N Murad, T Skaik, X Shang, F Huang, M Lancaster, "Micromachined microwave circuits", poster presentation in the 2nd UK/Europe-China Workshop on Millimetre Waves and Terahertz Technologies, Rutherford Appleton Laboratory, Oxford, UK, 19th-21st October, 2009

APPENDIX C

Publications

Murad, N.A.; Lancaster, M.J.; Yi Wang; Ke, M.L.; , "Micromachined rectangular coaxial line to ridge waveguide transition," *IEEE 10th Annual Wireless and Microwave Technology Conference, 2009*, pp.1-5.

doi: 10.1109/WAMICON.2009.5207269

Micromachined Rectangular Coaxial Line to Ridge Waveguide Transition

N. A. Murad, M. J. Lancaster, Yi Wang, M.L. Ke

The University of Birmingham, Edgbaston, Birmingham, B15 2TT, UK
nam623@bham.ac.uk, m.j.lancaster@bham.ac.uk, y.wang.6@bham.ac.uk,
m.l.ke@bham.ac.uk

Abstract

This paper discusses a new micromachined rectangular coaxial line to ridge waveguide transition operating in the frequency range from 60 to 90 GHz. The micromachining techniques are used to provide accurate device dimensions for millimeter wave distributed circuits. A 50 Ω coaxial line output is coupled to a relatively high impedance ridge waveguide. A balun (balanced to un-balanced) concept is considered in order to transform TEM mode in the coaxial line to TE mode in the waveguide [4]. The design has been simulated using CST Microwave Studio 3D simulator. The structure is constructed by bonding five layers of gold coated photoresist (SU-8) each 200 microns thick. The experimental result shows a good wideband response with return loss below -19dB between 60 GHz to 90 GHz. The measurements show a 1 dB insertion loss and the S parameter response giving a good agreement with the simulation result.

1. Introduction

Traditional ways of fabricating radio frequency devices may involve milling and drilling metal to form 3-D structures. The process needs high precision and may not be suitable when the wavelength is small. Micromachining techniques are very useful when fabricating compact devices [1]–[3], and the technique is practical for devices at millimeter and sub-millimeter wave frequencies. When two dissimilar guiding structures meet, the transition must be designed properly to make sure the signal can be transferred with minimum losses. This paper discusses a coaxial to waveguide transition.

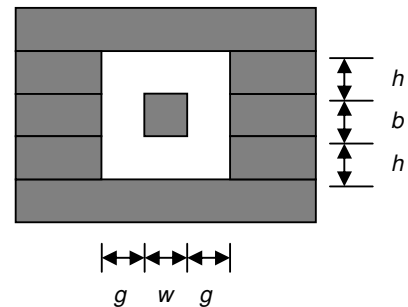
A balun concept is considered helping to alter the TEM mode of the coaxial cable to the TE mode of the ridge waveguide Boyd had patented a coaxial to ridged waveguide transition designed using a parallel plate line [4]. The 1960's design used a

parallel plate line as a transition to couple coaxial output from travelling wave tube to a double ridged waveguide. Few other coaxial to ridged waveguide transitions have been reported [5],[6]. The design here is implemented in such a way as to accomplish a structure made of five micromachined layers. The transition section is designed from an expansion of the rectangular coaxial inner conductor to join the single ridge, instead of a double ridge waveguide. The suspended lines are innovatively supported by stubs which have a cut-off frequency higher than the main waveguide.

2. Rectangular Coaxial Line

A coaxial line has the advantage that the signal is shielded by the outer conductor. Therefore, coupling to the adjacent component can be avoided. In many applications, circular coaxial cable is commonly used. However, in this work, a rectangular cross-section shape is chosen as it is easier to realise using the proposed layered micromachining method [7]. The cross-section of an ideal rectangular coaxial line is shown in Figure 1, depicting the five layers used in the construction.

Figure 1. Cross-section of an ideal air-



The rectangular inner conductor can be placed symmetrically or asymmetrically inside the hollow of the rectangular outer conductor. Discussions in this paper only consider a concentric case. The

characteristic impedance can be approximately calculated by [8]

$$Z = \frac{376.62}{2\left(\frac{b}{g} + \frac{w}{h}\right) + 4\left(\frac{C1+C2}{\epsilon}\right)} \quad (1)$$

where b , g , w and h are given in Figure 1, in this case ϵ is the free space permittivity, and $C1$ and $C2$ are the fringing capacitance produced by flux disturbance along vertical and horizontal side, respectively. They can be calculated by [8]

$$C1 = \frac{\epsilon}{\pi} \left[\ln \frac{g^2 + h^2}{4h^2} + 2\left(\frac{h}{g}\right) \arctan \frac{g}{h} \right] \quad (2)$$

$$C2 = \frac{\epsilon}{\pi} \left[\ln \frac{g^2 + h^2}{4g^2} + 2\left(\frac{g}{h}\right) \arctan \frac{h}{g} \right] \quad (3)$$

3. Ridge Waveguide

Ridge waveguide has two advantages when used in this context, the first being that it has an enhanced bandwidth over conventional waveguide, the second is that it is smaller in cross-section area. The latter is important for the case of micromachined microwave circuits, as the layer thicknesses are practically limited to around 1mm. Using this transition, we are able to convert our previous reported coaxial structures [7] to ridge waveguide, and then eventually to a horn antenna after possible further signal processing in the ridge waveguide. Only the transition is reported here.

Figure 2 shows a single and double ridge waveguide cross section. The single cross section is the one used in this paper. The layers making up the ridge waveguide are also depicted in the picture.

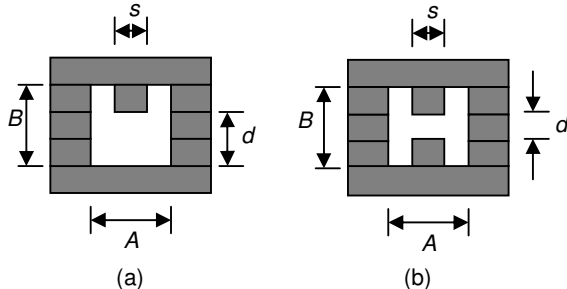


Figure 2. Ridge waveguide cross-sections. (a) Single ridged. (b) Double ridged.

A rectangular or ridge waveguide can propagate TE or TM modes, but not TEM modes. For

simplicity, this paper only considers single TE dominant propagation mode in which the ridge waveguide operates.

The dominant mode cut-off wavelength of single ridge waveguide can be calculated by using a closed form approximation [9]–[11]

$$\frac{A}{\lambda_c} = \frac{A}{2(A-s)} \left[1 + \frac{4}{\pi} \left(1 + 0.2 \sqrt{\frac{2B}{A-s}} \right) \left(\frac{2B}{A-s} \right) \right]^{\frac{1}{2}} \left[\ln \cos ec \left(\frac{\pi d}{2B} \right) + \left(2.45 + 0.2 \frac{s}{A} \right) \left(\frac{sB}{d(A-s)} \right) \right] \quad (4)$$

where A , B , d and s are given in Figure 2, and λ_c is the cut-off wavelength.

4. Design

The design is divided into three main sections, these are: (i) the coaxial line, (ii) the transition and (iii) the ridged waveguide. The design is shown in Figure 3. Section (i) is just a coaxial line of 1.07 mm long. The cross section of which is shown in Figure 3(a). Section (ii) is the inner conductor of the coaxial line, tapered and extended before shorted to the outer wall inside the waveguide as it combined with the ridge. It is quarter wavelength long. The cross section is shown in Figure 3(b). Section (iii) is the ridge waveguide. The cross-section is shown in Figure 3(c). The coaxial line only connects with half of the cross section of the ridge and is therefore shorted at the end of the quarter wavelength transition section.

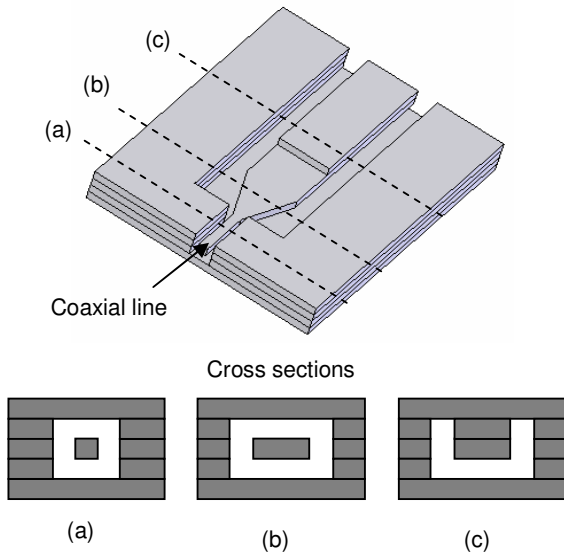


Figure 3. Transition section with lid removed. Cross-sections; (a) section (i), the coaxial line, (b) section (ii), the transition, (c) section (iii), the ridge waveguide.

For measurement purposes, two circuits have been made back-to-back. In addition, each of the coaxial ports has been transitioned to a coplanar line, so that a probe station can be used. This is shown in Figure 4.

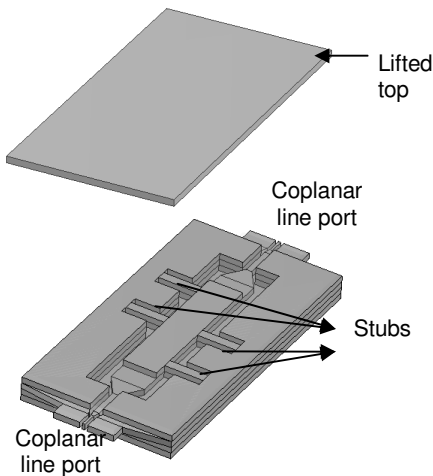


Figure 4. Back to back coaxial line to ridge waveguide transition circuit.

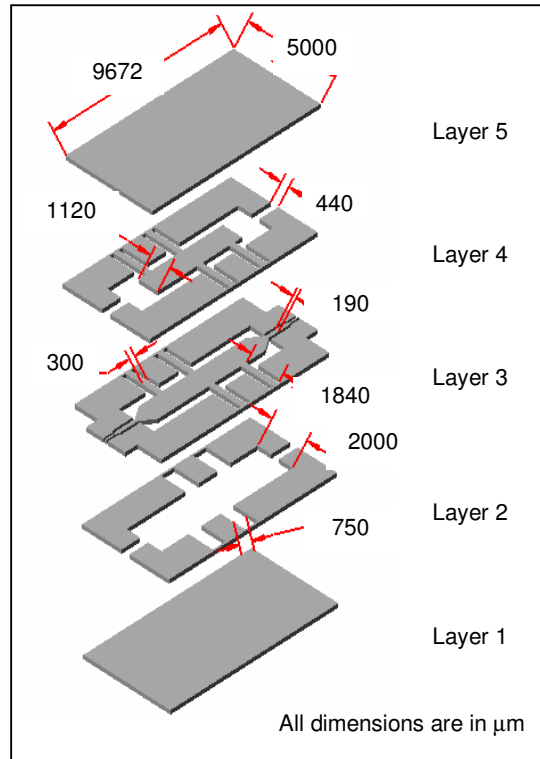


Figure 5. Layers layout.

The structure is assembled by bonding five layers of gold coated photoresist (SU-8) each $200\ \mu\text{m}$ thick. The construction is similar to a previously reported coaxial line filter [7], but at a higher frequency. Dielectric loss is negligible as it is air filled. A support system is needed to hold up the suspended line which forms both the ridge and the centre conductor of the coaxial cable. To solve this problem, the suspended ridge line is connected to the outer wall by shorted stubs which have a cut-off frequency higher than the operation frequency of the main waveguide. The ridges of the four stubs hold the suspended ridge of the main line waveguide. Ideally the stubs will be invisible to the signal at the designed frequency. The stubs are shown in Figure 4. Each of the layers, with dimensions, is shown in Figure 5.

The characteristic impedance of each coaxial line is $50\ \Omega$. Equation (1)–(3) have been used to calculate the size. Referring to Figure 1, h and b are fixed at $200\ \mu\text{m}$ layer thickness. The calculation gives $g=125\ \mu\text{m}$ and $w=190\ \mu\text{m}$. A short air filled $50\ \Omega$ co-planar line is added at each port for measurement purposes

Equation (4) has been adopted to estimate an appropriate size of a single ridge waveguide structure. B and d are fixed because they are made

of the 3 or 2, 200 μm layers respectively. Therefore, the only parameters that can be changed to meet the required frequency range are A and s . In practice, a waveguide useful lower frequency is at 25% higher than the cut-off frequency [14]. In this work the start frequency is 60 GHz. Therefore, the cut-off frequency of the main ridge waveguide is chosen to be at 48 GHz with $A=2$ mm, $B=0.6$ mm, $s=1.12$ mm and $d=0.2$ mm. The stubs that hold the suspended ridge of the main line waveguide are calculated to operate at a higher order mode. In this case, the cut-off frequency of the stub is 110 GHz which gives $A=0.75$ mm, $B=0.6$ mm, $s=0.3$ mm and $d=0.2$ mm. The size of the whole structure is 10.7mm x 5.0 mm x 1 mm. The design has been simulated using CST Microwave Studio software and some optimization has been applied in consideration of the junction effects where the main line and the stubs meet [13].

5. Results

The structure has been assembled and measured using an on-wafer probe station connected to a vector network analyzer. Before the measurement is carried out, a line-reflect-reflect-match (LRRM) full two-port calibration has been done. A similar measurement setup has been implemented in [7].

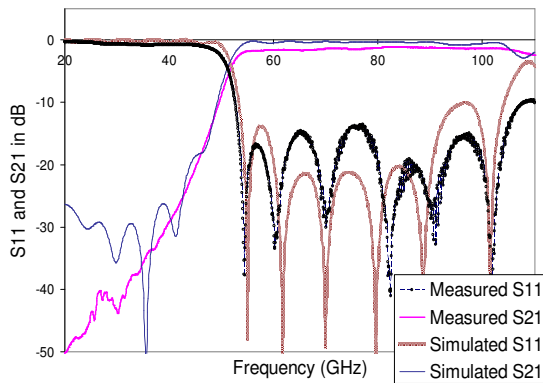


Figure 6. Measured and simulated results of back to back coaxial line to ridged waveguide transition.

A comparison of simulated and measured results is shown in Figure 6. The minimum measured insertion loss is 1 dB. The simulated return loss is below 19 dB from 60 GHz to 90 GHz. However, there is some deviation in measurement due to the process of assembling the structure. Some misalignment during the process affects the performance. Overall, the measurement result agrees well with the simulation.

The coaxial shorted stub supporting systems in [7] has been implemented using a wideband bandpass filter design, with a fixed quarter wavelength separations. The circuit here has been simulated again with different stub separation, S and stub length, L . The responses are similar but with very slight differences and are shown in Figure 7 and 8. By using higher order mode waveguide, it gives an advantage in flexibility of placing the supporting shorted stub in circuit.

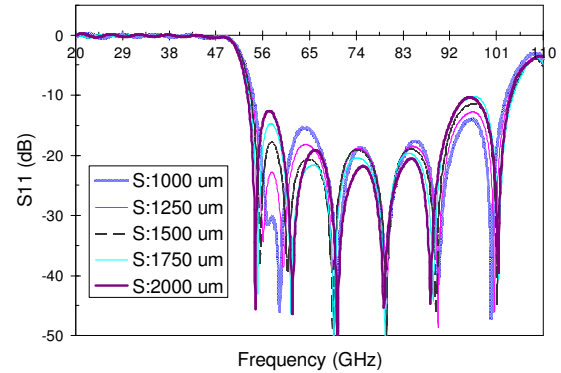


Figure 7. Return loss for different stub separation, S

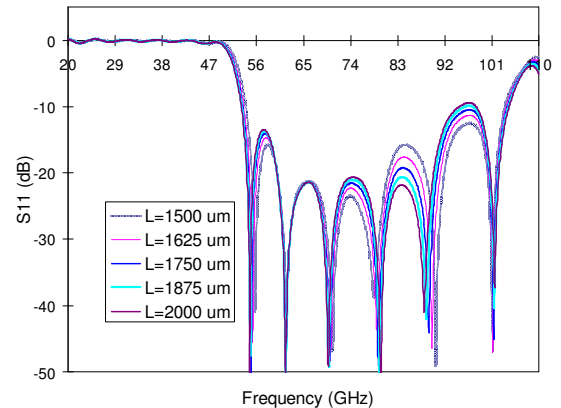


Figure 8. Return loss for different stub length, L

6. Conclusions

A coaxial line to single ridged waveguide operating between 60 to 90 GHz has been successfully simulated and measured. The structure is designed to fit the five layers gold-coated SU-8 micromachining. Generally, both simulation and measurement results give a good agreement.

Future work will be the implementation of a H-plane horn antenna fed by a rectangular coaxial line via this transition.

References

- [1] Stephan Biber, Jan Schiir, Arnd Hofmann, Lorenz-Peter Schmidt, "Design of New Passive THz Devices Based on Micromachining Techniques", *MSMw04 Symposium Proceedings. Kharkov, Ukraine*, June 21-26, 2004, pp. 26-31.
- [2] L. Bryzek, K. Peterson, and W. McCulley, "Micromachines on the March", *IEEE Spectrum*, 1994, pp. 20-31.
- [3] CTC Nguyen, LPB Katehi, and GM Rebeiz, "Micromachined Devices for Wireless Communications", *Proceedings of the IEEE*, vol.86, no.8, 1998, pp. 1756-1768.
- [4] M. R. Boyd, Parallel Plate Line Transition Section Between a Coaxial Line and Ridged Waveguide, " U.S. Patent 3188583, June. 8, 1965.
- [5] W.T. Patton, and R. J. Mason, "Coaxial Line to Waveguide Coupler ," *U.S. Patent 4409566*, Oct. 11, 1983.
- [6] Vincenzo Galdi, Giampiero Gerini, Marco Guglielmi, Huib J. Visser, and Francesco D'Agostino, "CAD of Coaxially End-Fed Waveguide Phased Array Antenna", *Microwave and Optical Technology Letters*, Vol. 34, No.4 , August, 2002, pp. 276-281.
- [7] M. J. Lancaster, J. Zhou, M.L.Ke, Y. Wang, K. Jiang, "Design and High Performance of a Micromachined K-Band Rectangular Coaxial Cable", *IEEE Trans. Microwave Theory Tech.*, vol. 55, no. 7, 2007, pp. 1548-1553.
- [8] T. S Chen, "Determination of the Capacitance, Inductance, and Characteristic Impedence of Rectangular Lines", *IRE Transaction on Microwave Theory and Techniques*, Vol. 8, no.5, September 1960, pp 510-519.
- [9] Cohn S.B. 'Properties of Ridge Waveguide'. *I.R.E Proceeding*, 1946, pp 783-788.
- [10] Helzajn J. "Ridge waveguides and passive microwave components", Institute of Electrical Engineers, London, 2000
- [11] W. Hoefer, M.N. Burton, "Closed Form Expression for the Parameters of Finned and Ridged Waveguide", *IEEE Transaction of Microwave Theory and Techniques*, vol. MTT-30, No. 12, December 1982, pp. 2190-2194.
- [12] I. Lamas, M. J. Lancaster and P.S. Hall, " A Low Loss Wideband Suspended Coaxial Line Components", *Microwave Optical Technology Letter*, Vol 43, no.1, Jan 2004, pp 93-95.
- [13] J. S. Hong and M.J. Lancaster, "*Microstrip Filters for RF/Microwave Applications*", John Wiley & Sons, 2001.
- [14] Hopfer S. "The design of ridged waveguides", *I.R.E Transactions On Microwave Theory And Techniques*, vol. MTT-3, October 1955, pp. 20-29.
- [15] G. Mathaei, L. Young, and E.M.T Jones, "*Microwave Filters, Impedance-Matching Networks, and Coupling Structures*", Artech House, November 1985.

Murad, N.A.; Lancaster, M.J.; Yi Wang; Ke, M.L.; , "Micromachined millimeter-wave Butler matrix with a patch antenna array," *Mediterranean Microwave Symposium (MMS), 2009*, pp.1-4.

doi: 10.1109/MMS.2009.5409809

Micromachined Millimeter-wave Butler Matrix with a Patch Antenna Array

N. A. Murad, M. J. Lancaster, Yi Wang, M. L. Ke.

Dept. of Electronic, Electrical and Computer Engineering,
The University of Birmingham, United Kingdom

nam623@bham.ac.uk, m.j.lancaster@bham.ac.uk, y.wang.6@bham.ac.uk,
m.l.ke@bham.ac.uk.

Abstract— This paper presents a micromachined patch antenna array with an integrated 2x2 Butler matrix (BM) beamformer. It was designed at 63 GHz and simulated using CST Microwave Studio 3D simulator. The BM is made using a low loss air filled rectangular coaxial line. The structure is constructed by bonding five layers of gold coated photoresist SU-8, each 200 microns thick. The experimental result shows a good matching achieved with return loss of -13 dB and inter-port isolation of about -22 dB at 63 GHz.

Keywords- micromachined, millimeter wave, beamforming, branch line coupler, patch array antenna.

I. INTRODUCTION

Microwave signals cover a wide range of frequencies from 300 MHz to 300 GHz. There has been enormous research in microwave systems and applications below 30 GHz and systems are now in rapid development for higher frequencies. For example the use of information, communication and sensing technologies in transportation systems are recognized to have the potential to help mobility in the future. Intelligent Transportation Systems (ITS) have been studied for many years in Europe, North America and Japan [1]. Short range radar (SRR) and long range radar (LRR) systems have been identified as key technologies to improve road safety. The 77 GHz band has been allocated for the automotive radar system in Europe. The 63 GHz band is then allocated for automotive data link transceiver.

This paper presents a micromachined patch antenna array beamforming network together with a 2x2 Butler matrix (BM) designed at 63 GHz. The structure is constructed in coaxial cable with five metallic layers that are bonded together to form the device. The challenge in this micromachined design is to have all the lines suspended so that no dielectric is required. The elimination of the dielectric allows

lower loss and the removal of any substrate modes which can be a problem at high frequencies. The use of coaxial lines provides a compact structure with no cross coupling between different parts of the circuit. Support lines are designed to hold the circuits together and not to sacrifice the performance of the system. At this very high frequency, a small deviation will bring a huge effect on the device performances. Modifications have been made to the ports to fit the signal-ground-signal measurement probe, as well as the antenna feeding line. A similar air-spaced design has been discussed in [2], but non micromachined and at 6.3 GHz.

II. DESIGN

The structures design is divided into two parts. One is the BM comprising a hybrid branch-line coupler. Second is the patch array antenna. The two parts then are combined together.

A. Hybrid Branch Line Coupler

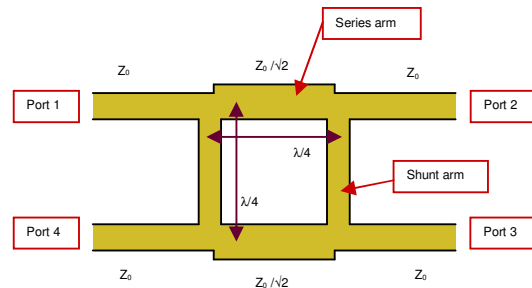


Fig 1 Branch Line Coupler Geometry

The branch-line coupler has symmetrical four ports as shown in Fig. 1. For a branch-line coupler any port can be an input port. Output ports are on the opposite side of the input port, while the port of the same side as the input port is isolated. For instance, if the input

is from Port 1, then Port 2 and Port 3 become the output and Port 4 is isolated. The outputs are usually of equal amplitude but quadrature phase [3]. The coupling factor can be determined by the ratio of the shunt and series arms impedance and is optimized to maintain a proper match over the required bandwidth [4].

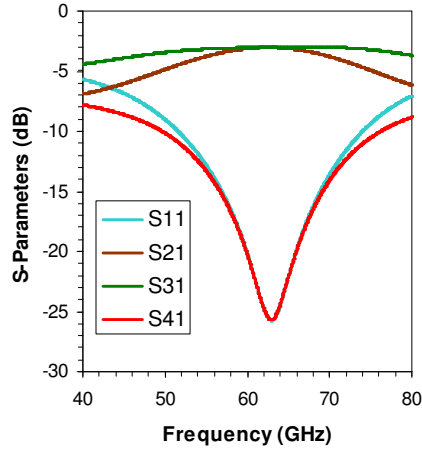


Fig. 2 Simulated response of the designed branch line coupler

Fig. 2 shows the S parameters response of the designed branch line coupler. The structure is made by using air filled rectangular coaxial line. The cross-section of an ideal rectangular coaxial line is shown in Fig. 3, depicting the five layers used in the construction.

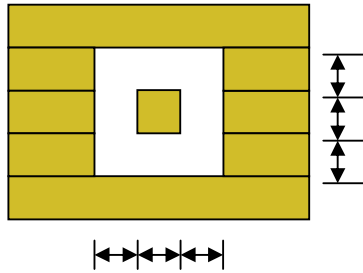


Fig. 3 Cross-section of an ideal air-filled rectangular coaxial line

The characteristic impedance can be approximately calculated by [5,6,7]

$$Z = \frac{376.62}{2\left(\frac{b}{g} + \frac{w}{h}\right) + 4\left(\frac{C1 + C2}{\epsilon}\right)} \quad (1)$$

where b , g , w and h for our circuit are given in Fig. 4. In this case ϵ is the free space permittivity, and $C1$ and $C2$ are the fringing capacitance produced by flux disturbance along vertical and horizontal side, respectively. They can be calculated by [5,6,7]

$$C1 = \frac{\epsilon}{\pi} \left[\ln \frac{g^2 + h^2}{4h^2} + 2\left(\frac{h}{g}\right) \arctan \frac{g}{h} \right] \quad (2)$$

$$C2 = \frac{\epsilon}{\pi} \left[\ln \frac{g^2 + h^2}{4g^2} + 2\left(\frac{g}{h}\right) \arctan \frac{h}{g} \right] \quad (3)$$

The inner conductor is supported by means of quarter wavelength stubs. The stubs are shorted to the outer wall at one end, and connected to the coaxial line centre conductor at the other end, this is shown in Fig. 4. The similar stubs supporting system has been used in [7,8,9].

B. Patch Array Antenna

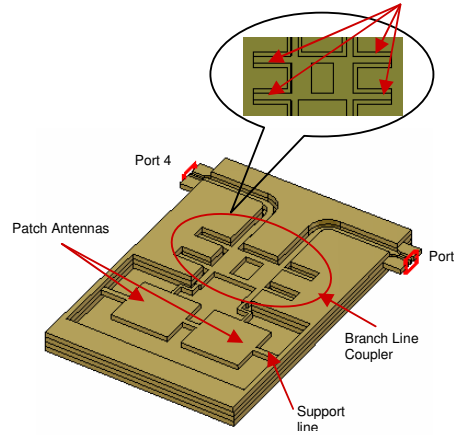


Fig 4 Structure layout of the 2x2 BM with patch array antenna

The array antenna consists of two rectangular patch antennas. The air filled micromachined antenna can be supported using thin membrane [10] or supporting posts [11]. In this work, the support lines that connect the antenna and the outer wall are placed at the point of minimum voltage to avoid significant effect on the antenna itself. The antenna is directly connected to the output port of the coupler by quarter wavelength transformer. The resonant input impedance of the antenna is calculated to be 500Ω . Therefore the

impedance of the quarter wavelength transformer is chosen to be at 158Ω to match the 50Ω output line from the coupler. Fig 4 shows the whole structure without the top layer that covers the ports and the BM. The overall structure size is $7.4 \text{ mm} \times 11.0 \text{ mm} \times 1.0 \text{ mm}$.

III. FABRICATION

The fabrication process begins with SU8 patterning, which was described earlier in [12]. Following the patterning and subsequent hard-baking, the SU8 pieces were released from a silicon substrate by etching the substrate away. The metal coating was done using a Cressington 308 coater, which combines plasma cleaning, chromium layer sputtering and gold or silver thermal evaporation. The SU8 pieces were mounted onto a substrate holder which was tilt into a set angle and spin continuously. 30 second plasma cleaning was firstly carried out, followed by a 5 nm chromium layer sputtering for improved adhesion and then a $2 \mu\text{m}$ thick gold layer was thermally evaporated onto the pieces. These pieces were then bonded together layer by layer to form the final device. Fig. 5 shows the exploded view of the five layers assembled structure. It consists of the inner conductors and the patch antenna at the middle (III) layer, sandwiched by two outer conductors layers (II and IV) and enclosed by top (I) and bottom (V) layers. All unconnected pieces at each layer are joined by tethers that are broken off after bonding.

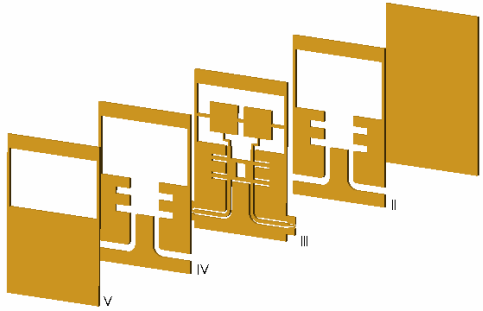


Fig 5 Exploded view of the five layers structure

IV. RESULTS

The design has been modeled using CST Microwave Studio [13]. The fabricated device has been measured using an on-wafer probe station connected to a vector network analyzer. A line-reflect-reflect-match (LRRM) full two-port

calibration has been performed. A similar measurement setup has been implemented in [7, 8].

Fig. 7 shows the inter-port isolation, while Fig. 6 shows the return loss with the input from port 1 and port 4 respectively. Some misalignment during fabrication may have resulted in a slightly higher return loss in the measurement response as compared with simulations. However, the structure is still well matched at the desired 63 GHz.

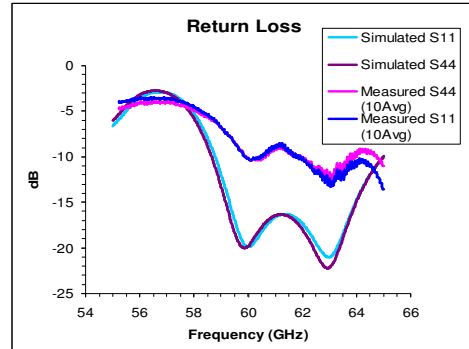


Fig. 6 Simulated and measured return loss with input from port 1 and port 4 respectively.

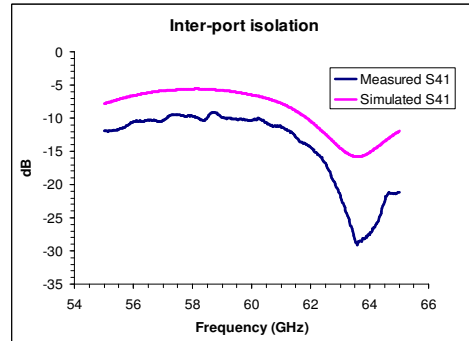


Fig 7 Simulated and measured inter-port isolation

The simulated farfield radiation patterns are depicted in Fig. 8 and Fig. 9 with the input from port 1 and port 4 respectively. The broadside beam is at 106° with side lobe level of -8.7 dB when the input is on port 1. Input from port 4 led to the broadside beam at 73° . The beams are formed at about $\pm 16^\circ$ from the perpendicular when each of the two ports is fed individually.

The co-polar radiation pattern has been measured at every 2° with standard horn antenna as the transmitter. Due to some obstruction in the current measurement setup, it is not possible to measure below 40° and above 140° . The results are shown in Fig. 10. A moving average, averaging every 3 adjacent data point, has been applied to the data. The results are comparable to the simulated results.

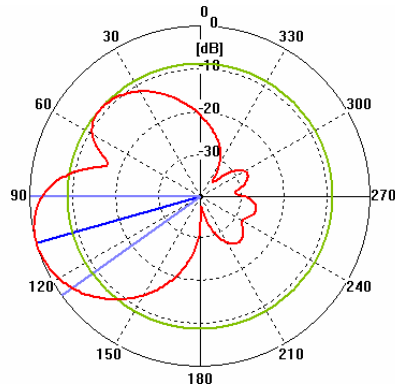


Fig.8 Simulated radiation polar pattern with an input at port 1 at 63 GHz

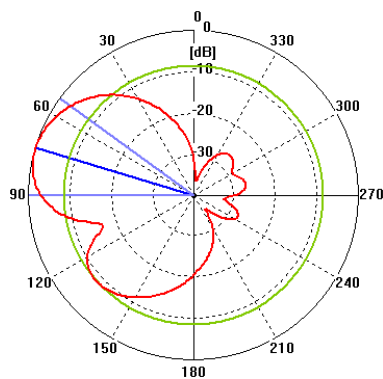


Fig.9 Simulated radiation polar pattern with an input at port 4 at 63 GHz

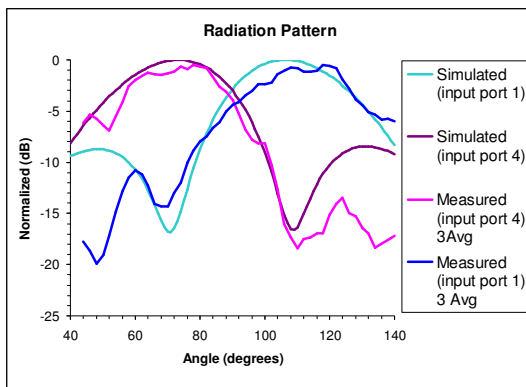


Fig. 10 Simulated and measured radiation plot.

V. CONCLUSION

A micromachined millimeter wave patch array antenna with a Butler matrix beamforming network has been designed and tested. The structure is matched at the desired 63 GHz with low return loss. The beam is formed at $\pm 16^\circ$ in the boresight, as expected from array factor calculation based on the BM quadrature phase properties.

ACKNOWLEDGMENT

N. A. Murad thanks the Government of Malaysia and University of Technology Malaysia for sponsoring her PhD on this work.

REFERENCES

- [1] Karl. M. Strohm, Hans Ludwig Bloecher, Robert Schneider, Josel Weinger, "Development of Future Short Range Radar Technology," EUMW Technical Digest, October 2005, pp. 165 – 168.
- [2] T.Y Lee, P Gardner, 'Air-spaced Beamforming Patch Antenna Array', Electronic Letters, Vol.40, Issue 12,10 June 2004 , pp.714 – 715
- [3] Pozar, D.M. 'Microwave Engineering. Third Edition' John Wiley & Sons, 2005.
- [4] Kai Chang, 'Handbook of Microwave and Optical Components, vol.1'. John Wiley & Sons, 1989.
- [5] T. S Chen, "Determination of the Capacitance, Inductance, and Characteristic Impedence of Rectangular Lines", IRE Transaction on Microwave Theory and Techniques, Vol. 8, no.5, September 1960, pp 510-519.
- [6] J. R. Reid, E. D. Marsh, and R. T. Webster, "Micromachined Rectangular Coaxial Transmission Lines" , IEEE Trans. Microw. Theory Tech., vol. 54, no. 8, Aug. 2006, pp. 3433–3442
- [7] M. J. Lancaster, J. Zhou, M.L.Ke, Y. Wang, K. Jiang, "Design and High Performance of a Micromachined K-Band Rectangular Coaxial Cable", IEEE Trans. Microwave Theory Tech., vol. 55, no. 7, 2007, pp. 1548-1553
- [8] Y. Wang, M. Ke, M. J. Lancaster, F. Huang, "Micromachined Millimeter-wave Rectangular-Coaxial Branch-Line Couplers with Enhanced Bandwidth", IEEE Trans. Microwave Theory Tech. vol. 57, no. 7, 2009, pp. 1655-1660.
- [9] K Jiang, M.J.L., I Llamas-Garro, P Jin, "SU-8 Ka Band Filter and Its Microfabrication". Journals of Micromechanics and Microengineering, 2005: p. 1522-1526
- [10] Preeti Sharma and Shibani K. Koul, "Design and Development of Millimeter-Wave Micromachined Patch Antennas", IETE Journal of Research, Vol.55, Issue.1, 2009, pp. 40-50
- [11] Jeong-Geun Kim, Hyung Suk Lee, Ho-Seon Lee, Jun-Bo Yoon, and Songcheol Hong, "60-GHz CPW-Fed Post-Supported Patch Antenna Using Micromachining Technology", IEEE Microwave and Wireless Components Letters, Vol. 15, No.10, October 2005, pp. 635-637.
- [12] Ke, Y. Wang, and M. Lancaster "Design and Realisation of Low-loss Air-filled Rectangular Coaxial Cable with Bent Quarter-wavelength Supporting Stubs", Micro. And Opt. Tech. Let., vol. 50, no. 5, pp.1443-1446 (2008)
- [13] CST Microwave Studio. CST GmbH, Darmstadt, Germany, 2006

Murad, N.A.; Lancaster, M.J.; Gardner, P.; Ke, M.L.; Wang, Y.; , "Micromachined H-plane horn antenna manufactured using thick SU-8 photoresist," *Electronics Letters* , vol.46, no.11, May 2010, pp.743-745.

doi: 10.1049/el.2010.1054

Micromachined H-plane horn antenna manufactured using thick SU-8 photoresist

N.A. Murad, M.J. Lancaster, P. Gardner, M.L. Ke and Y. Wang

A micromachined H-plane horn antenna designed at 63 GHz is presented. The horn is integrated with an air filled coaxial line to ridge waveguide transition with the ridge waveguide feeding the horn. The antenna is constructed by bonding five layers of gold coated SU-8 photoresist, each 200 μm -thick. The performance has been validated experimentally using on-wafer probe measurements. A good match is achieved with low return loss obtained at the designed operating frequency. This proposed design is to be used in three-dimensional phased array beamformers.

Introduction: Horn antennas are widely used, especially as feed elements for communication dishes and astronomy satellites. Some previous work on micromachined horn antenna has been reported. Two horn antennas have been integrated in [1] to couple power into and out of a micromachined waveguide. A sacrificial photoresist layer was used to create the hollow in the waveguide and horns' aperture. An octagonal micromachined horn antenna at 585 GHz was discussed in [2]. A crystallographic etching and ultraviolet lithography of thick SU-8 photoresist technique was proposed. The crystal planes of the silicon substrate and the thickness of the photoresist controlled the shape of the horn. An integrated H-plane horn antenna was presented in [3]. Pillars with uniform spaces were fabricated on top of a metalised substrate as a lower horn side wall to allow a coplanar waveguide (CPW) feeding line to excite the signal into the antenna. Another two layers of silicon are stacked on top for the upper side wall and covered with a top plate. However, some discrepancies between simulated and measured results were observed, which may be caused by inaccurate dimensions and the failure of pillars. These were scrutinised in their post-fabrication simulations.

The H-plane horn proposed here is linearly flared in one plane. It is built using five layers of metal coated SU-8 thick photoresist discussed in the 'Fabrication' Section below. The thick SU-8 photoresist technique proposed here has the advantage of being dielectric-free with all layers processed simultaneously. No sacrificial layer is involved, thus minimising the cost. Furthermore, the horn edge is not governed by the etching process as it was in [2]. A rectangular coaxial line to ridge waveguide transition is used to excite the signal into the horn. Therefore, the side wall is made sturdy with metal coated SU-8 photoresist avoiding the pillars issue discussed above. Moreover, the horn designed has a very short length. This reduces overall area and the usage of the material.

Design: The proposed five-layer structure is presented in Fig. 1. The horn is fed by a single ridge waveguide having a transition from a rectangular coaxial line attached to a coplanar waveguide. The coplanar waveguide port is used in this case solely for on-wafer probe measurement purposes. This low-loss air filled rectangular coaxial line is an excellent candidate for high performance integrated transmission line circuitry [4]. Referring to the cross-section (A) in Fig. 1, a 50 Ω coaxial line is designed using Chen's equations in [5] giving $g = 125 \mu\text{m}$, $G = 190 \mu\text{m}$ and $t = 200 \mu\text{m}$. The horn is designed with the aperture dimensions of $al = 4180 \mu\text{m}$ by $bl = 600 \mu\text{m}$. The horn is flared in the H-plane to the aperture from the throat. The throat, which is the ridge waveguide, is designed to have a cutoff frequency of 48 GHz using the closed loop equation in [6]. The width of the waveguide is 2000 μm and the height is 600 μm . The ridge is symmetrically placed at the centre of the waveguide width. The dimensions, referring to cross-section (C) in Fig. 1 are $s = 1060 \mu\text{m}$ and $t = 200 \mu\text{m}$. Notice that the structure is air filled. Therefore, all the suspended lines on each layer must be supported by a structure on the same layer. Higher-order mode ridge waveguide stub support lines are introduced in [7]. The stubs are in their cutoff region at the main waveguide operating frequency. The stub ridge waveguide is designed at 110 GHz cutoff frequency giving $a = 750 \mu\text{m}$, $b = 600 \mu\text{m}$ and $s = 300 \mu\text{m}$. The ridges of the stubs hold the ridge of the main waveguide and are attached to the outer wall.

Fabrication: The five-layer structure is chosen in order to build an air filled coaxial line. The SU-8 is spread and spin coated at 300 and

1000 rpm spin, respectively, before undergoing a stepped soft bake. The soft bake is stepped from 65° C for 10 min to 95° C for 75 min. The wafer is then exposed under UV light using a Canon 501 mask aligner. Post-exposure bake is stepped again from 65° C for 2 min to 95° C for 25 min. The wafer is then developed using EC solvent and finally the processed SU-8 pieces are released from the Si substrate and coated with Cr and Au. The coated pieces are aligned and bonded together to form the 3D structure.

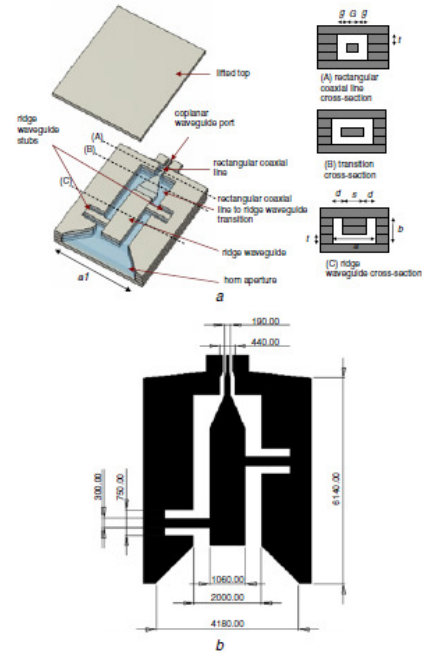


Fig. 1 Proposed antenna

a Five-layer structure and cross-sections
b Top view of third layer (dimensions in micrometres)

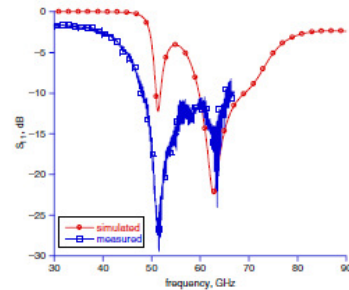


Fig. 2 Simulated and measured frequency response (S_{11})

Results: The manufactured structure has been measured using an on-wafer probe measurement setup up to 67 GHz. The measured and simulated return loss for the designed integrated H-plane antenna is shown in Fig. 2. The antenna is matched at the 63 GHz designed frequency. There is disagreement between simulated and measured S_{11} responses at lower frequency. The losses and imperfections within the structure owing to the fabrication process contribute to the difference between simulation and measurements. The radiation pattern is also measured at 63 GHz. The area surrounding the probe station is shielded by the absorbing material to minimise the error due to reflections during measurement. The measured pattern follows the simulated plot, as shown in Fig. 3. The measured main beam is broader than the one obtained from the simulation, which has a 48° half power beamwidth, although there is

more ripple in the gain within the main beam. From the simulation, the antenna is observed to have a single main lobe with no significant changes in side lobe level from 58 to 66 GHz. The realised gain is between 8 to 9 dB within the frequency range.

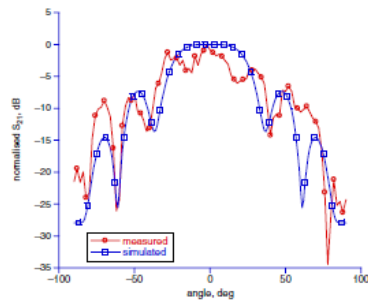


Fig. 3 Simulated and measured radiation pattern

Conclusions: A micromachined H-plane horn antenna is presented. It has been integrated with a rectangular coaxial line to ridge waveguide transition and demonstrated to operate at 63 GHz. The proposed structure can be used to integrate with other rectangular coaxial circuits at millimetre waves. The advantages over previously published structures include the use of an inexpensive SU8 process, the absence of dielectric and posts, smaller overall size and the fact that the quality of the horn wall is not reliant on the etching process.

© The Institution of Engineering and Technology 2010

20 April 2010

doi: 10.1049/el.2010.1054

One or more of the Figures in this Letter are available in colour online.

N.A. Murad, M.J. Lancaster, P. Gardner, M.L. Ke and Y. Wang
(*Electronic Electrical and Computer Engineering, University of Birmingham, B15 2TT, United Kingdom*)

E-mail: nam623@bham.ac.uk

N.A. Murad (*Fakulti Kejuruteraan Elektrik, Universiti Teknologi Malaysia (UTM), Johor Bahru, Johor 81310, Malaysia*)

References

- 1 Digby, J.W., Collins, C.E., Towson, B., Karatzas, L.S., Parkhurst, G., Chamberlain, J.M., Bowen, J.W., Pollard, R.D., Miles, R.E., Steenson, D.P., Brown, D.A., and Cronin, N.J.: 'Integrated micromachined antenna for 200 GHz operation', *IEEE MTT-S Int. Microw. Symp. Digest*, 1997, pp. 561–564
- 2 Hesler, J.L., Hui, K., Dahlstrom, R.K., Weikle, R.M., Crowe, T.W., Mann, C.M., and Wallace, H.B.: 'Analysis of an octagonal micromachined horn antenna for submillimeter-wave applications', *IEEE Trans. Antennas Propag.*, 2001, **49**, pp. 997–1001
- 3 Pan, B., Li, Y., Ponchak, G.E., Tentzeris, M.M., and Papapolymerou, J.: 'A low-loss substrate-independent approach for 60 GHz transceiver front-end integration using micromachining technologies', *IEEE Trans. Microw. Theory Tech.*, 2008, **56**, pp. 2779–2788
- 4 Wang, Y., Ke, M.L., Lancaster, M.J., and Huang, F.: 'Micromachined millimeter-wave rectangular-coaxial branch-line coupler with enhanced bandwidth', *Microw. Theory Tech.*, 2009, **57**, pp. 1655–1660
- 5 Reid, J.R., Marsh, E.D., and Webster, R.T.: 'Micromachined rectangular-coaxial transmission lines', *IEEE Trans. Microw. Theory Tech.*, 2006, **54**, pp. 3433–3444
- 6 Helszajn, J.: 'Ridge waveguides and passive microwave components' (IET, 2000)
- 7 Murad, N.A., Lancaster, M.J., Wang, Y., and Ke, M.: 'Micromachined rectangular coaxial line to ridge waveguide transition'. 10th Annual Wireless and Microwave Technology Conf., Florida, USA, 2009, pp. 1–5